NASA Technical Memorandum 81847

NASA-TM-81847 19800020136

THE DEVELOPMENT OF A STEPPED FREQUENCY MICROWAVE RADIOMETER AND ITS APPLICATION TO REMOTE SENSING OF THE EARTH

RICHARD F. HARRINGTON

JUNE 1980

NASA
National Aeronautics and
Space Administration

Langley Research Center
Hampton, Virginia 23665

Page missing in original document.

Page missing in original document.

TABLE OF CONTENTS

Page

LIST OF TABLES vii

LIST OF FIGURES viii

LIST OF SYMBOLS xii

Chapter

I. INTRODUCTION 1

Objective of This Research 1

Background of Microwave Radiometers 2

Background of Microwave Radiometer Remote Sensing Measurements 4

Overview 7

II. THEORETICAL ANALYSIS 9

Radiative Transfer Equation 9

Atmospheric Absorption and Emission 15

Thermal Emission From Natural Surfaces 23

Radiating Properties of Water and Ice 34

III. INSTRUMENT DESIGN AND ANALYSIS 47

Design Technique 47

Design Description 52

Analysis 83

N80-28637 #

Chapter Page

IV. RADIOMETER ALGORITHMS 104
  Radiative Transfer Equation Algorithm 104
  Antenna Pattern Correction 114
  Windspeed Correction 116
  Cloud Correction 119
  Sea Surface Temperature Inversion Algorithm 122
V. AIRCRAFT REMOTE SENSING RESULTS 124
  Radiometric Mapping of an Ocean Polar Front 124
  Ice Thickness Measurements 129
  Sea Ice Measurements 139
VI. CONCLUSIONS 153
LIST OF REFERENCES 156

APPENDIXES

A. ERROR DUE TO RAYLEIGH-JEANS APPROXIMATION 162
B. RADIATIVE TRANSFER EQUATION PROGRAM 164

LIST OF TABLES

TABLE PAGE

2-1. Change in Brightness Temperature (K) Due to Atmospheric Oxygen at an Altitude of 20 km 20

2-2. Change in Brightness Temperature (K) Due to Atmospheric Water Vapor at an Altitude of 20 km, Water Vapor Density of 10 g/m^3, and Scale Height of 5 km 21

3-1. Data Recorded on Digital Tape Recorder 79

3-2. Commutated Temperatures 79

3-3. Typical Values for SFMR Measurement 94

3-4. Typical Values During Calibration and Measurement 101

4-1. Error Budget for 0.1 K Accuracy 110

4-2. Variation in Dependent Variables 113

4-3. Antenna Correction Factor 116

4-4. Cloud Attenuation 122

LIST OF FIGURES

FIGURE PAGE

2-1. Electromagnetic radiation contributions to the radiative transfer equation 11

2-2. Change in brightness temperature from oxygen in the atmosphere as a function of altitude and surface temperature . . 22

2-3. Change in brightness temperature from atmospheric water vapor versus altitude, water vapor density, and scale height for a surface temperature of 10° C and frequency of 6 GHz 24

2-4. Boundary value problem for a dielectric layer over a semi-infinite dielectric medium 27

2-5. Emissivity of sea water at 5° C versus incidence angle at frequencies of 4, 6, and 8 GHz for vertical, horizontal, and circular polarization 31

2-6. Emissivity of an ice layer over water versus thickness at frequencies of 4, 6, and 8 GHz with ice attenuation coefficients of 0 dB/m and 50 dB/m 33

2-7. Emissivity of fresh water and sea water versus surface temperature at frequencies of 4, 6, and 8 GHz 36

2-8. Comparison of theoretical and measured radiometric brightness temperatures for smooth and rough surfaces versus incidence angle 38

2-9. Emissivity of a foam covered sea surface versus fractional foam coverage for a foam with 5 percent water, 3 cm thick, and a frequency of 6 GHz 39

2-10. Emissivity of rough lake ice over fresh water versus attenuation at a water temperature of 0° C, an ice dielectric constant of 3.2-j0.0066, and for frequencies of 4, 6, and 8 GHz 43

2-11. Skin depth of a dielectric medium versus the loss tangent at frequencies of 4, 6, and 8 GHz 45

3-1. Block diagram of the stepped frequency microwave radiometer 53

3-2. Stepped frequency microwave radiometer configured for installation in NASA CV-990 aircraft 55

FIGURE PAGE

3-3. Diagram of the antenna subsystem 56

3-4. Corrugated horn antenna without radome and polarizer 58

3-5. Principal plane antenna patterns of the stepped frequency microwave radiometer antenna including radome and polarizer at a frequency of 6 GHz 60

3-6. Absorption and reflection coefficients of the radome versus frequency 62

3-7. Block diagram of the microwave front end of the radiometer contained in the constant temperature enclosure 64

3-8. View of the microwave front end showing the antenna feed and noise injection circuit components 66

3-9. View of the microwave radiometer front end showing the temperature stabilizing plate, thermal control paths, tunnel diode amplifier, and Dicke circulator switch 67

3-10. Block diagram of the receiver portion of the stepped frequency microwave radiometer 69

3-11. View of the receiver showing the local oscillator, mixer-preamplifier, and predetection filters 70

3-12. Block diagram of the analog signal processor 73

3-13. Block diagram of the driver circuits 76

3-14. View of the analog signal processor and driver circuits . . 78

3-15. Block diagram of the digital subsystem 80

3-16. Front panel view of the digital controller for the stepped frequency microwave radiometer (microwave spectrometer) 82

3-17. Sensitivity of a balanced Dicke radiometer versus integration time for predetection bandwidths from 20 MHz to 2 GHz, receiver noise temperature of 600 K, and a Dicke reference temperature of 308 K 86

FIGURE PAGE

3-18. Ratio of the change in surface temperature to the resulting change in radiometer measured temperature versus loss prior to comparison junction at a surface temperature of 10° C, emissivity of 0.3624, altitude of 500 m, and frequency of 6 GHz 88

3-19. Calibration of the stepped frequency microwave radiometer 97

4-1. Windspeed correction factor 118

4-2. Cloud models of liquid water content versus height of cloud above cloud base (Love, et al., 1975) 120

5-1. Location of the polar front region near Bear Island in the Barents Sea 125

5-2. Synoptic sea surface temperature on October 5, 1979 in the Bear Island region as observed by Airborne Expendable Bathythermograph (AXBT). (Dots indicate drop sites.) 127

5-3. Aircraft remote sensing observations on October 8, 1979 of the sea surface variations of microwave brightness temperature, sea surface thermodynamic temperature measured by the aircraft infrared radiometer, and "in-situ" thermodynamic temperature measured by a surface vessel on October 5, 1979 along the north south transect across the Barents Sea ocean front 128

5-4. Sea surface radiometric brightness temperature on October 8, 1979 along four north south transects across the Barents Sea ocean front 130

5-5. Location of the lake ice measurements conducted in Mackinac Straits, Lake Michigan, showing flight lines and location of ground truth measurements 132

5-6. Radiometric brightness temperature of lake ice versus longitude for line 2 134

5-7. Radiometric brightness temperature of lake ice at White Shoal Light on line 2 135

5-8. Radiometric brightness temperature of lake ice versus longitude for line 4 136

FIGURE PAGE

5-9. Radiometric brightness temperature of lake ice versus latitude during north south transect of lines 1 through 8 138

5-10. Location of the sea ice measurements of first year, multiyear, and frequency sensitive ice in the Arctic Ocean 141

5-11. Aerial photograph of an isolated piece of multiyear ice embedded in first year ice along line 1 in Fig. 5-10 142

5-12. Aerial photograph of multiyear ice along line 1 in Fig. 5-10 143

5-13. Radiometric brightness temperature of sea ice versus time for run 8 at a frequency of 7.2 GHz and an integration time of 0.5 s 144

5-14. Radiometric brightness temperature of sea ice versus time for run 6 at frequencies alternating between 5.6 GHz and 6.6 GHz every 0.5 s 146

5-15. Aerial photograph of a section of smooth, frequency sensitive sea ice along line 1 in Fig. 5-10 148

5-16. Radiometric brightness temperature of the frequency sensitive sea ice versus time for runs 4, 5, and 9 at a frequency of 5.6 GHz 149

5-17. Radiometric brightness temperature of the frequency sensitive sea ice versus time for run 8 at a frequency of 7.2 GHz 150

5-18. Radiometric brightness temperature of the frequency sensitive sea ice versus time for run 7 at frequencies alternating between 5.6 GHz and 6.6 GHz every second 151

B-1. Flow chart of TANT 165

B-2. Flow chart of ATMOD 166

LIST OF SYMBOLS

A	area, m^2
a_{CL}	total absorption due to clouds, dimensionless
B	brightness (used in Appendix A), $Wm^{-2}H_3^{-1}sr^{-1}$
B	bandwidth, Hz
B_{no}	noise bandwidth, Hz
B_{si}	statistical bandwidth, Hz
B_3	half power (3 dB) bandwidth, Hz
C_D	square law detector constant, V/W
C_1	antenna pattern correction, K
C_2	wind correction, K
C_3	cloud correction, K
c	velocity of light, 2.9979×10^8, m/s
d	thickness of layer, m
d_N	duty cycle of injected noise pulses, dimensionless
d_{N_C}	duty cycle of injected noise pulses during calibration, dimensionless
d_{N_M}	duty cycle of injected noise pulses during measurement, dimensionless
d_o	mean thickness, m
E	electric field strength, V/m
e	emissivity, dimensionless
$\langle e \rangle$	average emissivity, dimensionless
f	frequency, Hz
f_o	resonant frequency, Hz

Δf_o	linewidth, Hz
G	gain, dimensionless
G_0	maximum gain of antenna, dimensionless
G_R	radiometer gain, dimensionless
H_i	transfer function of the predetection filters, dimensionless
h	Planck's constant, 6.626×10^{-34}, J·s
h_r	altitude of radiometer, m
Im	imaginary component of a complex quantity
j	imaginary
K_1	forward gain constant, dimensionless
k	Boltzmann's constant, 1.38×10^{-23}, J/K
k_R	radiometer calibration factor, K
k_{R_C}	radiometer calibration factor during calibration, K
k_{R_M}	radiometer calibration factor during measurement, K
L	liquid water content of the clouds, g/m^3
N_{CL}	number of ungated clock pulses
N_G	number of gated clock pulses
$\hat{n}$	unit normal vector
P	barometric pressure [used in (2-14), (2-16), and (2-17)], Pa
P	power, W
P_a	absorbed power, W
P_c	barometric pressure during calibration, Pa
P_i	incident power, W
P_r	reflected power, W

R	voltage reflection coefficient, dimensionless
R^*	complex conjugate of R
$\|R\|^2$	power reflection coefficient, dimensionless
Re	real part of a complex quantity
r	distance, m
r_i	power reflection coefficient of air-ice boundary, dimensionless
r_R	power reflection coefficient of radiometer loss element, dimensionless
r_w	power reflection coefficient of ice-water boundary, dimensionless
s	distance, m
s_h	scale height for water vapor, m
T	thermodynamic temperature, K
ΔT	radiometer sensitivity, K
T_A	antenna temperature, K
T_{ant}	antenna thermodynamic temperature, K
T_B	brightness temperature, K
T_{B_i}	incident brightness temperature, K
T_{B_S}	surface brightness temperature, K
T_{CAL}	radiometric brightness temperature of calibration load, K
T_{CL}	thermodynamic temperature of cloud, K
T_{dw}	downwelling brightness temperature, K
T_I	injected noise temperature, K
T_M	measured noise temperature, K
T_0	Dicke reference load thermodynamic temperature, K
T_{pol}	polarizer thermodynamic temperature, K

T_R	radiometer noise temperature, K
T_{rad}	radome thermodynamic temperature, K
T_S	surface thermodynamic temperature, K
T_{uw}	upwelling brightness temperature, K
T_{wg}	waveguide to coaxial adapter thermodynamic temperature, K
T_α	thermodynamic temperature of loss α, K
$\hat{T}_{\alpha_C}$	composite thermodynamic temperature of the radiometer loss elements during calibration, K
$\hat{T}_{\alpha_M}$	composite thermodynamic temperature of the radiometer loss elements during measurement, K
$\hat{T}_{\alpha_R}$	composite thermodynamic temperature of the radiometer loss elements, K
T_∞	extraterrestrial electromagnetic radiation temperature, K
$\langle T \rangle$	mean thermodynamic temperature, K
$\langle T \rangle_a$	mean thermodynamic temperature of the atmosphere, K
$\langle T \rangle_h$	mean thermodynamic temperature of the atmosphere at altitude h, K
t_s	sample period, s
V_0	output voltage, V
z	altitude, m
α	real part of the complex propagation constant γ, m^{-1}
α_a	absorption coefficient, nepers/m
α_{CL}	absorption coefficient for nonprecipitating clouds, nepers/m
α_e	extinction coefficient, nepers/m
α_{O_2}	oxygen absorption coefficient, nepers/m
α_R	absorption coefficient of radiometer loss element, dB
α_s	scattering coefficient, nepers/m

α_{WV}	water vapor absorption coefficient, nepers/m
β	imaginary part of the complex propagation constant γ, m^{-1}
γ	propagation constant of the layered dielectric medium, m^{-1}
ε	dielectric constant, dimensionless
ε'	real component of the complex dielectric constant, dimensionless
ε''	imaginary component of the complex dielectric constant, dimensionless
ε_{C_1}	error in antenna temperature due to error in antenna pattern correction, K
ε_{C_2}	error in antenna temperature due to error in wind correction, K
ε_{C_3}	error in antenna temperature due to error in cloud correction, K
ε_e	error in antenna temperature due to error in emissivity, K
ε_M	complex dielectric constant of layered medium, dimensionless
ε_o	permittivity of vacuum, 8.854×10^{-12}, F/m
ε_s	static dielectric constant, dimensionless
$\varepsilon_{\sec\theta}$	error in antenna temperature due to error in incidence angle, K
ε_{T_A}	total error in antenna temperature, K
$\varepsilon_{T_{dw}}$	error in antenna temperature due to error in downwelling temperature, K
ε_{T_S}	error in antenna temperature due to error in surface thermodynamic temperature, K
$\varepsilon_{T_{uw}}$	error in antenna temperature due to error in upwelling temperature, K
ε_{τ_h}	error in antenna temperature due to error in opacity, K
ε_∞	dielectric constant at infinite frequency, dimensionless

θ	angle, rad
θ_a	antenna pointing angle, rad
λ	wavelength, m
μ_o	permeability of vacuum, $4\pi \times 10^{-7}$, H/m
ρ	density of water, g/m^3
ρ_W	water vapor density, g/m^3
σ	conductivity, S/m
τ	relaxation time, s
τ_h	opacity at altitude h, dimensionless
$\tau(z)$	opacity at altitude z, dimensionless
τ_∞	total one-way opacity, dimensionless
$\tau(\infty)$	total one-way opacity, dimensionless
$\langle \tau \rangle_a$	mean opacity of total atmosphere, dimensionless
$\langle \tau \rangle_h$	mean opacity of atmosphere at altitude h, dimensionless
Ω	solid angle, sr
ω	radian frequency, Hz

CHAPTER I

INTRODUCTION

Objective of This Research

The objective of this research was the design, development, and scientific utilization of a variable frequency microwave radiometer whose versatility, accuracy, and stability provide a capability to achieve significant contributions for the geophysical understanding of ocean and ice processes. This research included the development of (1) a computational technique to predict the radiometric brightness temperature at the input to the radiometer antenna as a function of the geophysical parameters, (2) a simplified algorithm for the computation of the expected radiometric brightness temperature, (3) a computer model of the radiometer to determine the input radiometric brightness temperature as a function of the radiometer output, and (4) a computer program to determine the emissivity of a layered dielectric media such as ice over water. Analyses of the radiometer accuracy and sensitivity are presented to demonstrate that the design meets the accuracy objectives of this research.

The microwave radiometer developed during this research, the stepped frequency microwave radiometer (SFMR), was flown on a National Aeronautics and Space Administration (NASA) C-130 aircraft. The SFMR was flight tested to demonstrate the capability of the instrument to measure radiometric brightness temperature from ocean and ice processes in actual field experiments. The SFMR participated in the 1978 and 1979

Great Lakes Ice Experiment, the 1978 and 1979 Sea Ice Radar Experiment (SIRE), and the 1979 Norwegian Remote Sensing Experiment (NORSEX). Four significant observations were accomplished during these experiments. These observations consisted of the first microwave radiometric mapping of an ocean polar front, exploratory experiments to measure thickness of lake ice, C-Band discrimination between first year and multiyear sea ice, and the first measurements of frequency sensitive characteristics of sea ice.

Background of Microwave Radiometers

The first microwave radiometer used for geophysical measurements was developed by Dicke (1946), and it was used to measure water vapor in the atmosphere. This radiometer used a design technique in which the received noise power was modulated by switching between a reference noise temperature and the antenna input. The Dicke switching eliminates the large receiver noise component and improves radiometer performance. The effect of gain fluctuations is also reduced. If the received noise could be made equal to the reference noise, a null balance condition occurred, and the requirement of an accurate knowledge of radiometer gain was eliminated. Radiometers were developed shortly after the Dicke radiometer which added noise to the received noise to achieve a balance condition (Ryle and Vonberg, 1948). Closed-loop feedback systems were added to the noise injection radiometer to maintain a balance condition as the input noise changed (Seling, 1962). Both electromechanical and electronic feedback systems were built and tested (Goggins, 1967).

The requirement to measure ocean surface temperature with an absolute accuracy of 1 K from a satellite on a global, all weather, and day night basis resulted in a design of a precision microwave radiometer which utilized closed-loop noise feedback (Hidy, et al., 1972). A 2.65 GHz precision microwave radiometer with the microwave front end placed in a constant temperature enclosure was built (Hardy, et al., 1974). Subsequently, a 1.4 GHz precision microwave radiometer using the same design technique was built at the Langley Research Center (Blume, et al., 1978). A design of a stepped frequency microwave radiometer, which operated at five fixed frequencies in a fixed mode, was proposed for improved measurement of geophysical parameters (Love, et al., 1975).

The design technique selected for the SFMR is based on the 2.65 GHz precision microwave radiometer (Hardy, et al., 1974) and the design by Love (1975). The design utilizes a noise injection, closed-loop feedback system, where noise pulses are added to the received electromagnetic radiation to achieve a null balance in a Dicke switched radiometer. The low loss microwave front end is contained within a constant temperature enclosure. The SFMR can operate at any frequency between 4.5 GHz and 7.2 GHz with one of four bandwidths and six integration times. It can operate in either a fixed frequency or a frequency scanning mode. The operation of the SFMR is controlled by a microprocessor based digital controller. The noise injection design technique with a closed-loop feedback system in a balanced Dicke switched microwave radiometer and the use of a constant temperature enclosure for the microwave front end provide the required accuracy and stability. The frequency stepping, multiple bandwidths and integration times, and the digital controller provide the required versatility.

Background of Microwave Radiometer Remote Sensing Measurements

Microwave radiometers have been used from aircraft and satellites to measure geophysical parameters such as sea surface temperature, salinity, and windspeed. Also, various geophysical parameters associated with sea ice, lake ice, and snow have been measured. The importance of these measurements to the understanding of climates, global food production, and energy sources has resulted in many scientific remote sensing experiments using microwave radiometers. Some of these experiments are summarized in the following paragraphs and provide the justification for this research.

The measurement of sea surface temperature and salinity is of vital importance to the fishing industry, marine transport industry, oceanographers, and marine meteorologists. Sea surface temperatures have been measured from an aircraft to an accuracy of 1° C (Blume, et al., 1977). Sea surface temperatures have been measured from the Seasat satellite using the Scanning Multichannel Microwave Radiometer (SMMR) (Gloersen and Barath, 1977) with a standard deviation of 1.5° C and a bias error of 3° C to 5° C (Lipes, et al., 1979). The SFMR has measured the sea surface temperature across the Grand Banks ocean front to an accuracy of 1° C (Delnore, et al., 1980). Salinity measurements have been made in the Gulf of Mexico to an accuracy of 2 o/oo (Thomann, 1976) and in the Chesapeake Bay to an accuracy of 1 o/oo (Blume, et al., 1978).

The capability of measuring sea surface windspeed from a satellite would provide important information to climate studies and the marine transportation industry. The increase in radiometric brightness temperature with windspeed has been measured in many experiments (Hollinger, 1970 and 1971; Nordberg, et al., 1971; Webster, et al., 1976; Wilheit and Fowler, 1977; and Swift, 1974). However, the development of a reliable and accurate model to predict the increase in radiometric brightness temperature as a function of windspeed is an area requiring continued research and experiments.

Microwave radiometers on the NASA CV-990 aircraft measured the radiometric brightness temperature of lake ice at Bear Lake in Utah during March 1971 (Schmugge, et al., 1973). Ice on Chandalor Lake in Alaska was measured in 1975 by the NASA CV-990 aircraft. Walden Reservoir in Colorado was measured in 1977 by microwave radiometers on the NASA P-3 aircraft. Analysis of these data indicated that the brightness temperature decreased with decreasing ice thickness (Hall, et al., 1978). Radiometer measurements of low salinity sea ice in the Gulf of Bothnia located between Finland and Russia demonstrated that ice thickness can be determined from a 600 MHz radiometer (Tiuri, et al., 1978).

The scientific study of the geophysical characteristics and processes involving sea ice is important to the understanding of global weather and climate systems. The demand for natural resources, i.e., energy, minerals, fresh water, and food, necessitates an increased activity in the polar regions of the Earth. Exploitation of these resources is complicated by the hazards associated with sea ice, permafrost, icebergs, and other ice forms. The importance of ice research is such that a multidisciplinary, international program of coordinated investigations of the ice and snow masses of the Earth have been initiated. This program is the Ice and Climate Experiment (ICEX) (Campbell, et al., 1979). The scientific objective of ICEX is a clearer understanding of the roles of ice and snow in geophysical processes.

The application of microwave radiometers to the remote sensing of sea ice from satellites is important since the polar regions are either cloud covered or in darkness 90 percent of the time. The microwave radiometer provides the capability for all weather, day night observations of sea ice in the polar regions. The first sea ice microwave radiometer remote sensing experiments were conducted in the Beaufort Sea using the NASA CV-990 aircraft. These measurements were in conjunction with the Arctic Ice Dynamics Joint Experiment (AIDJEX) during 1971 and 1972 (Campbell, et al., 1973). These measurements confirmed the feasibility of identifying first year and multiyear ice from radiometric brightness temperature measurements above 10 GHz (Gloersen, et al., 1973). The AIDJEX main experiment was conducted between April 1975 and May 1976 in which a comprehensive microwave sensing program was performed on the sea ice of the Beaufort Sea (Campbell, et al., 1978). Measurements were obtained of dielectric properties (Vant, 1976) and radiometric brightness temperature of first year and multiyear ice (Gloersen, et al., 1978).

Overview

The purpose of this section is to provide a brief overview of this dissertation highlighting the author's original research contributions. Throughout this dissertation, it is the intent of the author to provide sufficient background material and references to previous research such that this work will prove valuable to other researchers. Original work is generally associated with an absence of cited reference material.

Chapter II outlines the development of the equations for the radiometric brightness temperature, atmospheric contributions, and the emissivity of water and ice surfaces. A significant new contribution of this research is to utilize existing theory to show that the unique variable frequency SFMR should be capable of measuring sea ice thickness. Also, the author shows that corrections for atmospheric water vapor can be made using the variable frequency technique.

Chapter III presents the development of the design techniques used in the SFMR. The author brought together existing techniques for precision stable performance with the new concepts of variable frequency, bandwidth, and integration time to design this unique radiometer. A detailed design description is presented along with the development of original computational techniques for calibration and data analysis.

Algorithms and computational techniques developed by the author during this research are presented in Chapter IV. These include a simplified algorithm to accurately predict the radiometric brightness temperature at the radiometer input. Based on the computational speed and accuracy of the algorithm, significant empirical data can be developed for windspeed corrections to the measurements of sea surface temperature.

Chapter V presents the results of field experiments which the author conducted during the past two years. Although the inversion technique to determine the geophysical parameters from the radiometric brightness temperature has not been completed, the results of these experiments show that the unique variable frequency capability and versatility of the precision SFMR will provide significant contributions to the geophysical understanding of ocean and ice processes.

CHAPTER II

THEORETICAL ANALYSIS

Radiative Transfer Equation

Electromagnetic radiation is emitted by matter which has been heated to a temperature above absolute zero. The amount of blackbody radiation in the microwave frequency region of interest, $10^8 < f < 10^{10}$ Hz, emitted by matter can be determined from the Rayleigh-Jeans approximation to Planck's Radiation Law (Reeves, 1975). The error due to this approximation is derived in Appendix A. The amount of electromagnetic radiation from matter which is not a blackbody is a function of the emissivity of the material. The emissivity e is a factor less than unity and is a function of several parameters including chemical composition, temperature, frequency, surface characteristics, and viewing angle.

A radiometer is an instrument which detects and provides a measure of the electromagnetic radiation being emitted by a material or surface area within the radiometer's antenna beamwidth. The measured power is determined by (Swift, 1980)

$$P = kT_A \Delta f \tag{2-1}$$

where k is Boltzmann's constant, Δf is the frequency interval or bandwidth of the radiometer, and T_A is the antenna temperature. The antenna temperature is defined by (Swift, 1980)

$$T_A = \frac{1}{4\pi} \int e(\Omega)T(\Omega)G(\Omega)d\Omega \tag{2-2}$$

where e is the emissivity, T is the thermodynamic temperature, and G is the antenna gain. The quantity T_B is defined (Swift, 1980) as the radiometric brightness temperature of the material or surface being measured and is determined by

$$T_B(\Omega) = e(\Omega)T(\Omega) \ . \tag{2-3}$$

The microwave radiometer measures antenna temperature (2-2), while the desired quantity is the radiometric brightness temperature (2-3). If the antenna has a narrow beam with very low side lobes, then the problem of inverting an integral equation is avoided and the radiometric brightness temperature can be approximated by the antenna temperature.

The antenna temperature measured by a microwave radiometer viewing the Earth's surface from a platform in the atmosphere is determined by the radiative transfer equation. This equation is used to account for all the electromagnetic radiation contributions to the antenna temperature which are illustrated in Fig. 2-1. These include radiation from space which is propagated through the atmosphere where a portion is absorbed. Then it is reflected by the Earth's surface, absorbed by the atmosphere between the surface and the radiometer antenna, and finally received by the antenna. Similarly, the atmosphere itself radiates both an upwelling and a downwelling component. The upwelling radiation is directly received by the antenna, whereas the downwelling component

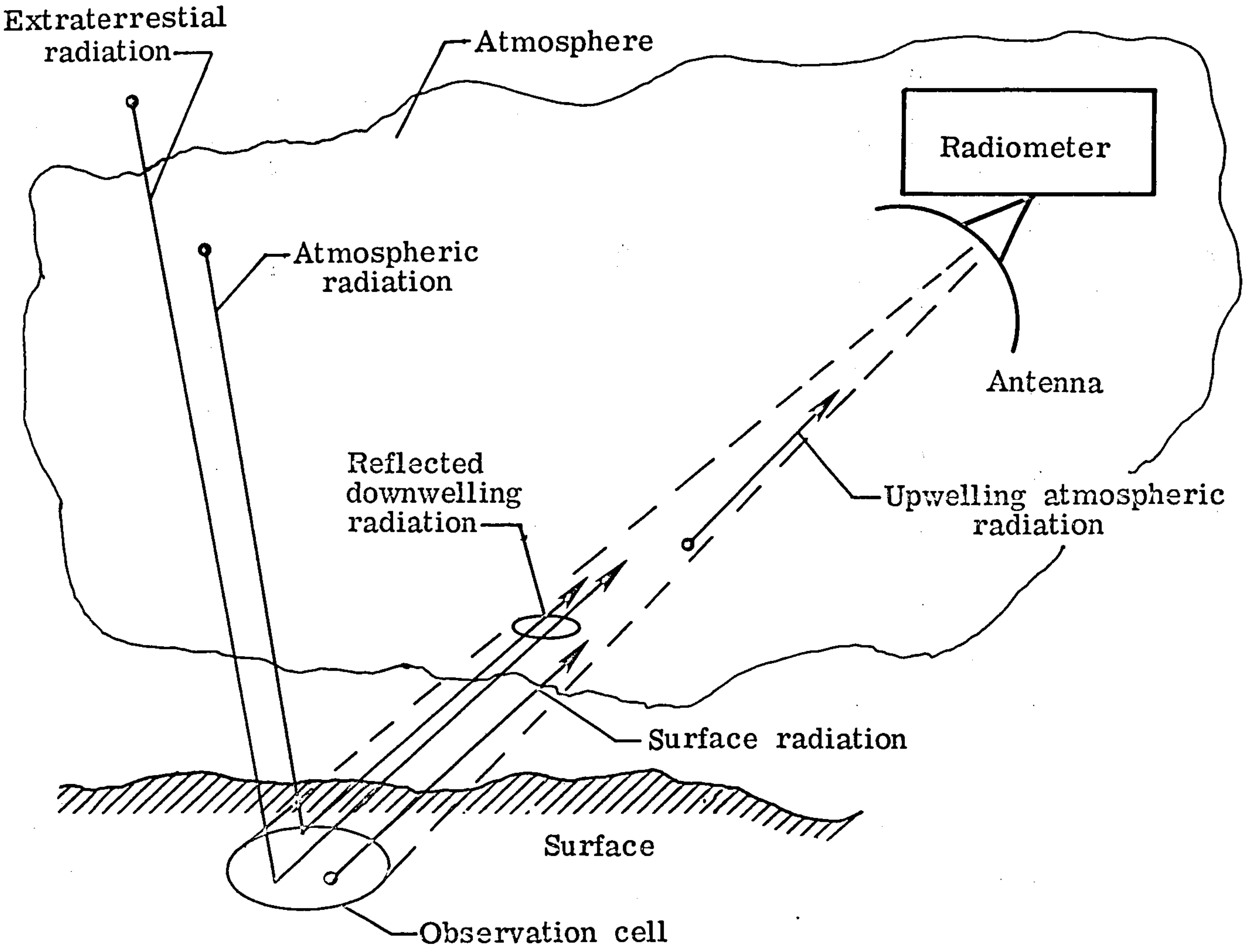

Figure 2-1. Electromagnetic radiation contributions to the radiative transfer equation.

is reflected by the surface and is attenuated by the atmosphere before it is received by the antenna. Finally, the surface itself emits thermal radiation which is also attenuated by the atmosphere prior to being received.

Since the power leaving a boundary between two regions of different electrical properties is equal to the incident power P_i upon the boundary, then the incident power must equal the absorbed power P_a plus the reflected power P_r. For reasons that will become evident, a dimensionless quantity, the power reflection coefficient $|R|^2$ is defined as follows:

$$|R|^2 = \frac{P_r}{P_i} \tag{2-4}$$

where R is defined as the reflection coefficient. Since

$$P_r = P_i - P_a \tag{2-5}$$

then (2-4) can be rewritten as:

$$|R|^2 = 1 - \frac{P_a}{P_i}. \tag{2-6}$$

The ratio of the absorbed power to the incident power can be defined as an absorptance. According to Kirchhoff's Law (Reeves, 1975) absorptance is equal to emissivity and (2-6) becomes

$$|R|^2 = 1 - e\,. \tag{2-7}$$

It therefore follows that the power leaving the surface, expressed as a brightness temperature, is equal to the power emitted by the surface,

eT_S, plus the power reflected by the surface, $(1 - e)T_{B_i}$, or (Wilheit and Fowler, 1973)

$$T_{B_S} = eT_S + (1 - e)T_{B_i} \tag{2-8}$$

where e is the surface emissivity, T_S is the surface thermodynamic temperature, and T_{B_i} is the temperature which corresponds to the radiation incident upon the surface.

The incident radiation expressed as a temperature is (Swift, 1980):

$$\begin{aligned} T_{B_i}(f) = {} & T_\infty \exp\left[-\sec\theta \int_0^\infty \alpha_a(z,f)dz\right] \\ & + \int_0^\infty \alpha_a(z,f)T(z) \exp\left[-\sec\theta \int_0^z \alpha_a(z',f)dz'\right] \sec\theta\, dz \end{aligned} \tag{2-9}$$

where T_∞ is the extraterrestrial electromagnetic radiation, α_a is the absorption coefficient, and θ is the incidence angle between the antenna beam and nadir.

The radiation leaving the surface is determined by substituting (2-9) in (2-8). The radiative transfer equation for the remote sensing stepped frequency microwave radiometer becomes (Swift, 1980)

$$\begin{aligned} T_A(f) = {} & \Bigg(e(f)T_S + \left[1 - e(f)\right] \Bigg\{T_\infty \exp\left[-\sec\theta \int_0^\infty \alpha_a(z,f)dz\right] \\ & + \sec\theta \int_0^\infty \alpha_a(z,f)T(z) \exp\left[-\sec\theta \int_0^z \alpha_a(z',f)dz'\right] dz\Bigg\}\Bigg) \\ & \times \exp\left[-\sec\theta \int_0^{h_r} \alpha_a(z,f)dz\right] + \sec\theta \int_0^{h_r} \alpha_a(z,f)T(z) \\ & \times \exp\left[-\sec\theta \int_0^z \alpha_a(z',f)dz'\right] dz \end{aligned} \tag{2-10}$$

where h_r is the altitude of the microwave radiometer above the Earth's surface.

A quantity called opacity or optical thickness is now defined. This quantity is a measure of the total loss or attenuation of electromagnetic radiation as it propagates through a medium. Opacity as a function of altitude is defined as (Reeves, 1975)

$$\tau(z,f) = \int_0^z \alpha_a(z',f)dz' . \tag{2-11}$$

The total one-way opacity through the entire Earth's atmosphere is defined as

$$\tau(\infty,f) = \int_0^\infty \alpha_a(z',f)dz' . \tag{2-12}$$

The contributions to the antenna temperature T_A from the component of brightness temperature $(1 - e)T_{B_i}$ that is emitted from a nonspecular surface, such as a wind driven sea, will be considered small and treated as a correction factor. This correction factor is empirically developed in Chapter IV.

The opacity of the Earth's atmosphere in the absence of rain and in the microwave frequency region is in the range $\tau(\infty,f) < 0.02$. The stepped frequency microwave radiometer was operated in a nadir viewing mode with incidence angle less than 5°, $\sec\theta$ is bounded by $1.000 < \sec\theta < 1.004$.

Therefore, the argument of the exponential in (2-10) is much less than 1, and the exponentials in (2-10) can be expanded in power series. The terms above the first order can be neglected. This will produce a worst case error of less than 0.02 K. After expansion of the exponentials and substitution of (2-11) and (2-12) into (2-10) the following result is obtained:

$$
\begin{aligned}
T_a(f) = \Bigg(& e(f)T_S + \Big[1 - e(f)\Big] \Bigg\{ \Big[1 - \sec\theta\tau(\infty,f)\Big] T_\infty \\
& + \sec\theta \int_0^\infty \alpha_a(z,f)T(z)\Big[1 - \sec\theta\tau(z,f)\Big]\,dz \Bigg\} \Bigg) \Big[1 - \sec\theta\tau(h,f)\Big] \\
& + \sec\theta \int_0^{h_r} \alpha_a(z,f)T(z)\Big[1 - \sec\theta\tau(z,f)\Big]\,dz \qquad (2\text{-}13)
\end{aligned}
$$

This is the radiative transfer equation for the stepped frequency microwave radiometer.

A computer program was developed during this research to accurately calculate the antenna temperature using (2-13). This program is described in Appendix B. The application of this program requires the knowledge of the opacity as a function of altitude, the total one-way opacity, thermodynamic temperature distribution of the atmosphere, emissivity of the ocean and ice, and the extraterrestrial brightness temperature. These will be developed in the remaining sections of this chapter.

Atmospheric Absorption and Emission

The absorption and emission of electromagnetic radiation in the Earth's atmosphere at microwave frequencies results from the interaction of this radiation with molecular oxygen, water vapor, nonprecipitating clouds, and rain. The interaction of electromagnetic radiation with atmospheric gases results from one or more dipole resonances located at frequencies f_o which have finite natural linewidths Δf_o. Although the atmosphere is primarily composed of nitrogen, this gas does not exhibit a dipole moment and is therefore transparent to electromagnetic radiation. The resonant frequencies of both oxygen and water vapor occur at sufficiently high frequencies such that the interaction is dominated by the linewidth characteristics. These natural linewidths are broadened by two effects, namely Doppler shifts induced by random thermal motion of the molecules and intermolecular collisions associated with the barometric pressure, both of which are functions of altitude. On the other hand, the interaction with condensed water in the atmosphere is nonresonant in nature and is proportional to the macroscopic loss tangent of water. The attenuation and emission from condensed water is also proportional to the liquid water content distribution, which is reasonably homogeneous in clouds. Rainfall, however, exhibits a rather complicated spatial distribution and the radiating properties are difficult to quantify. Consequently, the effects of rain will not be considered for this reason and because the data collected in support of this research were generally taken in the absence of rain.

The absorption from the oxygen molecule results from a large number of different spectral lines closely spaced in the frequency region of 50 to 60 GHz and a nonresonant continuum. The absorption coefficient α_{O_2} can be obtained from the Van Vleck-Weisskopf formula (Love, et al., 1975):

$$\alpha_{O_2} = \frac{61.2P}{T^3} f^2 \Delta f_o \left[\frac{1}{(60 - f)^2 \div \Delta f_o^2} + \frac{1}{(60 + f)^2 + \Delta f_o^2} + \frac{1}{f^2 + \Delta f_o^2} \right] . \tag{2-14}$$

The absorption coefficient α_{O_2} has units of nepers per meter and is a function of barometric pressure P and thermodynamic temperature T. The linewidth Δf_o is (Love, et al., 1975)

$$\Delta f_o = 0.62P\left(\frac{300}{T}\right)^{0.70} . \tag{2-15}$$

The absorption coefficient α_{WV} due to water vapor consists of contributions from a resonant spectral line at 22.235 GHz and the edge effects of several lines located in the submillimeter wavelength frequency region. The following equation for the absorption coefficient is based on the Van Vleck-Weisskopf formula for the 22.235 GHz line and a correction factor for the effects of the higher frequency lines (Love, et al., 1975):

$$\alpha_{WV} = 0.3427\ \rho_W \exp\left(\frac{-644}{T}\right) \frac{f^2\ \Delta f_o}{T^{2.5}} \left[\frac{1}{(22.235 - f)^2 + \Delta f_o^2} + \frac{1}{(22.235 + f)^2 + \Delta f_o^2} \right] + 2.55 \times 10^{-6}\ \rho_W \frac{f^2\ \Delta f_o}{T^{1.5}} . \tag{2-16}$$

The absorption coefficient α_{WV} also has units of nepers per meter. The linewidth Δf_o is (Love, et al., 1975)

$$\Delta f_o = 2.58 \times 10^{-3}\left(1 + \frac{1.47 \times 10^{-2}\ \rho_W T}{P}\right) P \left(\frac{318}{T}\right)^{0.625} . \qquad (2\text{-}17)$$

The water vapor density ρ_W used in (2-16) and (2-17) varies with altitude and can be estimated from the barometric equation:

$$\rho_W = \rho_{W_o} \exp(-h/s_h) \qquad (2\text{-}18)$$

where ρ_{W_o} is the water vapor density at the surface and s_h is the scale height for water vapor. Both of these quantities are quite variable with time of year, location on the Earth, and even diurnally.

The absorption coefficient α_{CL} for nonprecipitating clouds is a function of the liquid water content of the clouds L, the real and imaginary components of the complex dielectric constant, ε' and ε'', respectively, for liquid water at the cloud temperature, the frequency of the electromagnetic radiation f, and the water density ρ. The absorption coefficient in nepers per meter can be determined from an expression (Love, et al., 1975) which was derived through the use of the Rayleigh approximation for small particles to Mie's solution of Maxwell's equations for dielectric spheres. The result is

$$\alpha_{CL} = \frac{1.8 \times 10^{-3}\ L\varepsilon''\pi f}{c\rho\left[(\varepsilon' + 2)^2 + (\varepsilon'')^2\right]} . \qquad (2\text{-}19)$$

The liquid water content L, cloud temperature, cloud base altitude, and cloud thickness are functions of the cloud type. Cloud models have been developed which can be used to estimate these variables. The location and type of cloud is a highly variable function of location and time. Therefore for the purposes of this research, a cloud correction factor based on (2-19) and the referenced cloud models is developed in Chapter IV and is applied where necessary.

The total absorption coefficient $\alpha_a(z,f)$, in the absence of rain and deferring nonprecipitating cloud effects to a cloud correction factor, is the sum of the absorption coefficient due to oxygen α_{O_2} and water vapor α_{WV}. The opacity as a function of altitude $\tau(z,f)$ and total opacity $\tau(\infty,f)$ can be calculated using (2-14) and (2-16). The atmospheric temperature variation $T(z)$ is obtained from the <u>1976 U.S. Standard Atmosphere</u>.

The magnitude of the effects of atmospheric absorption by oxygen and water vapor can best be illustrated in terms of the change in brightness temperature with the presence of either constituent. This change is calculated using the radiative transfer equation program described in Appendix B with the absorption coefficients due to oxygen and water vapor, respectively, set equal to zero. This removes the atmospheric absorption and emission effects. Then the equation is solved adding each absorption coefficient separately, and the resultant change in brightness temperature is then computed. The change in brightness temperature as a function of altitude from the surface to 50 km, surface temperature variation of from 0° C to 30° C, frequencies from 4 to 8 GHz, water vapor densities from 1 to 5 g/m^3, and scale height of water vapor density variation from 1 to 5 km were considered. These ranges represent the atmospheric conditions typically encountered during this research. At altitudes above 20 km, there is virtually no change in the absorption due to either species.

The computed change in brightness temperature due to oxygen as a function of frequency and surface temperature is given in Table 2-1. The change is virtually independent of frequency because the major contribution in this frequency range is the nonresonant oxygen line. A decreasing change in brightness temperature with increasing surface temperature is observed because the attenuation of the surface radiation due to oxygen absorption increases at a faster rate than does the emission from the atmosphere due to oxygen absorption.

TABLE 2-1

CHANGE IN BRIGHTNESS TEMPERATURE (K) DUE TO ATMOSPHERIC OXYGEN AT AN ALTITUDE OF 20 KILOMETERS

Surface temperature (°C)	Frequency (GHz)				
	4	5	6	7	8
0	2.08	2.08	2.08	2.08	2.08
10	1.88	1.89	1.89	1.90	1.91
20	1.70	1.71	1.71	1.72	1.73
30	1.55	1.55	1.56	1.56	1.57

The computed change in brightness temperature due to oxygen as a function of altitude is shown in Fig. 2-2. The majority of data gathered during this research was taken at altitudes between 500 and 1000 m or at 6 km. This figure shows that knowledge of the surface temperature to within a few degrees is sufficient to predict the oxygen contributions to within 0.1 K.

The computed change in brightness temperature due to water vapor, although only one-fourth the magnitude of the oxygen induced change, is potentially a more serious problem as indicated in Table 2-2. The change in brightness temperature is a significant function of frequency because the absorption is dominated by the resonant line located nearby at 22 GHz and the skirts are consequently fairly steep in the 4 to 8 GHz region. The fact that the water vapor contribution is a predictable function of frequency suggests that the SFMR can self correct for the water vapor contribution. This can be accomplished by alternately collecting data at widely separated frequencies.

TABLE 2-2

CHANGE IN BRIGHTNESS TEMPERATURE (K) DUE TO ATMOSPHERIC WATER VAPOR AT AN ALTITUDE OF 20 km, WATER VAPOR DENSITY OF 10 g/m^3, AND SCALE HEIGHT OF 5 km

Surface temperature (°C)	Frequency (GHz)				
	4	5	6	7	8
0	0.22	0.34	0.49	0.68	0.89
10	.21	.33	.48	.67	.88
20	.21	.33	.47	.65	.86
30	.20	.32	.46	.63	.84

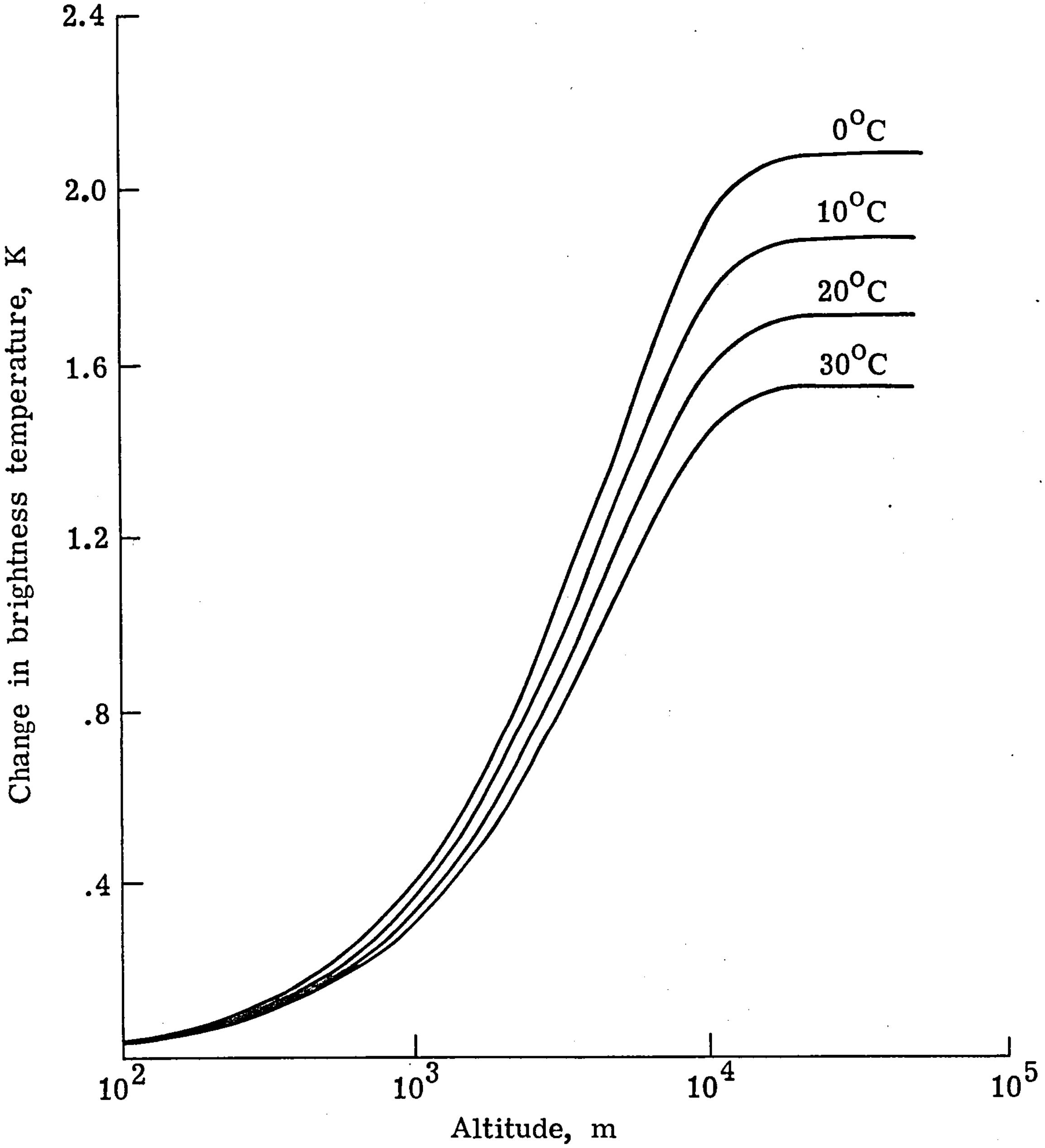

Figure 2-2. Change in brightness temperature from oxygen in the atmosphere as a function of altitude and surface temperature.

The brightness temperature is almost independent of surface temperature in the 4 to 8 GHz frequency region; however, Fig. 2-3 shows that the brightness temperature varies significantly with water vapor density and scale height. These effects are illustrated as a function of altitude for an assumed frequency of 6 GHz and a surface temperature of 10° C. Variations of water vapor density from 1 to 10 g/m^3 produce changes in brightness temperature from 0.04 to 0.43 K at 6 km. Variations in scale height from 1 to 5 km for a fixed water vapor density of 10 g/m^3 produce changes in brightness temperature from 0.13 to 0.43 K at 6 km.

Because of the global and temporal variations in density and scale height, the achievement of the desired accuracy could be problematic if supplemental knowledge of these two parameters is not available during the operation of the instrument. When operating in a single frequency mode, the data should be collected at altitudes as low as possible to minimize these effects. Measurements made at 500 m will keep the uncertainty due to water vapor absorption below 0.1 K. Table 2-2 suggests that higher altitude operation will require collecting data at two extreme frequencies in order to correct for water vapor when supplemental data are not available.

Thermal Emission From Natural Surfaces

The thermal emission from a natural surface is determined by the thermodynamic temperature and emissivity which, in turn, is a first order function of the complex dielectric constant and a second order

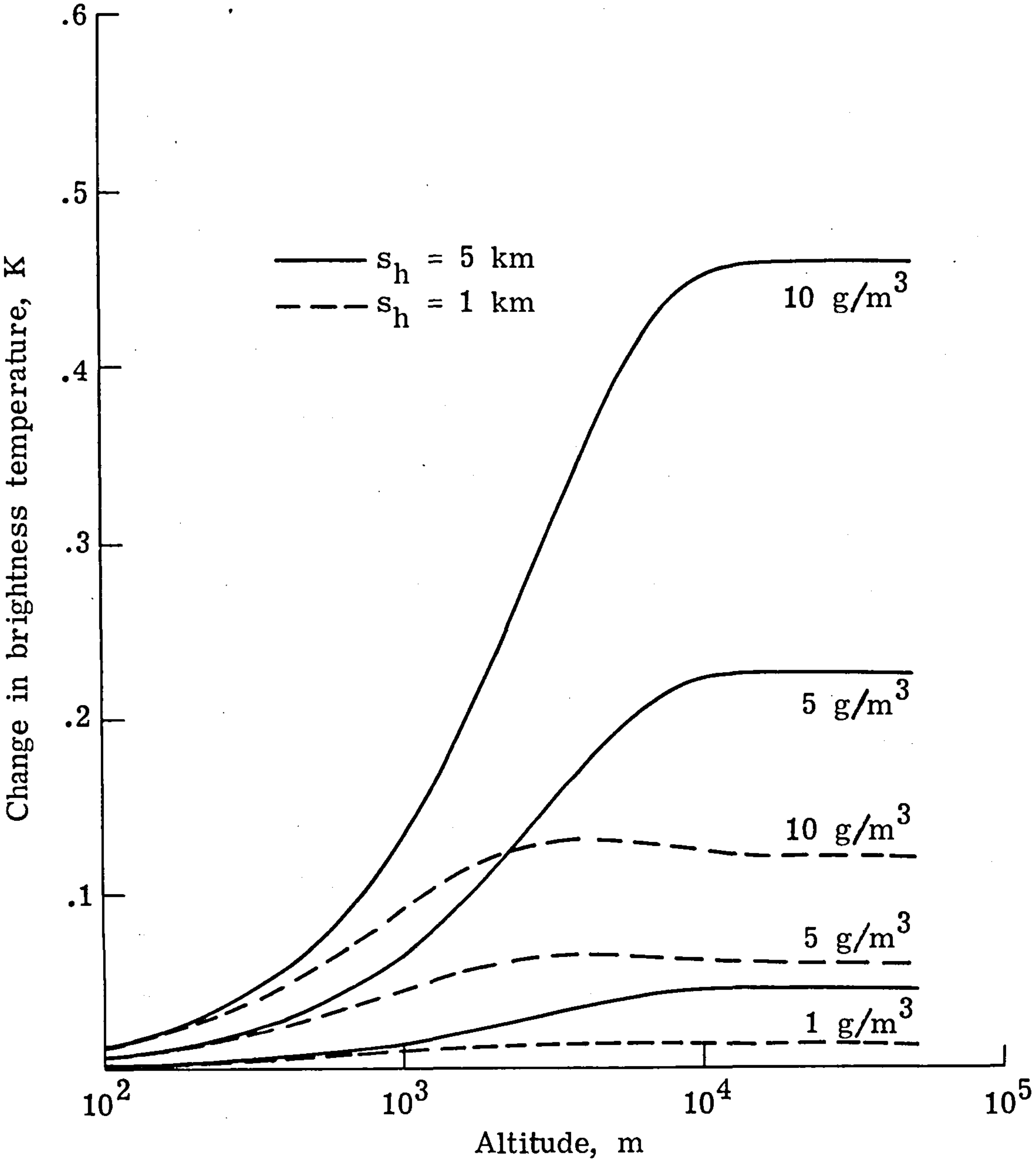

Figure 2-3. Change in brightness temperature from atmospheric water vapor versus altitude, water vapor density, and scale height for a surface temperature of 10° C and frequency of 6 GHz.

function of surface roughness. The first order effects can be quantitatively described; however, theoretical difficulties require empirical corrections to the second order roughness contributions.

The natural surfaces encountered during this research fall into two categories. The first category are those whose loss properties and depths are such that the interaction can be described by the reflection from a boundary between two semi-infinite dielectric media. The two examples considered are the ocean and lossy thick ice encountered in the polar regions of the Earth. The second category consists of a layer of dielectric medium of thickness d separating two semi-infinite dielectrics. Examples here include lake ice over fresh water and foam patches on the ocean surface. The skin depth is the connection between these two problems.

Skin depth is defined as the thickness of a lossy medium at which the amplitude of a plane wave propagating in that medium decreases to 1/e or 0.3659 of the initial amplitude. The accuracy goal of this research is to measure 0.1 K out of 300 K or approximately 3 parts in 10^4. When a plane wave has traveled ten skin depths, it has been attenuated to a value less than 3 parts in 10^4. Therefore, when the layer thickness is equal to or greater than ten skin depths, it can be considered a semi-infinite medium and the second case simplifies into the first case.

The emissivity of the layered dielectric medium over a semi-infinite dielectric medium is derived from the power reflection coefficient using (2-7). The complex reflection coefficient R is related to the power reflection coefficient by:

$$|R|^2 = RR^* \tag{2-20}$$

where R^* is the complex conjugate of R. The reflection coefficient of a plane wave incident upon the dielectric layer over a semi-infinite dielectric medium is derived from Maxwell's equations through the solution of the boundary value problem shown in Fig. 2-4. Region 1 is the space above the surface and can be approximated as a vacuum. Regions 2 and 3 are dielectric media with permeabilities equal to that of a vacuum.

The reflection coefficient is the ratio of the reflected wave in region 1 to the incident wave in region 1. The incident wave can have any orientation relative to the plane of incidence; however, solution of the boundary value problem for an arbitrary orientation is cumbersome. The arbitrary orientation can be resolved into two orthogonal components, one where the electric field vector is normal to the plane of incidence (horizontal polarization) and one where the electric field vector lies in the plane of incidence (vertical polarization).

The choice of expressing the boundary conditions in terms of the electric field vector or the magnetic field vector depends on the polarization. For horizontal polarization, the electric field vector is used and for vertical polarization, the magnetic field vector is used. The solution to the boundary value problem for the two

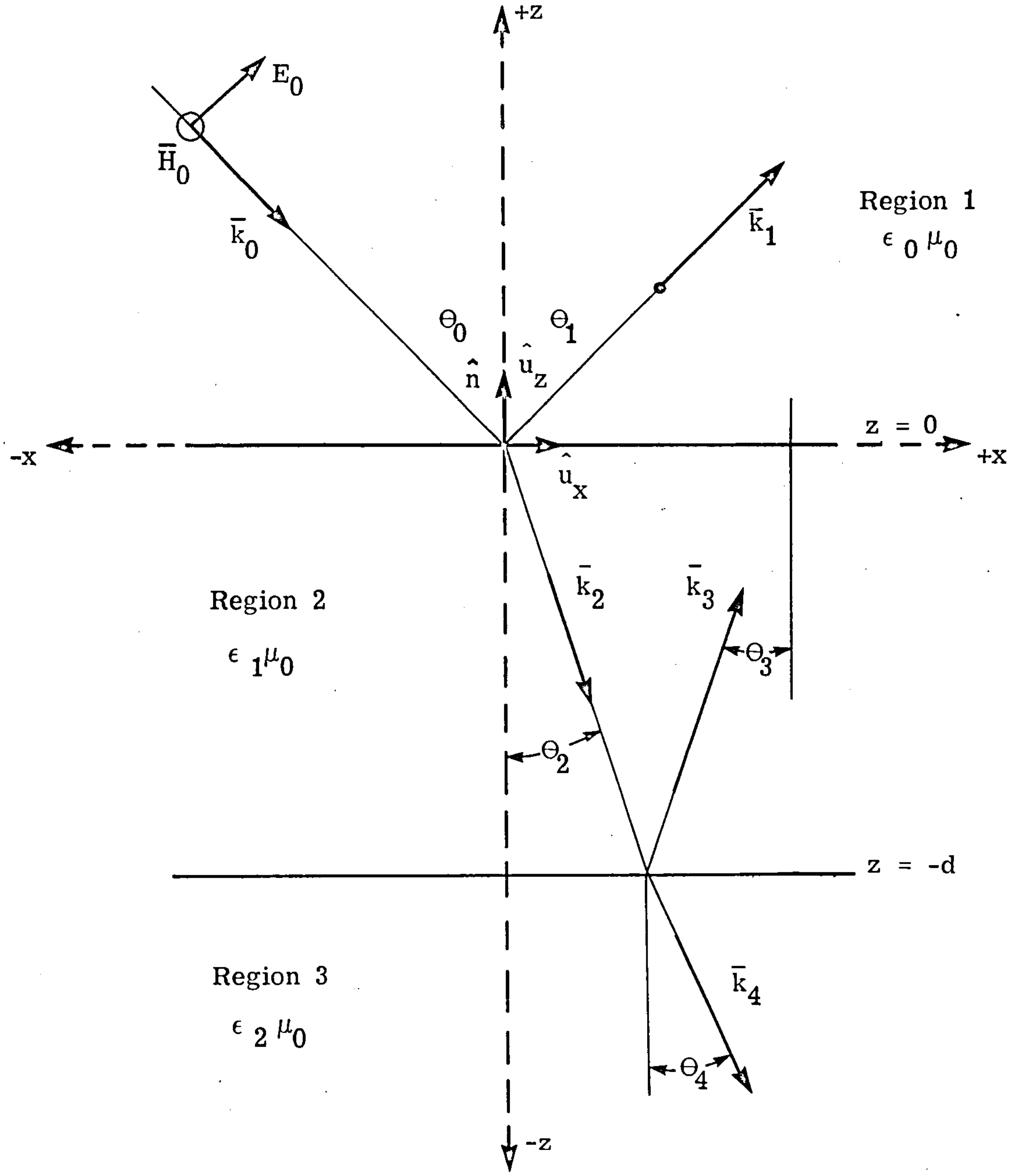

Figure 2-4. Boundary value problem for a dielectric layer over a semi-infinite dielectric medium.

polarizations is well known (Stratton, 1941). The reflection coefficient for horizontal polarization is (Swift, 1980)

$$R_H = \frac{R_{12H} + R_{23H} \exp(j2\gamma d)}{1 + R_{12H}R_{23H} \exp(j2\gamma d)} \qquad (2\text{-}21)$$

where R_{nmH} is the reflection coefficient between regions n and m for horizontal polarization. The reflection coefficient is obtained using Maxwell's curl equation from the magnetic field vector reflection coefficient for vertical polarization and is given by (Swift, 1980)

$$R_V = \frac{R_{12V} + R_{23V} \exp(j2\gamma d)}{1 + R_{12V}R_{23V} \exp(j2\gamma d)} \qquad (2\text{-}22)$$

where R_{nmV} is the reflection coefficient between regions n and m for vertical polarization. The propagation constant γ in (2-21) and (2-22) is the effective propagation constant of the layered dielectric medium. It is a function of the complex dielectric constant of the layered dielectric medium ε_1 and is given by

$$\gamma = \left[\mu_0\omega^2\left(\varepsilon_1 - \varepsilon_0 \sin^2 \theta_0\right)\right]^{1/2} . \qquad (2\text{-}23)$$

It is important to note that the imaginary part of the complex dielectric constant ε_1 will create a real argument in the exponential which becomes a damping term. The real part of the complex dielectric constant is the phase term and the exponential oscillates between +1 and -1 as the imaginary part of the argument varies.

The attenuation coefficient resulting from the damping term at normal incidence is related to the complex dielectric constant by (Reeves, 1975)

$$\alpha = 8.686\left(\frac{2\pi}{\lambda}\right)\left(\left(\frac{\varepsilon'}{2}\right)\left\{\left[1 + \left(\frac{\varepsilon''}{\varepsilon'}\right)^2\right]^{1/2} - 1\right\}\right)^{1/2} \tag{2-24}$$

where α is the attenuation coefficient in dB/m and ε' and ε'' are the real and imaginary parts of the complex dielectric constant.

The reflection coefficients R_{12H}, R_{12V}, R_{23H}, and R_{23V} are the Fresnel reflection coefficients of a dielectric boundary and are given for horizontal and vertical polarizations respectively by (Swift, 1980)

$$R_{mnH} = \frac{\cos\theta_0 - \left[\left(\frac{\varepsilon_n}{\varepsilon_m}\right) - \sin^2\theta_0\right]^{1/2}}{\cos\theta_0 - \left[\left(\frac{\varepsilon_n}{\varepsilon_m}\right) - \sin^2\theta_0\right]^{1/2}} \tag{2-25}$$

and

$$R_{mnV} = \frac{\left(\frac{\varepsilon_n}{\varepsilon_m}\right)\cos\theta_0 - \left[\left(\frac{\varepsilon_n}{\varepsilon_m}\right) - \sin^2\theta_0\right]^{1/2}}{\left(\frac{\varepsilon_n}{\varepsilon_m}\right)\cos\theta_0 + \left[\left(\frac{\varepsilon_n}{\varepsilon_m}\right) - \sin^2\theta_0\right]^{1/2}}\,. \tag{2-26}$$

The power reflection coefficient, which is real, is the product of the complex reflection coefficient and its conjugate. The emissivity is calculated from the power reflection coefficient using (2-7).

As discussed above, the plane wave propagating in space with an arbitrary polarization was resolved into two orthogonal polarizations, horizontal and vertical. If these two components are equal in amplitude and differ in phase by an odd multiple of 90°, the resultant plane wave in space will have a polarization which rotates, and the tip of the field vector traces out a circle. This polarization state is referred to as circular polarization, and the power reflection coefficient for circular polarization is:

$$|R|^2_{CP} = \frac{1}{2}\left(|R_H|^2 + |R_V|^2\right) \qquad (2\text{-}27)$$

where R_H and R_V are the Fresnel reflection coefficients.

The emissivity for a smooth surface dielectric medium is a function of the complex dielectric constant of the medium and the incidence angle. The emissivity as a function of incidence angle for 4, 6, and 8 GHz is shown in Fig. 2-5 for horizontal, vertical, and circular polarization. The surface is a smooth semi-infinite dielectric medium with a dielectric constant typical of ocean water at a temperature of 5° C and a salinity of 35 o/oo. The vertical polarization increases with incidence angle to a maximum near unity at the Brewster angle, then falls rapidly to zero at 90°. The horizontal polarization falls monotonically from the nadir value to zero at 90°. The circular polarization remains reasonably constant out to 30°, then increases somewhat until the Brewster angle is reached, and then falls rapidly to zero at 90°. The effect of frequency is small and due to the change in the dielectric constant of water.

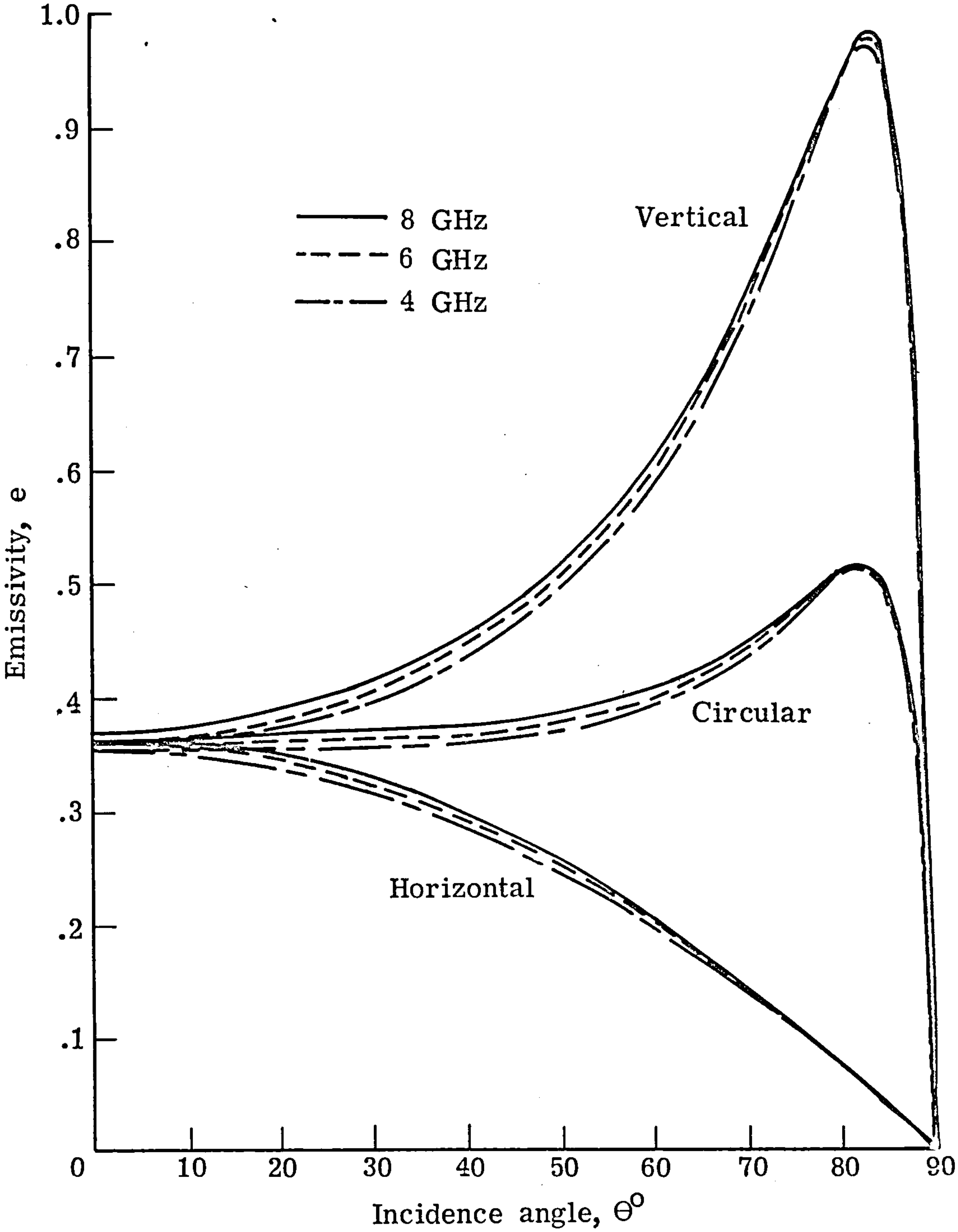

Figure 2-5. Emissivity of sea water at 5° C versus incidence angle at frequencies of 4, 6, and 8 GHz for vertical, horizontal, and circular polarization.

An equation for emissivity at normal incidence of a smooth layered dielectric medium over a semi-infinite dielectric medium is (Apinis and Peake, 1976)

$$e = \frac{(1 - r_i)\left[1 - r_w \exp(-4\alpha d)\right]}{1 + r_i r_w \exp(-4\alpha d) + 2\sqrt{r_i r_w \exp(-4\alpha d)} \cos 2\beta d} . \tag{2-28}$$

The power reflection coefficient of the air-ice boundary r_i and the ice-water boundary r_w is a function of the ratio of the complex dielectric constant of the two media and can be calculated from (2-20) and (2-25) or (2-26). The real part of the propagation constant α is calculated from:

$$\alpha = \frac{2\pi}{\lambda} \operatorname{Im}\left(\sqrt{\varepsilon_M}\right) \tag{2-29}$$

where ε_M is the complex dielectric constant of the layered medium. The imaginary part β is calculated from:

$$\beta = \frac{2\pi}{\lambda} \operatorname{Re}\left(\sqrt{\varepsilon_M}\right). \tag{2-30}$$

For $4\alpha d \geq 10$, the emissivity reaches the value of a semi-infinite layer of ice, $1 - r_i$. However, when $4\alpha d < 10$, the value of emissivity will oscillate where the amplitude of these oscillations is a function of the value of $4\alpha d$. This is a result of the phase term $\cos 2\beta d$ which oscillates between +1 and -1 as the thickness d undergoes quarter-wavelength variations in the medium whose phase constant is β.

The emissivity at normal incidence of ice over water is shown in Fig. 2-6 as a function of ice thickness for an ice attenuation

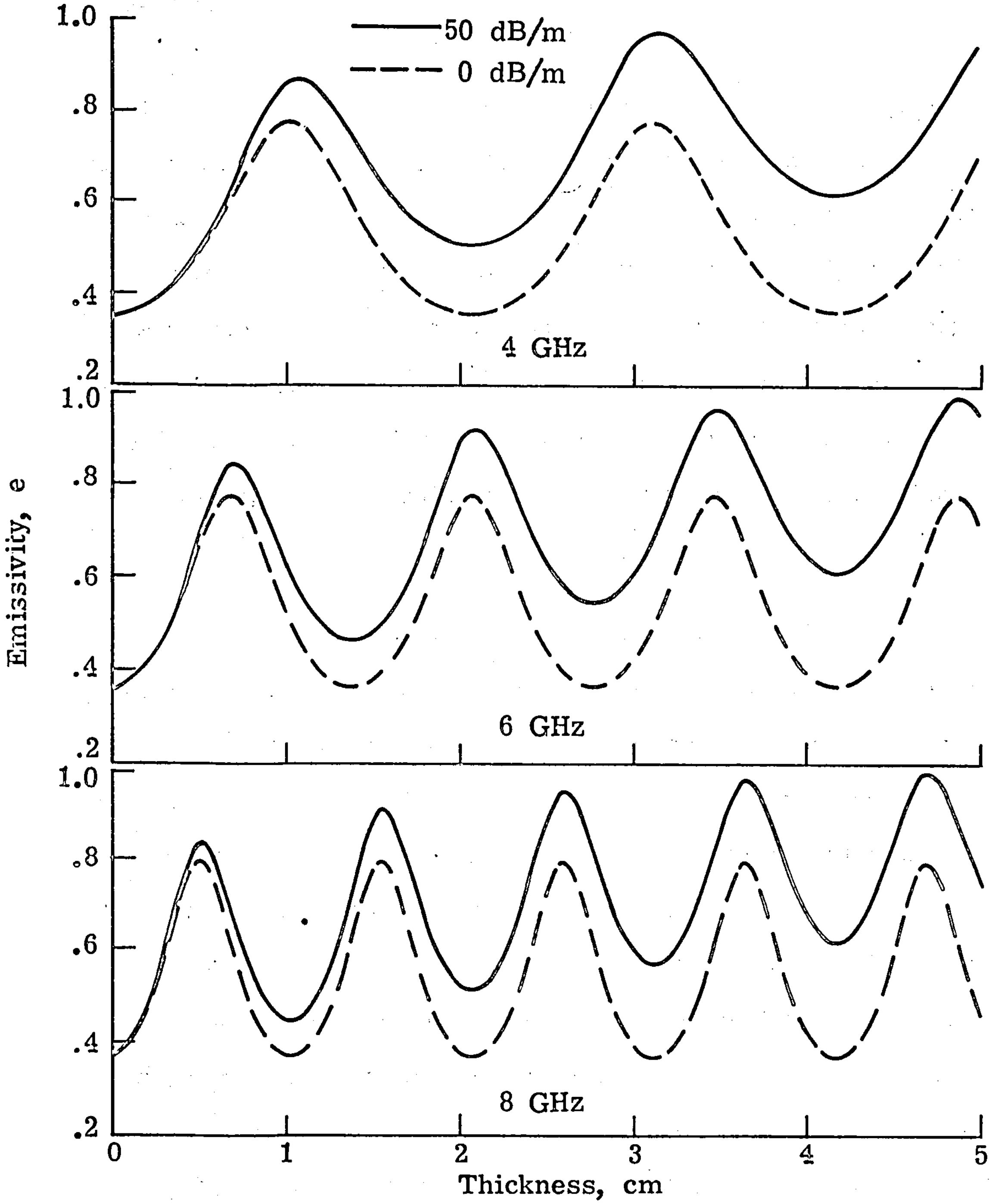

Figure 2-6. Emissivity of an ice layer over water versus thickness at frequencies of 4, 6, and 8 GHz with ice attenuation coefficients of 0 dB/m and 50 dB/m.

coefficient of 0 dB/m and 50 dB/m. Curves which exhibit the quarter-wavelength oscillations are presented for 4, 6, and 8 GHz. The emissivity varies from that of water to near unity depending upon the frequency, thickness and attenuation coefficient. At a fixed thickness of 2 cm, the emissivity varies from 0.36 to 0.77 as frequency is varied from 4 to 8 GHz for the nonlossy ice and from 0.52 to 0.92 for the lossy ice. The quarter-wavelength oscillations in the emissivity are damped out for lossy ice and are clearly illustrated in the 8 GHz curve. The damped oscillations approach the limiting value of the emissivity of a semi-infinite ice medium when the ice thickness exceeds ten skin depths.

Radiating Properties of Water and Ice

The radiating properties of water and ice at a specific thermodynamic temperature is determined by the emissivity. For a smooth surface, the emissivity is directly proportional to the Fresnel reflection coefficients, which are a function of dielectric constant and the known viewing angle. The emissivity of a rough surface is discussed by Peake (1959). A geometric optics model of a rough surface with a gaussian height distribution provides a reasonable description of the ocean. However, other surfaces, such as ice, are much more difficult to model because of the intricate surface statistics.

The complex dielectric constant of sea water is obtained from a model developed for sea water at microwave frequencies (Klein and Swift, 1977). The basis for this model is the Debye expression for polar liquids modified to include the ionic conductivity of the various salts in sea water. The Debye expression is

$$\varepsilon = \varepsilon_\infty + \frac{\varepsilon_s - \varepsilon_\infty}{1 + j\omega\tau} - \frac{j\sigma}{\omega\varepsilon_o} . \tag{2-31}$$

At infinite frequency the dielectric constant is $\varepsilon_\infty = 4.9$. The static dielectric constant ε_s, the relaxation time τ, and the ionic conductivity σ are all functions of the thermodynamic temperature and salinity of the sea water. Expressions have been developed for the static dielectric constant, relaxation time, and conductivity as functions of temperature and salinity based on regression fits to experimental data.

The emissivity as a function of water temperature for both fresh and sea water has been calculated for 4, 6, and 8 GHz using (2-7), (2-20), and (2-25) and the dielectric constant model. The results of these calculations at a viewing angle of 0^o are presented in Fig. 2-7. The differences in emissivity of fresh and sea water increase with decreasing frequency and increasing water temperature.

Because of the relatively simple statistical nature of a wind roughened sea, the geometric optics model has been used to calculate the normalized differential scattering cross section. This model assumes that the large-scale roughness can be approximated by an ensemble of reflecting plane facets, whose areas are much larger than a wavelength. Diffraction is ignored and the resultant normalized differential scattering cross section depends only upon the rms tilt and

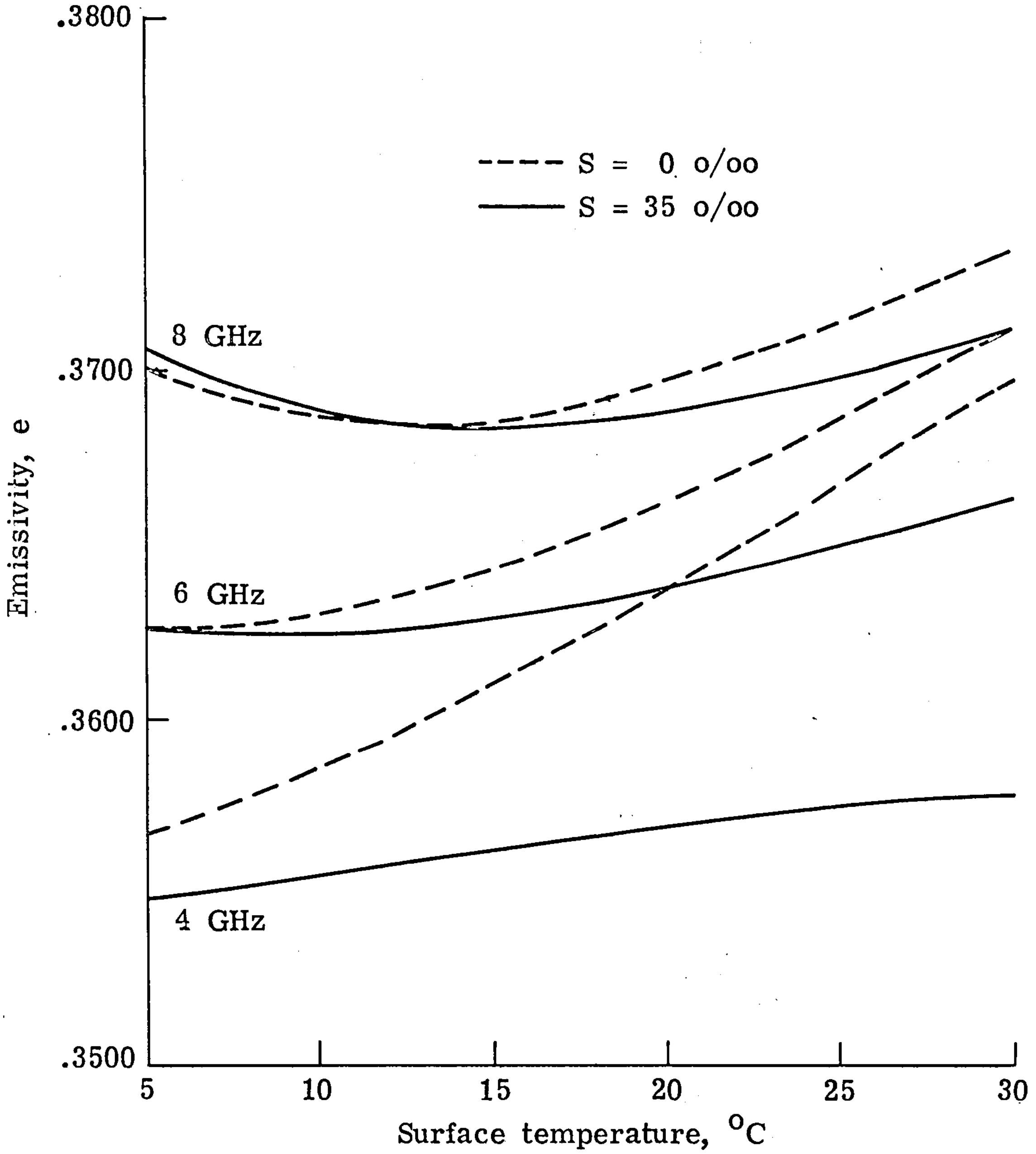

Figure 2-7. Emissivity of fresh water and sea water versus surface temperature at frequencies of 4, 6, and 8 GHz.

dielectric properties of the facet ensemble. Calculations of the emissivity from rough surfaces based on the geometric optics model were first reported by Stogryn (1967). The relationship between windspeed and rms slope of the sea surface was based on sea slope measurements (Cox and Munk, 1954). Measurements of the differences in emissivity between smooth and rough water have been conducted from stationary platforms over bodies of water (Hollinger, 1971, and Swift, 1974). The results of these measurements and theoretical calculations using the geometric optics model are shown in Fig. 2-8. Although the agreement between the calculations and measurements is reasonably good on a qualitative basis, the quantitative results of the theory are insufficient to meet the desired accuracy of this research. Therefore, an empirical correction is developed in Chapter IV based on actual wind and scatterometer measurements.

When the windspeed exceeds approximately 7 m/s, the emissivity exhibits a substantial increase that is not strictly attributed to an increase in surface roughness. Above this windspeed, foam is produced on the sea surface and acts as a matching layer whose average dielectric constant is significantly different from that of the underlying water. The percentage of foam within the surface area illuminated by the radiometer antenna is a function of both the windspeed and fetch. A model to predict the percentage foam coverage has been developed (Ross and Cardone, 1974). The resultant emissivity of a foam covered sea surface neglecting rough surface effects is shown in Fig. 2-9 as a function of

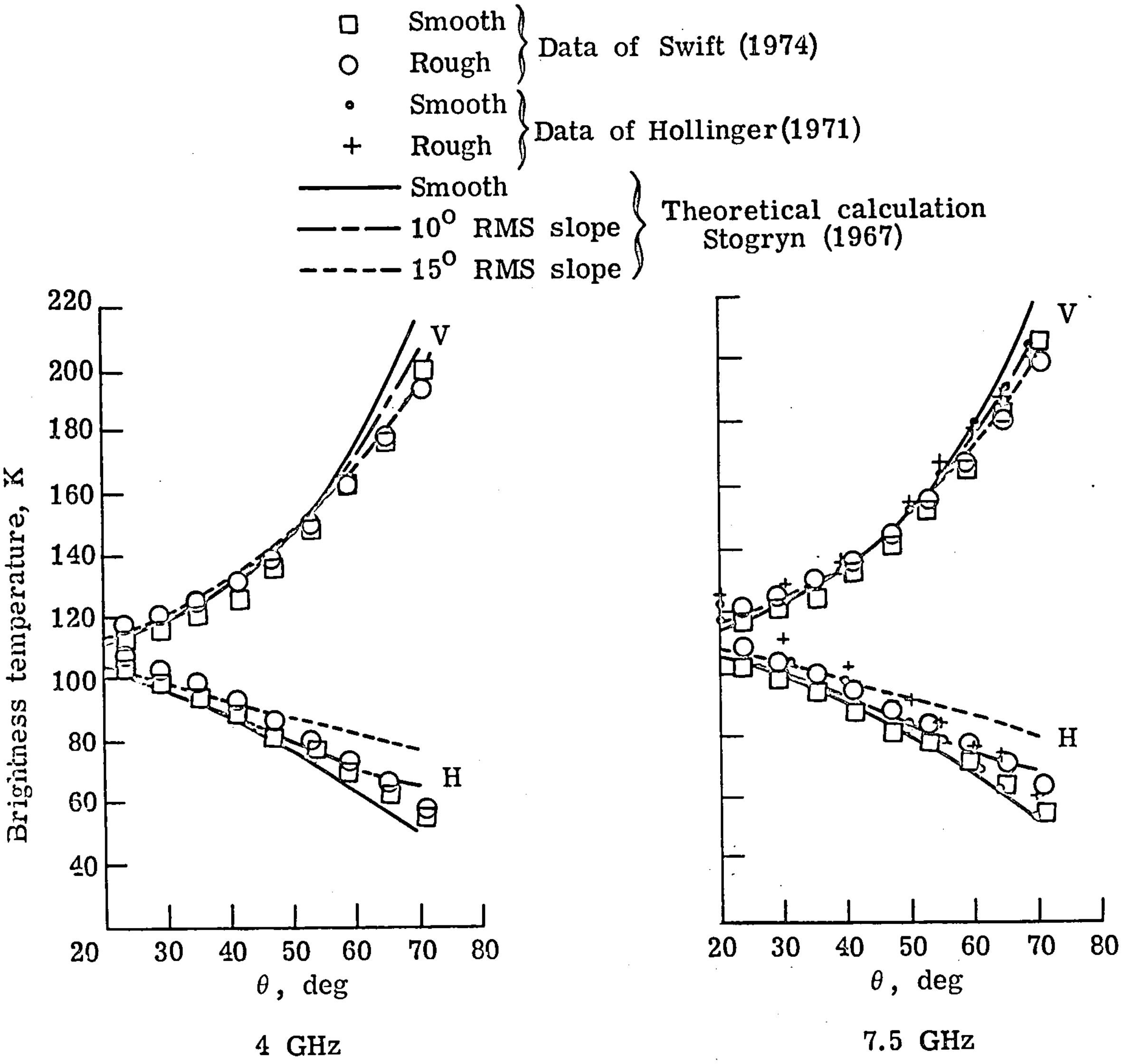

Figure 2-8. Comparison of theoretical and measured radiometric brightness temperatures for smooth and rough surfaces versus incidence angle.

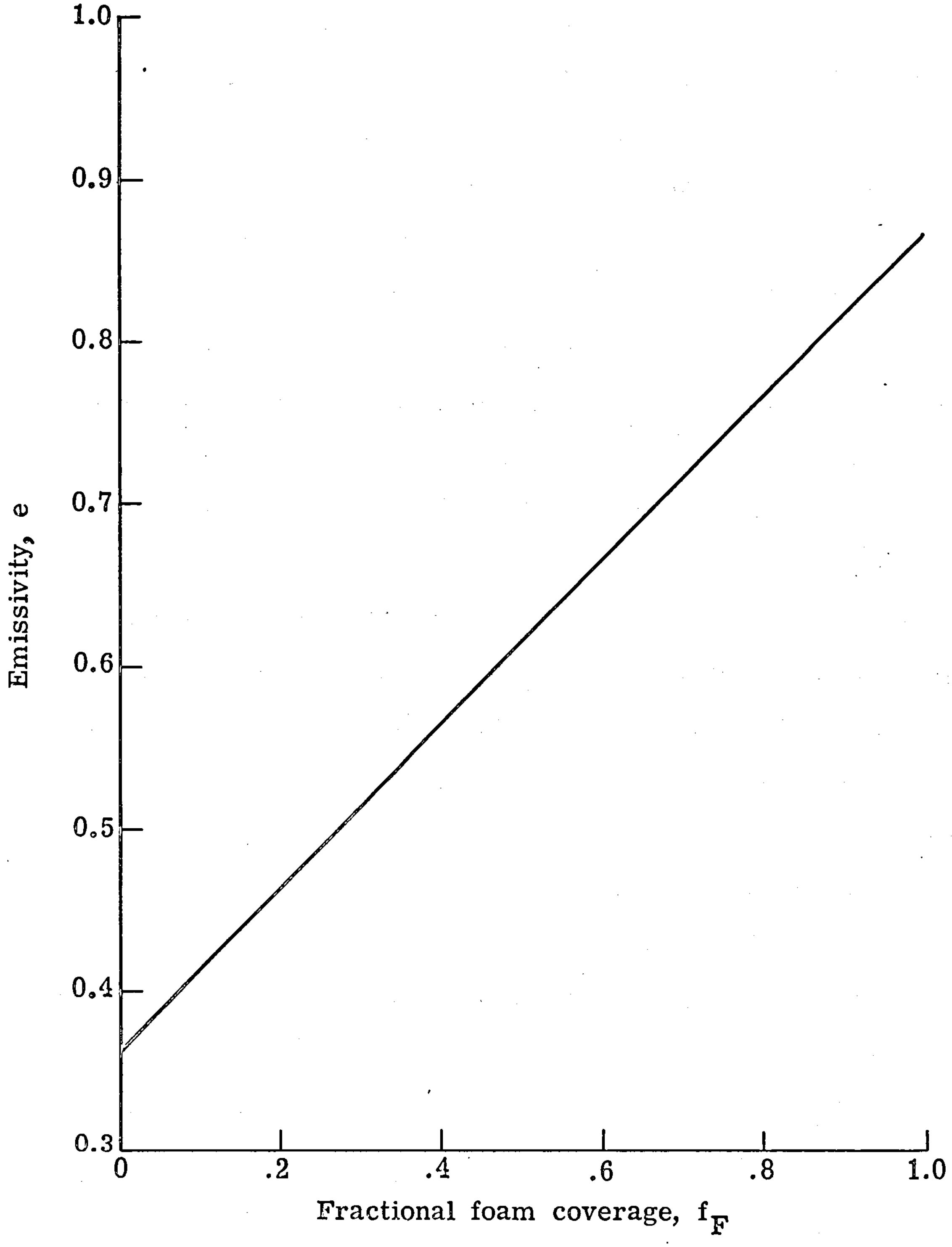

Figure 2-9. Emissivity of a foam covered sea surface versus fractional foam coverage for a foam with 5 percent water, 3 cm thick, and a frequency of 6 GHz.

the fractional foam coverage. The empirical wind correction model presented in Chapter IV includes empirical corrections for foam.

The complex dielectric constant for water has values in the 4 to 8 GHz frequency region ranging from 47 to 76 for the real part and from 12 to 44 for the imaginary part. When water freezes, there is a change in the real and imaginary parts of the dielectric constant since the physical properties undergo a change. The static dielectric constant does not change appreciably; however, the relaxation time becomes very large due to the change of state. The relaxation time goes from typically 20×10^{-12} s for cold water to 5.3×10^{-5} s for ice, a change of seven orders of magnitude.

The real part of the dielectric constant of fresh water ice is 3.14 and is relatively independent of both temperature and frequency at microwave frequencies (Vant, et al., 1974). The imaginary part of the dielectric constant of fresh water ice varies between 0 and 0.006. The imaginary part is a function of temperature, decreasing towards zero as the temperature becomes colder.

The complex dielectric constant of natural and artifically grown sea ice has been measured extensively for many types of sea ice. These measurements were conducted over a frequency range of 100 MHz to 40 GHz and a temperature range from -40° C to -4° C. Both an empirical and theoretical model were developed and comparisons were made with the measured data (Vant, 1976). The real and imaginary parts of the dielectric constant of sea ice are a function of frequency, temperature, salinity, density, brine volume fraction, entrapped ice volume fraction, and ice crystal orientation. The real part varies from 2.5 to 6.0, and the imaginary part varies from 0.003 to near unity in the 4 to 8 GHz frequency region.

The air-ice boundary and the ice-water boundary of a layer of ice over water are usually roughened by stresses associated with the growth process. The effects of these rough surfaces on the oscillatory behavior of the emissivity can be examined through the following development. Equation (2-28) can be expressed as a series by a partial fraction expansion (Apinis and Peake, 1976). The emissivity of an ice layer over semi-infinite water after this expansion becomes

$$e = \frac{(1-r_i)\left[1-r_w \exp(-4\alpha d)\right]}{\left[1-r_i r_w \exp(-4\alpha d)\right]} \left\{ 2 \sum_{n=0}^{\infty} \frac{(-1)^n}{1+\delta_0{}^n} \left[r_i r_w \exp(-4\alpha d)\right]^{n/2} \cos 2n\beta d \right\} . \tag{2-32}$$

The microwave radiometer does not receive a single frequency, but has finite bandwidth passing frequencies in a range which corresponds to a change in the propagation constant of $\pm\Delta\beta/2$. The thickness of the ice is assumed to vary within the antenna footprint as a result of surface roughness. This variation of thickness is assumed to have a uniform distribution about a much greater mean thickness d_o of $\pm\Delta d/2$. The effects of variation in thickness of the ice layer and the finite bandwidth of the radiometer can be incorporated into (2-32) by the convolution of the ideal bandpass function $\Delta\beta$ and the ice thickness variation Δd with (2-32). The average value of the emissivity becomes (Apinis and Peake, 1976):

$$\langle e \rangle = \frac{(1 - r_i)\left[1 - r_w \exp(-4\alpha d_o)\right]}{\left[1 - r_i r_w \exp(-4\alpha d_o)\right]} \left\{ 2 \sum_{n=0}^{\infty} \frac{(-1)^n}{1 + \delta_0{}^n} \right.$$

$$\left. \times \left[r_i r_w \exp(-4\alpha d_o)\right]^{n/2} \left(\frac{\sin n\,\Delta\beta d_o}{n\,\Delta\beta d_o}\right) \left(\frac{\sin n\beta\,\Delta d}{n\beta\,\Delta d}\right) \cos 2n\beta d_o \right\} . \tag{2-33}$$

In developing (2-33) it is assumed that the ice has a low attenuation coefficient such that $\exp(-4\alpha d_o)$ is a slowly varying function and is not involved in the averaging process. The $\sin x/x$ terms essentially suppress the higher order harmonics in the series when the following conditions are satisfied:

$$\Delta\beta d_o \geq \pi \tag{2-34}$$

and

$$\beta\,\Delta d \geq \pi . \tag{2-35}$$

These conditions are usually met in the application of microwave radiometry such that (2-33) reduces to:

$$\langle e \rangle = \frac{(1 - r_i)\left[1 - r_w \exp(-4\alpha d_o)\right]}{\left[1 - r_i r_w \exp(-4\alpha d_o)\right]} \tag{2-36}$$

which is the average emissivity of a thick slightly rough layer of ice.

The emissivity as a function of αd_o for a layer of fresh water ice with an attenuation coefficient of 2 dB/m is shown in Fig. 2-10. The oscillatory behavior has been suppressed primarily by the surface roughness and to some extent by the finite bandwidth of the receiver.

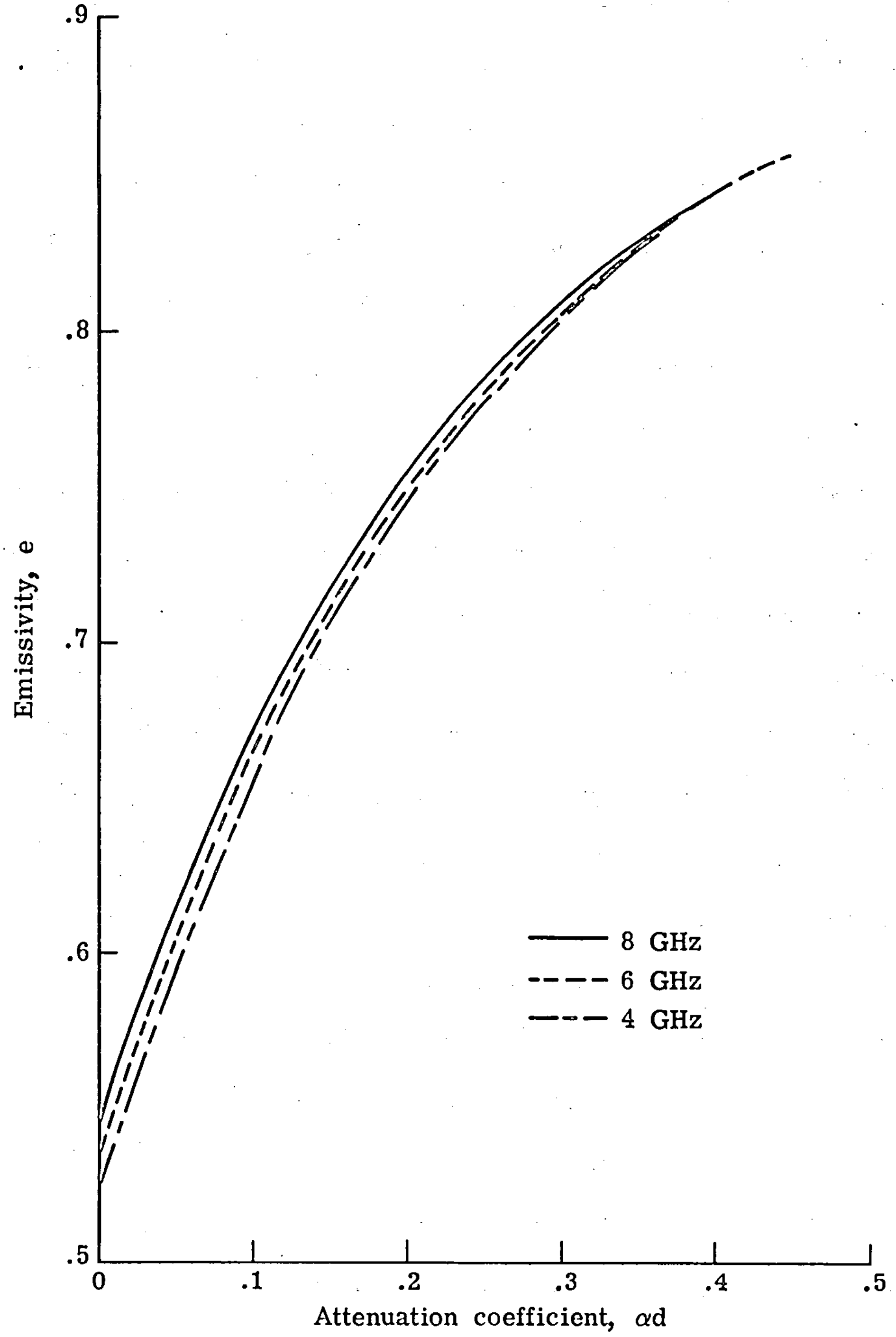

Figure 2-10. Emissivity of rough lake ice over fresh water versus attenuation at a water temperature of 0° C, an ice dielectric constant of 3.2-j0.0066, and for frequencies of 4, 6, and 8 GHz.

The power reflection coefficients r_i and r_w can be determined accurately from (2-25) and (2-26), and thus, the emissivity is a function of the product of the attenuation coefficient and the mean ice thickness. An independent determination of the attenuation coefficient can be made from the thermodynamic temperature of the ice. In principle, the thickness of fresh water ice can therefore be remotely measured using a microwave radiometer to measure the emissivity and an infrared radiometer to infer the thermodynamic temperature.

A microwave radiometer which can accurately measure the brightness temperature to 1 part in 300 and an infrared radiometer with a relative accuracy of 0.25 K should be capable of measuring ice to a thickness of five skin depths. Skin depth as a function of loss tangent for the 4 to 8 GHz frequency region is shown in Fig. 2-11. Loss tangent is defined as the ratio of the imaginary part of the dielectric constant to the real part. The loss tangent for fresh water ice varies from 0.0 to 0.002. Fresh water ice is typically less than 1 m thick, and since five skin depths at 6 GHz for a loss tangent of 0.002 is 22.5 m, the subsurface properties of any fresh water ice can easily be probed.

Sea ice can be divided into two major types, first year ice and multiyear ice. Multiyear ice has survived at least one summers' melt. First year ice exhibits a depth which varies from less than 10 cm for ice called nilas, up to a maximum of 3 m. Multiyear ice is usually thicker than 3 m. The loss tangent of first year ice varies from 0.01 to 0.1 and for multiyear ice, from 0.001 to 0.02 (Vant, 1976). At a

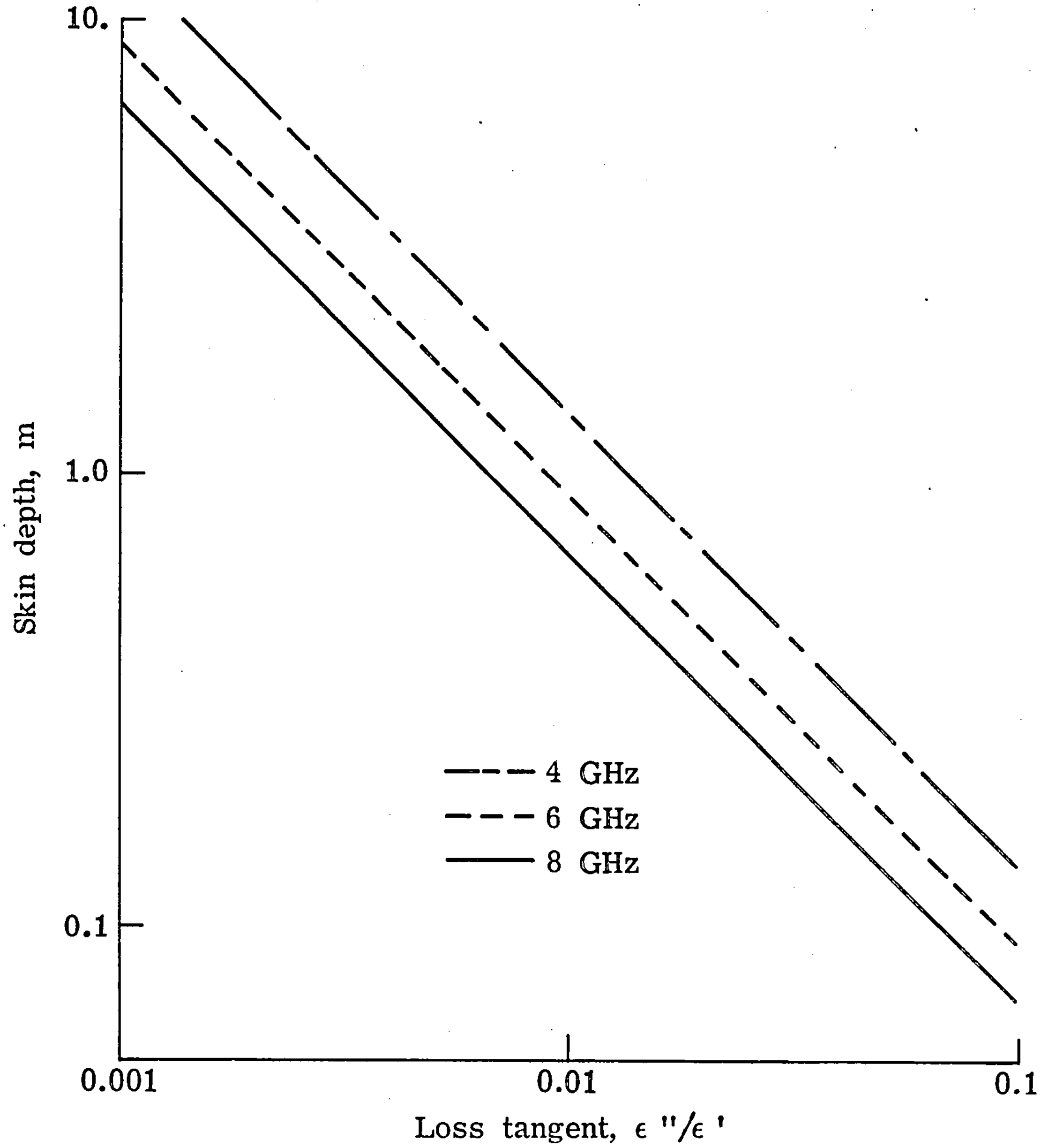

Figure 2-11. Skin depth of a dielectric medium versus the loss tangent at frequencies of 4, 6, and 8 GHz.

frequency of 6 GHz, five skin depths for loss tangents of 0.1 and 0.01 is about 0.5 m and 5 m, respectively. Because the loss tangent of sea ice depends upon several parameters, it appears that radiometric measurements can only establish bounds on the thickness.

CHAPTER III

INSTRUMENT DESIGN AND ANALYSIS

Design Technique

The stepped frequency microwave radiometer (SFMR) is a variable frequency, balanced Dicke switched, noise feedback precision radiometer. The low loss microwave front end of the SFMR is contained within a constant temperature enclosure. The SFMR requires calibration only before and after a mission, some of which extend for periods of several weeks. This is a direct result of the application of noise feedback and the use of a constant temperature enclosure in the design.

The SFMR can operate at any frequency between 4.5 and 7.2 GHz. This provides the ability for radiometric measurements at several frequencies almost simultaneously. The radiometer can operate either in a fixed frequency mode or a frequency stepping mode. The frequency, change in frequency, and time between frequency steps are controlled by a microprocessor based digital controller.

The objective of a radiometer is to measure the amount of received electromagnetic noise power which is captured by the antenna. Noise power is also generated by several sources within the radiometer such as the antenna and microwave front end. These sources include both lossy elements radiating at a thermodynamic temperature and by active circuits within the first few amplifiers of the radiometer. This internally generated noise is statistically independent of the received noise and therefore their noise powers add directly.

The received noise power in a 100 MHz bandwidth for an input antenna temperature of 100 K is 1.38×10^{-13} W. This signal must be amplified by a gain factor of approximately 10^{11} prior to measurement. Exact knowledge of this gain factor is required to determine the input antenna temperature. Short term instabilities in the gain create fluctuations in the radiometer output signal which also add system noise. These gain fluctuations are statistically independent of the radiometer noise, and their noise powers therefore add directly.

There are many types of microwave radiometers (Tuiri, 1964) of which the oldest and simplest is the total power radiometer. The output voltage V_0 of a total power radiometer is:

$$V_0 = kBG_RC_D(T_A + T_R) \tag{3-1}$$

where B is the bandwidth, G_R is the radiometer gain, C_D is the square law detector constant, T_A is the received noise temperature, and T_R is the internally generated radiometer noise temperature.

The total power radiometer has the disadvantage of requiring the measurement of a small noise power T_A which has been added to a much greater noise power T_R. Dicke (1946) developed a design technique in which he modulated the received noise power and thereby provided the capability to distinguish the received noise from internally generated radiometer noise and the noise like gain fluctuations. This modulated radiometer switches the input between the antenna and a known reference noise temperature T_0. The switch driving signal is then correlated with the amplified radiometer noise voltage signal prior to the final output filter. Thus, the output of this radiometer is a function of the difference between T_A and T_O and is

$$V_O = kBG_RC_D(T_O - T_A) . \qquad (3\text{-}2)$$

The output is now independent of the internally generated noise T_R.

The effect of the choice of a switching signal on the overall performance of a modulated radiometer has been analyzed by several investigators (Strom, 1957), (Knight, 1962), and (Wait, 1967). The results from these investigations have shown for a radiometer using a square law detector, the preferred waveform is a square wave. The optimum radiometer performance occurs when the radiometer is switched to the antenna and reference load for equal periods of time (Knight, 1962). The penalty for receiving the antenna noise temperature only one-half the time is that the information on which an estimate of the noise power (variance) is made has been reduced. The resolving capability of the radiometer is reduced by a factor of 2. However, the improvement obtained by elimination of error due to variation in gain and internally generated radiometer noise temperature between calibrations exceeds the loss in resolving capability.

The effect of gain variations between calibrations can be avoided, if in (3-2) T_A can be made equal to T_O by injecting a known amount of noise T_I. A modulated radiometer in which this is accomplished is referred to as a balanced Dicke switched radiometer and (3-2) becomes

$$V_O = kBG_RC_D(T_O - T_A - T_I) = 0 . \qquad (3\text{-}3)$$

Either T_A or T_0 can be varied depending on the relative level of T_A. The SFMR is a balanced Dicke switched radiometer where the noise power T_I is added to the received noise temperature $T_A \leq T_0$ and a closed-loop feedback continuously adjusts T_I such that

$$T_A + T_I = T_0 \tag{3-4}$$

to maintain the null condition specified by (3-3).

The addition of noise to the received antenna noise in a balanced Dicke switched radiometer using a closed-loop feedback was first employed in a radiometer developed for Sun measurements (Ryle and Vonberg, 1948). It has also been used in several other applications requiring precision radiometers (Seling, 1962), (Goggins, 1967), Hardy, et al., 1974), and (Blume, et al., 1977).

The third design technique applied to the SFMR to achieve the required accuracy was to enclose the microwave front end within a constant temperature enclosure. The input section of a microwave radiometer contains devices which have small finite losses which cannot be accurately measured by direct means. Also, these losses do not have the required stability which is the most serious potential problem in precision radiometry. When the received noise temperature T_A is transmitted through such a device with loss α, T_A is attenuated by this loss. As discussed in Chapter II, this loss also emits noise power equal to the loss (absorption coefficient) multiplied by the thermodynamic temperature T. The output of the lossy device is

$$T_A' = (1 - \alpha)T_A + \alpha T . \tag{3-5}$$

The Dicke reference noise temperature T_0 is typically obtained from a resistor which is matched to a transmission line between the resistor and the Dicke switch. From (2-5), the resistor generates a noise power T_0 equal to its thermodynamic temperature T. The Dicke reference load is maintained at a constant thermodynamic temperature T_0 and is included within the constant temperature enclosure. This enclosure contains the microwave front end which is maintained at a constant temperature equal to T_0. Since $T = T_0$, (3-5) becomes

$$T_A' = (1 - \alpha)T_A + \alpha T_0 . \tag{3-6}$$

If a known amount of noise T_I is added to the received noise radiometer before any losses, then (3-6) becomes

$$T_A' = (1 - \alpha)(T_A + T_I) + \alpha T_0 . \tag{3-7}$$

Substitution of (3-4) in (3-7) yields

$$T_A' = (1 - \alpha)T_0 + \alpha T_0 = T_0 . \tag{3-8}$$

The loss α has been eliminated and accurate knowledge of this loss and loss stability problems are avoided. Therefore the combination of the design techniques of a balanced Dicke switched radiometer and a constant temperature enclosure result in a precision radiometer whose accuracy depends only on an accurate knowledge of the added noise, thermodynamic temperature of the constant temperature enclosure, and knowledge of any loss prior to the noise adding point.

This design technique was first used in a fixed frequency precision 2.65 GHz radiometer developed for accurate ocean temperature measurements (Hardy, et al., 1974). The only other application of this design technique is a companion fixed frequency precision 1.4 GHz radiometer, which is used in conjunction with the 2.65 GHz radiometer to measure both ocean salinity and temperature (Blume, et al., 1977). The SFMR is the first and only variable frequency precision microwave radiometer to have used these design techniques and is the most accurate radiometer available for remote sensing at these frequencies.

Design Description

An overall block diagram of the SFMR is presented in Fig. 3-1. There are six major sections which include the antenna subsystem, microwave front end, receiver, analog signal processor, driver circuits, and digital subsystem. The antenna subsystem collects the circular polarized electromagnetic radiation incident on the antenna aperture and feeds it to the microwave front end. At the input of the microwave front end, the injected noise is added to the received noise such that the sum is equal to the reference noise. The Dicke switch alternately switches the radiometer between the sum of the receiver noise and injected noise or to the reference noise. The resultant square wave modulated noise signal, which is in the microwave frequency region, is amplified prior to transmission to the receiver.

The receiver down converts the noise signal from the microwave frequency region to a filtered baseband signal near zero frequency. This

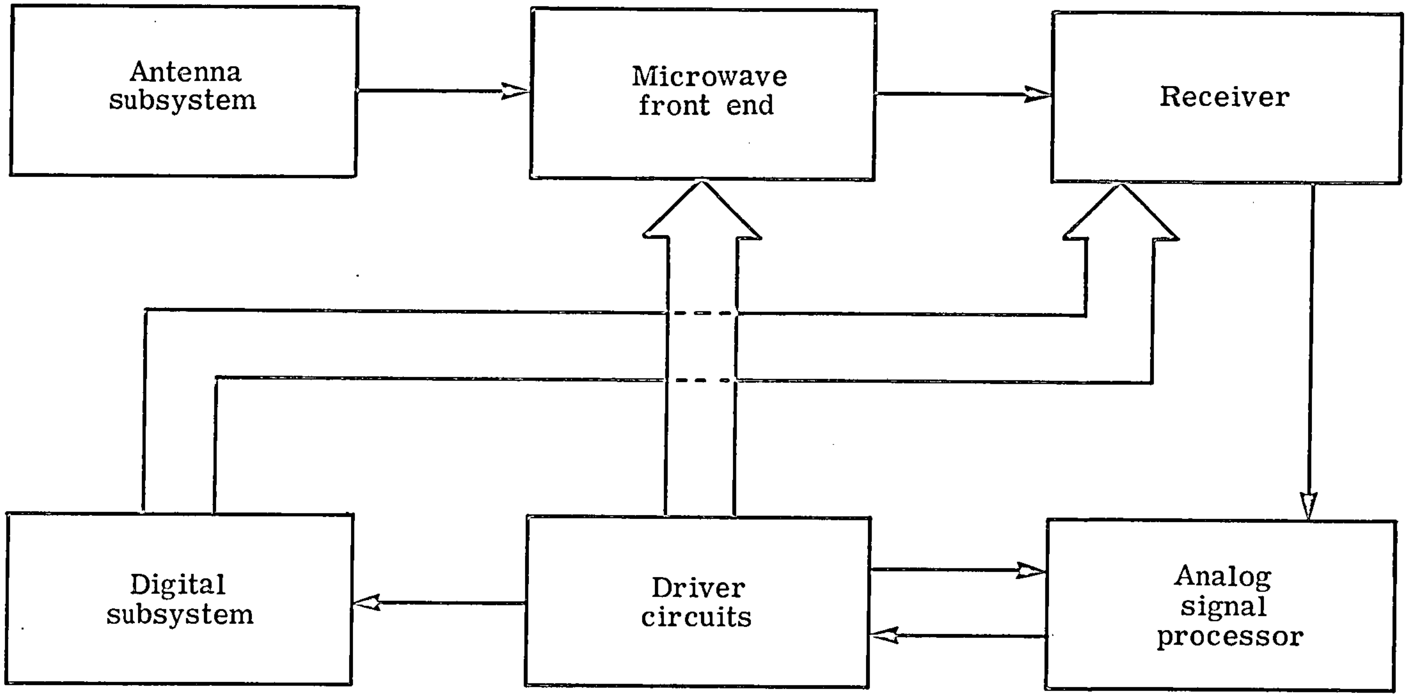

Figure 3-1. Block diagram of the stepped frequency microwave radiometer.

baseband signal is detected, amplified, and correlated with the Dicke switching signal. It is then integrated to obtain a dc voltage whose amplitude is a measure of the noise power of the received antenna noise temperature. These functions are accomplished in the analog signal processor. The dc voltage is converted to a variable duty cycle pulse which turns on the injected noise modulator. The variable duty cycle pulse also controls a counter in the digital subsystem which represents a digital measure of the receiver antenna noise temperature. The voltage to pulse frequency converter is included in the driver circuits section along with the constant current noise diode driver and the square wave oscillator which provides the Dicke switching frequency. The microprocessor based digital subsystem performs the functions of SFMR control, data handling, thermodynamic temperature measurement, and timing.

A photograph of the SFMR is shown in Fig. 3-2 as configured for installation in the NASA CV-990. The antenna is partially visible inside the mounting frame. The microwave front end is located inside the constant temperature enclosure above the radiometer. The receiver is located in the box located on the left side of the frame, while the analog signal processor and driver circuits are located in the other box. The digital subsystem is contained in an airborne equipment rack located behind the SFMR. The operation and design of each of the six major sections are subsequently discussed.

The antenna subsystem is shown in Fig. 3-3 and consists of a radome, polarizer, and corrugated horn. This subsystem is connected to

Figure 3-2. Stepped frequency microwave radiometer configured for installation in NASA CV-990 aircraft.

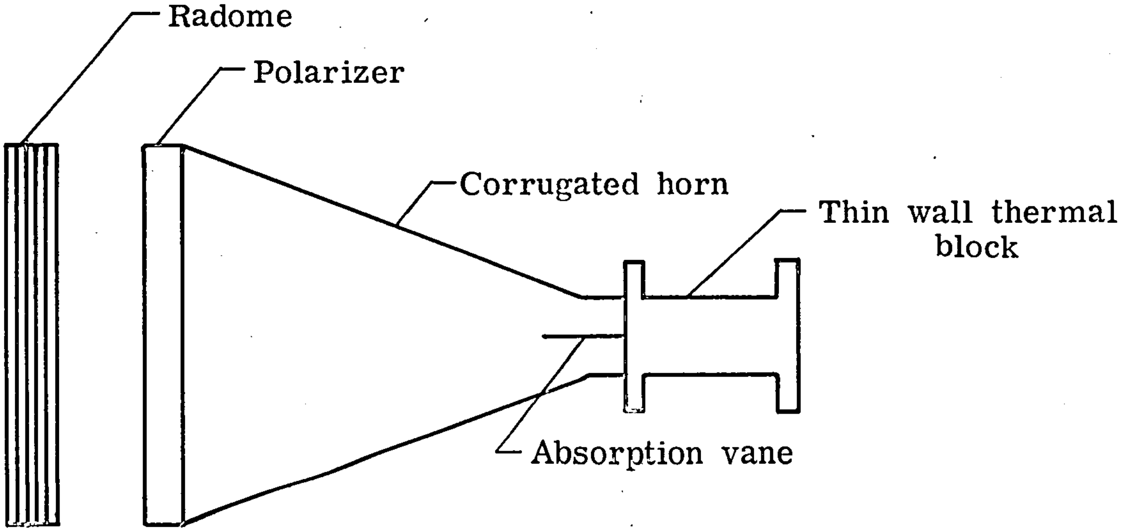

Figure 3-3. Diagram of the antenna subsystem.

a waveguide to coaxial adapter in the constant temperature enclosure. This transition serves as a thermal block which is necessary to reduce the heat loss from the constant temperature enclosure. The radiometer generates noise within the microwave front end which it radiates through the antenna toward the polarizer. An absorption vane, located in the antenna throat section, is constructed of resistive material and absorbs the electric field which is oriented in the same plane as the vane. The undesired reflected noise from the radiometer is orthogonal to the desired received antenna noise and is consequently absorbed by the vane. The vane is visible in the photograph, Fig. 3-4, of the antenna where the radome and polarizer have been removed.

The antenna is a corrugated horn which is particularly well suited for radiometer applications, because such an antenna exhibits low side and back lobes, good symmetry between principal plane patterns, and broadband frequency capability. Beam efficiency, which is extremely important in accurate radiometric measurements, can be obtained with a corrugated horn over a 1.6 to 1 frequency range. These are the primary reasons why this antenna type was chosen for the SFMR.

The design of the SFMR employs 47 triangular teeth with V-shaped corrugations (Mentzer, et al., 1975) and is based on data from the Antenna Laboratory at Langley Research Center. The horn was constructed by Rockwell International (Love, et al., 1975). The exact number of teeth was determined experimentally to obtain the lowest VSWR over the operating frequency region.

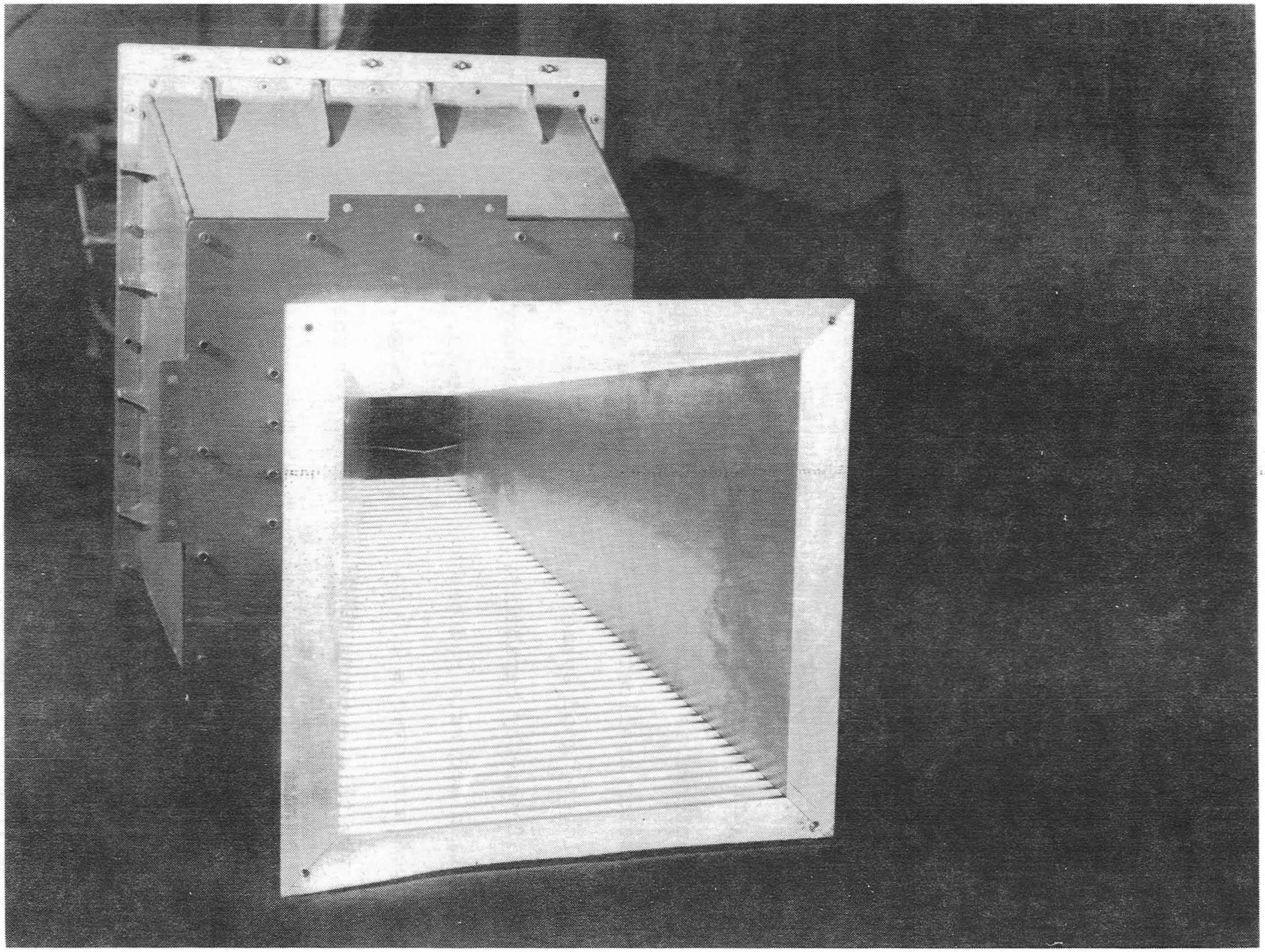

Figure 3-4. Corrugated horn antenna without radome and polarizer.

The antenna has a square aperture which is 24.2 cm square, thereby providing a 3 dB beamwidth of approximately 20° at the lowest operating frequency. The horn tapers to a square 4.06 cm waveguide which provides a cut-off frequency of 3.7 GHz for the dominant modes and 7.35 GHz for the next higher order modes. The antenna has a length of 48.4 cm and a flare angle of 11°52'.

Principal plane antenna patterns at 6 GHz for the SFMR antenna with the radome and polarizer installed are shown in Fig. 3-5. A complete set of patterns have been measured from 4.5 to 7.2 GHz for both horizontal and vertical principal planes. The half power beamwidth at 6 GHz is 15° and varies from 18° at 4.5 GHz to 13° at 7.2 GHz. The effect of these finite antenna beamwidths and pattern shape on the measurement accuracy is accounted for through the antenna pattern correction factor. This is discussed in Chapter IV.

The meander line polarizer transforms the received electromagnetic radiation from circular polarization to the proper linear polarization for reception by the linearly polarized corrugated horn antenna. The meander line polarizer was conceived at the Stanford Research Institute in 1966 (Young, et al., 1973). This transmission line exhibits low loss, octave frequency bandwidths, and low VSWR. The polarizer consists of a layered structure of four copper clad dielectric sheets from which an array of meander line slow wave structures has been etched. Between the copper clad sheets are three thick low loss polyfoam sheets which provide the required spacing between the meander line sheets. The

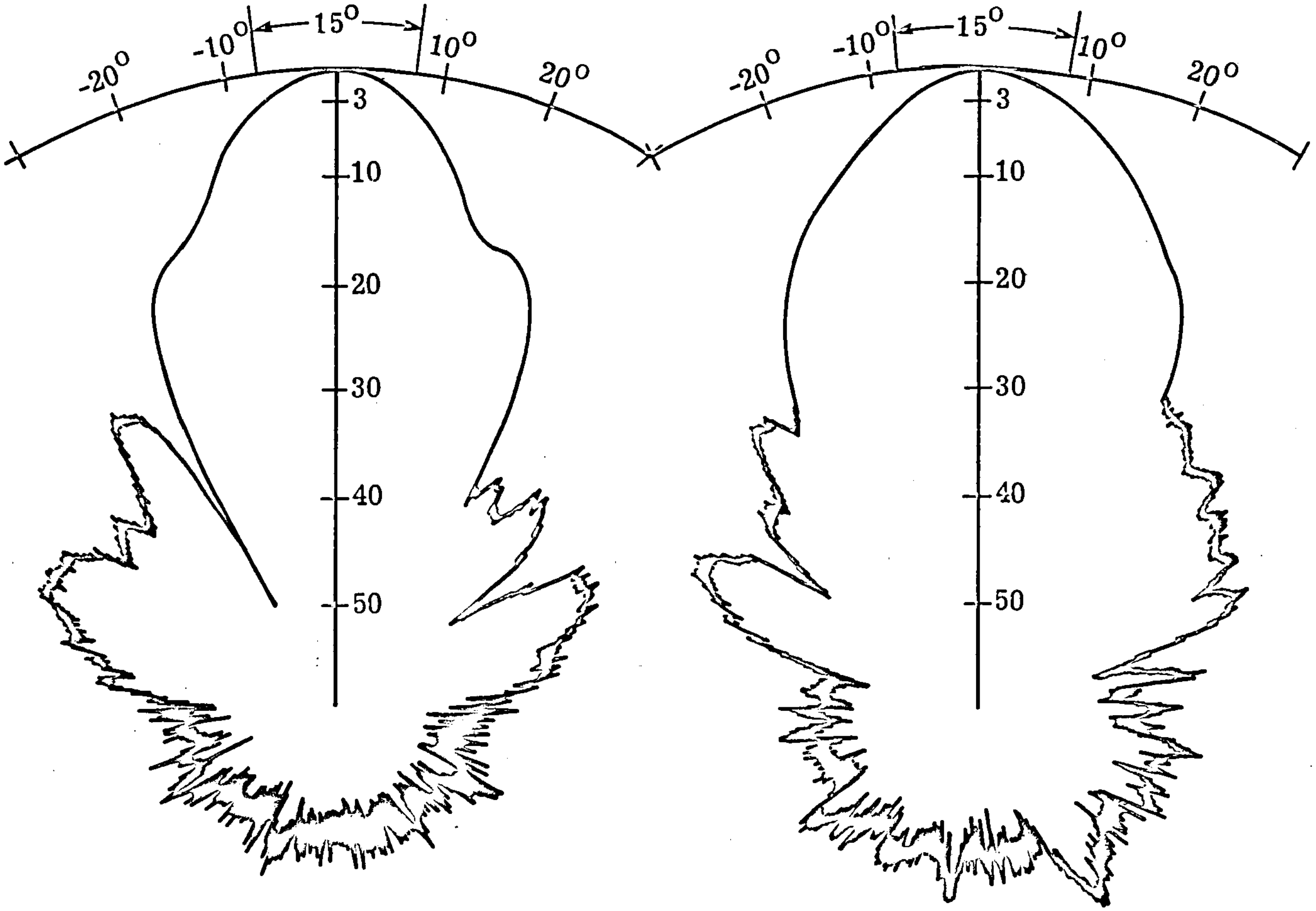

Vertical **Horizontal**

Figure 3-5. Principal plane antenna patterns of the stepped frequency microwave radiometer antenna including radome and polarizer at a frequency of 6 GHz.

SFMR polarizer was built by Hacking Labs, Inc. and has an attenuation coefficient of approximately 0.2 dB (0.035) and a power reflection coefficient of 0.01.

The radome is a broadband eleven layer design. It consists of six layers of fiberglass, the outer two being 0.0762 cm thick and the four remaining inner layers 0.0381 cm thick. The radome provides the pressure seal between the aircraft interior and exterior. The outer two layers are thicker because of high altitude pressure requirements for installation on the NASA CV-990. The spacing between the six fiberglass layers consists of an open cell honeycomb material 0.3175 cm thick. The radome was designed by W. F. Croswell of the Electromagnetic Research Branch, Langley Research Center, and was fabricated in the Model Shop at Langley Research Center.

The electrical performance of the radome over the frequency range from 4.5 to 7.2 GHz was calculated using a computer program which determines the absorption α and power reflection coefficient r for a multiple layer dielectric structure. The results of this analysis are presented in Fig. 3-6. The absorption is reasonably constant over the required frequency range. The reflection coefficient is very low at 5 GHz, however, it increases to nearly 10 percent at 7.2 GHz. The absorption and reflection are incorporated into the inversion algorithm developed in Chapter IV.

The microwave front end is contained within a RFI shielded housing located inside a thermally insulated constant temperature enclosure. It includes the injected noise circuit, the Dicke switch, and the low noise

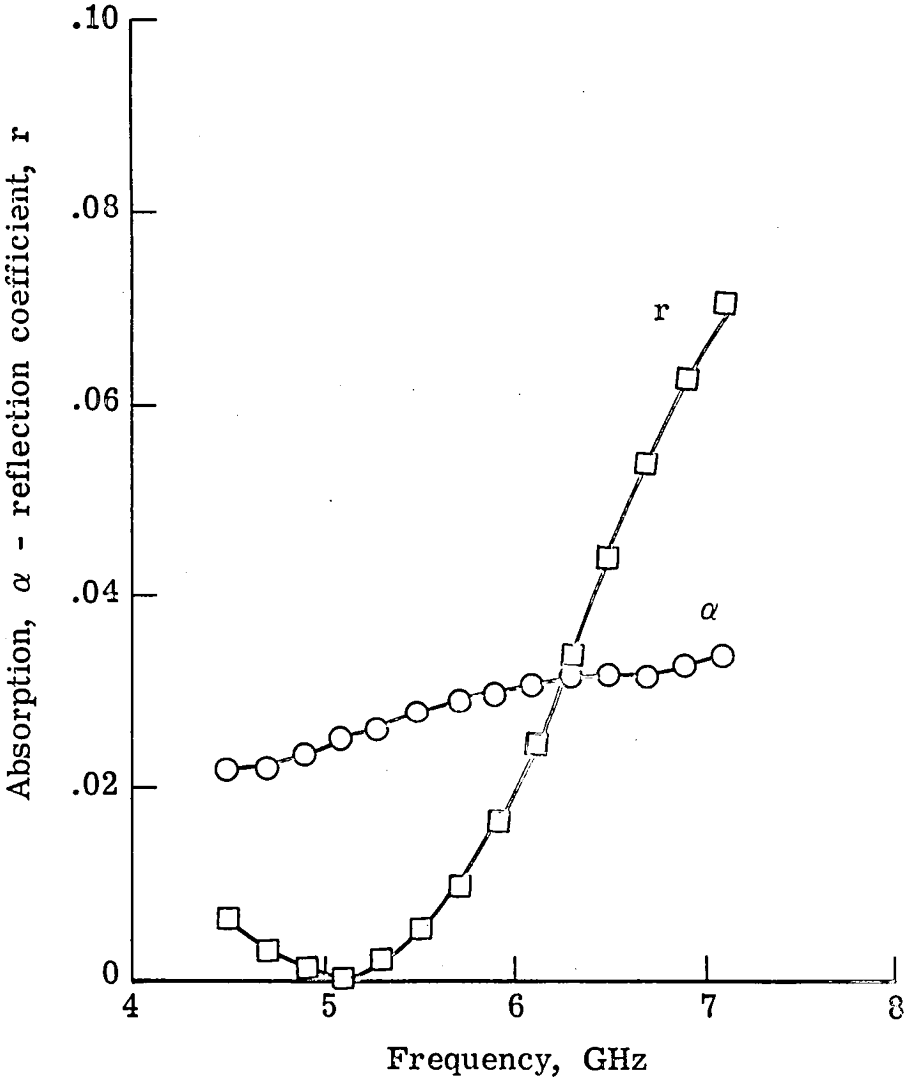

Figure 3-6. Absorption and reflection coefficients of the radome versus frequency.

amplifier. Also, precision thermodynamic temperature measurements of the Dicke reference load, the constant temperature plate, and the waveguide to coaxial adapter are accomplished by using precision thermistors calibrated to an accuracy of 0.1 K. Heaters within the enclosure are operated through a proportional controller and maintain the desired temperature to within ±0.1 K. A block diagram of the microwave front end is shown in Fig. 3-7.

The injected noise circuit consists of the avalanche noise diode, isolator, noise modulator, attenuator pad, and a noise coupler. The noise diode generates a constant noise power which is modulated by the noise modulator using variable duty cycle 70 μs wide pulses. These noise pulses are added to the received noise through a coupler. The attenuator pad sets the amplitude of the noise pulses such that a 0.70 duty cycle is required when the input antenna noise temperature is near 0 K. The isolator provides a constant input impedance to the noise diode while the noise modulator switches. The noise diode is driven by a constant current source for stability. The noise output has an excess noise temperature above 290 K of 31.0 ± 0.2 dB (365,000 ± 17,000 K) over the operating frequency range. The noise output is stable to better than 0.001 dB.

The noise modulator is a single pole single throw PIN diode switch (Watson, 1969). It consists of three shunt diodes which are biased on by a dc current of 75 mA. The switch provides an isolation >63 dB when the bias is applied. Output noise is transmitted from the noise diode to the noise coupler when the bias is removed. The switch insertion

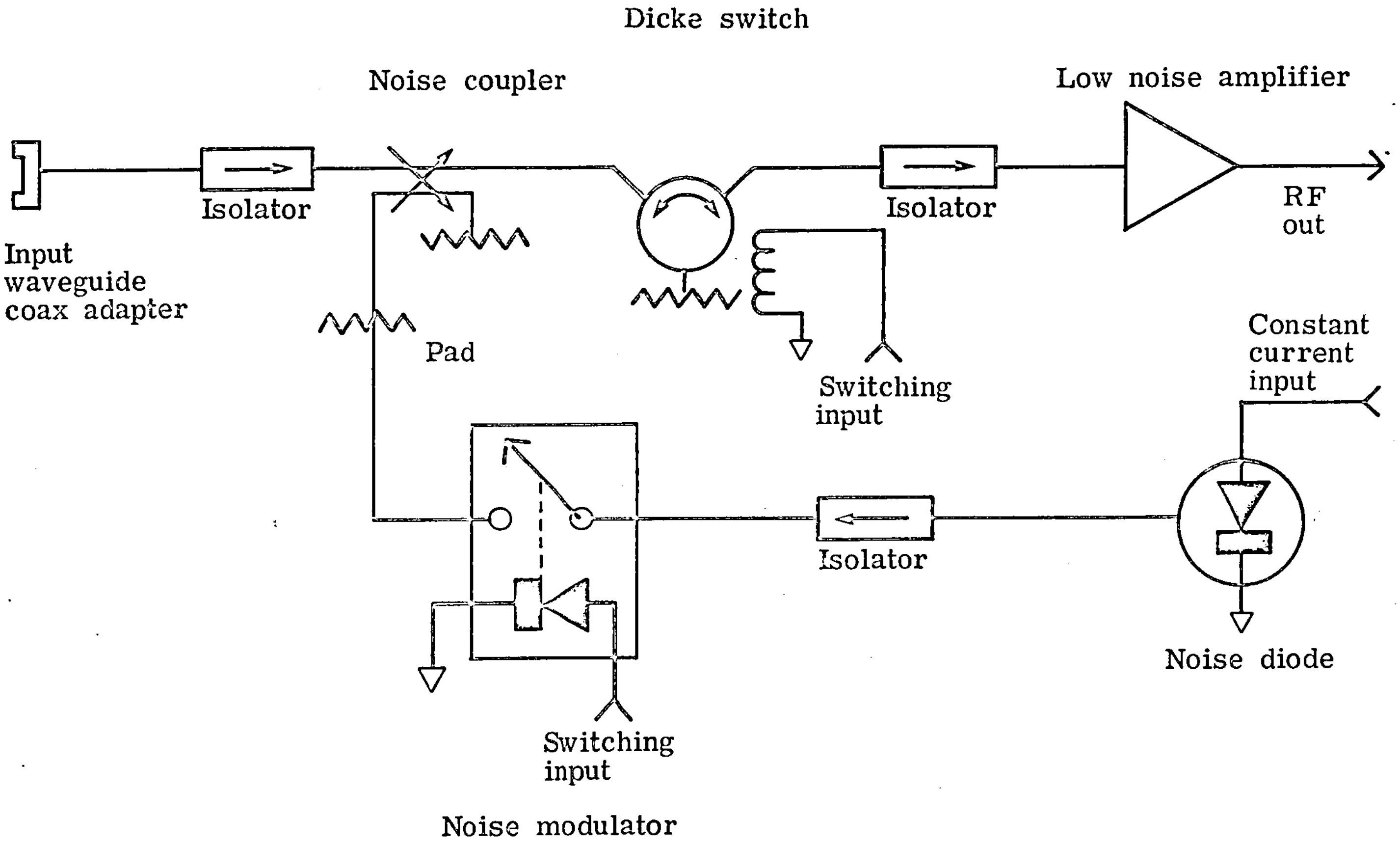

Figure 3-7. Block diagram of the microwave front end of the radiometer contained in the constant temperature enclosure.

loss is <1.6 dB. The noise coupler is a directional coupler with a coupling of 20 dB, a directivity of 20 dB, and a maximum insertion loss of 0.25 dB.

The Dicke switch is a broadband latching Y junction circulator which operates over the frequency region from 4.5 to 7.2 GHz. The circulator is a three port ferromagnetic device in which the direction of the magnetic field determines which input is connected to the output. The circulator can be switched by the momentary application of a current pulse which drives the magnetic field into saturation. Upon removal of the current pulse, the magnetic field follows the hysteresis loop and reaches the residual value. Two switching coils are used to drive the magnetic field into saturation in either a positive or negative direction, thereby switching the inputs. The latching circulator has an insertion loss <0.6 dB and an isolation >18 dB.

The low noise amplifier is a broadband tunnel diode amplifier with a gain of 26 ± 1 dB and a noise temperature of 600 ± 50 K over the operating frequency range. The low noise amplifier is included in the constant temperature enclosure since any loss prior to the first amplification stage must be maintained at the Dicke reference temperature for accurate radiometer operation. The output of the low noise amplifier feeds a coaxial feedthrough in the RFI shielded housing. A coaxial transmission line connects the output to the receiver input.

Views of the microwave front end in the RFI shielded housing are shown in Figs. 3-8 and 3-9. The waveguide to coaxial adapter which connects to the antenna subsystem can be seen in Fig. 3-8. The RFI

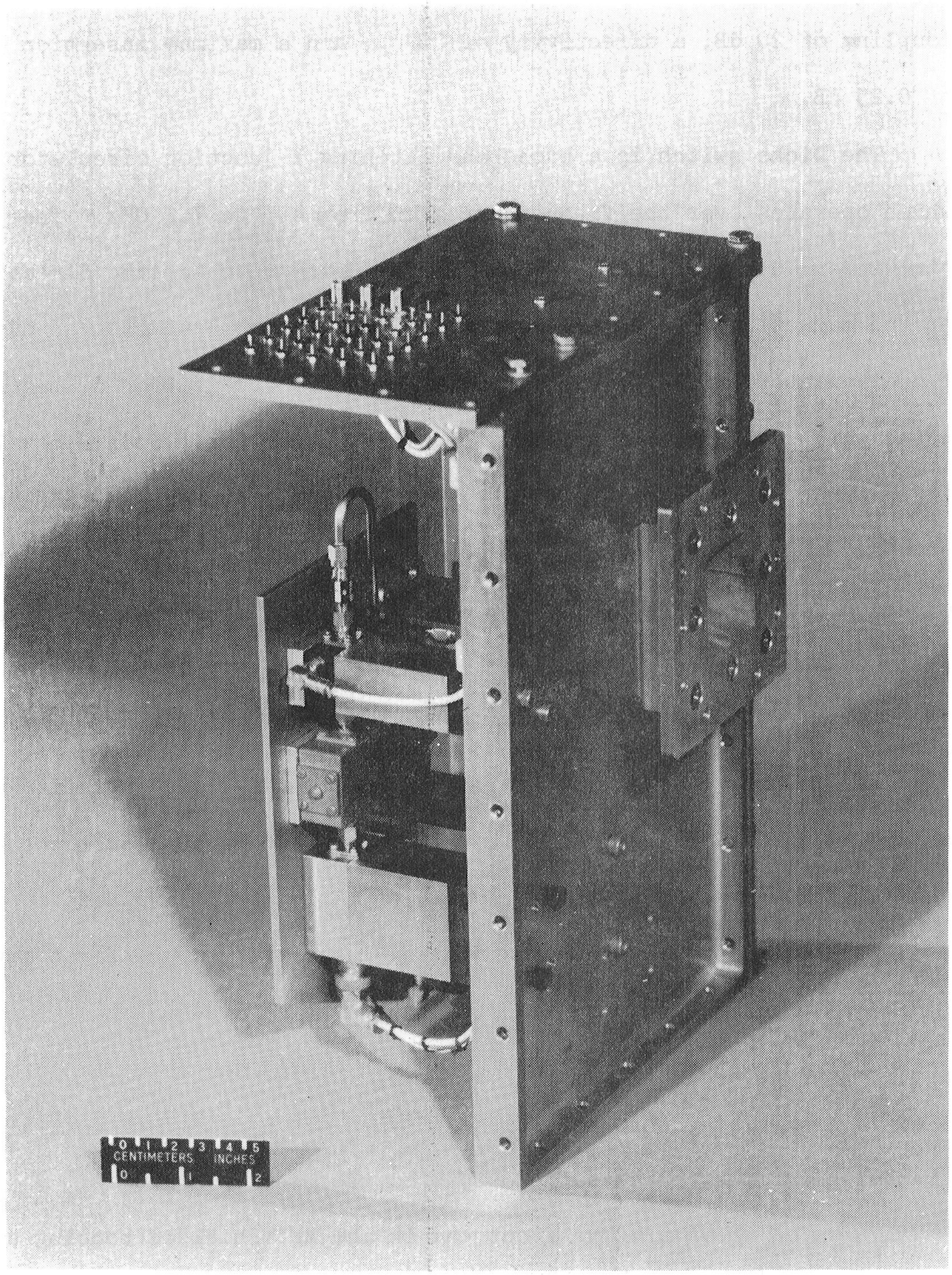

Figure 3-8. View of the microwave front end showing the antenna feed and noise injection circuit components.

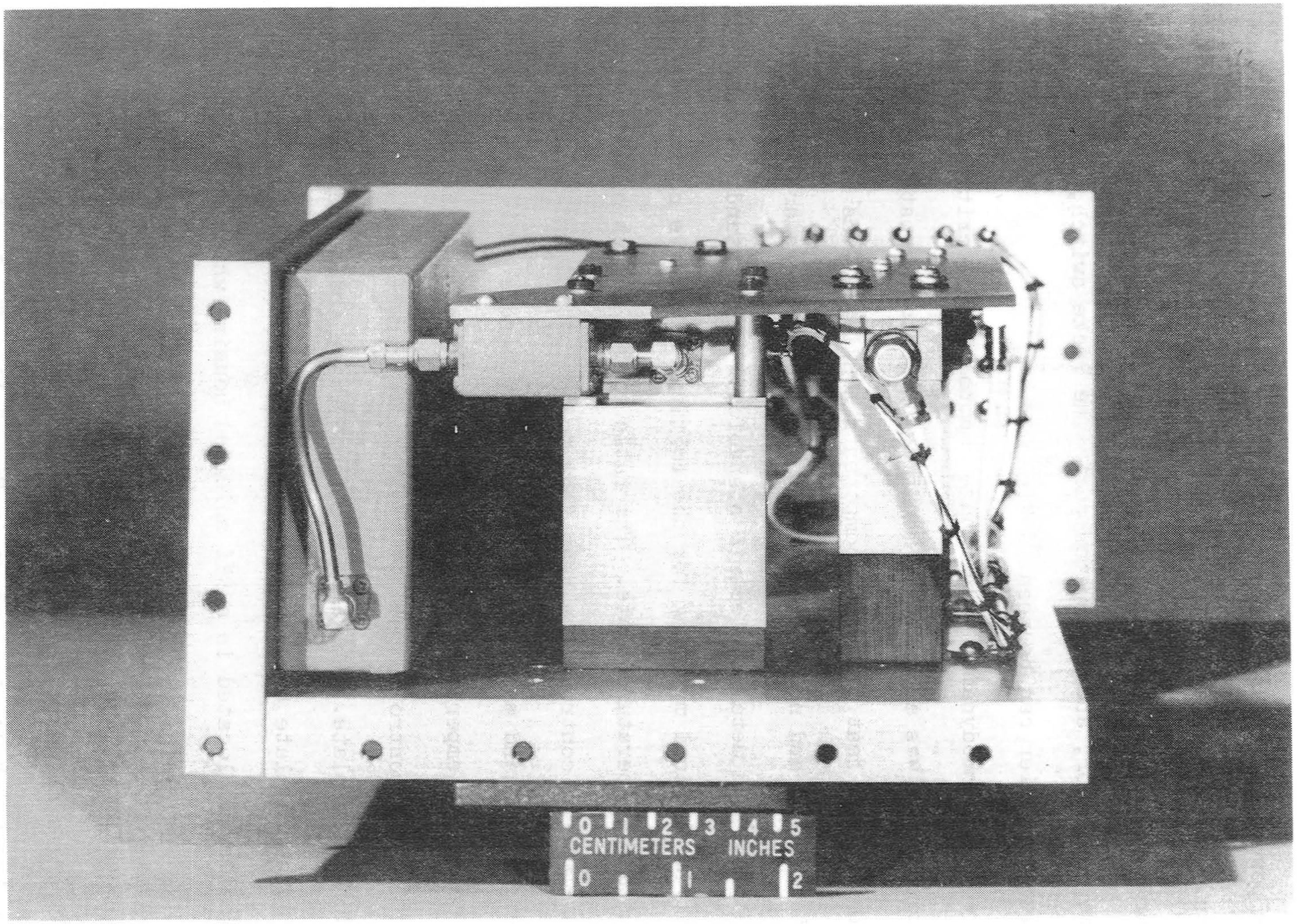

Figure 3-9. View of the microwave radiometer front end showing the temperature stabilizing plate, thermal control paths, tunnel diode amplifier, and Dicke circulator switch.

feedthroughs are used to provide connections through the shielded housing for power, control signals, heater power, and temperature measurements. The noise injection circuit is visible beneath the constant temperature plate. From left to right is the noise source, isolator, noise modulator, and attenuator pad. The Dicke switch, isolator, and low noise amplifier can be seen in Fig. 3-9.

The precise thermodynamic temperature control of the critical microwave components was achieved by mounting these to a constant temperature plate. The heat producing components consist of the Dicke switch, noise diode, and noise modulator. These components are mounted between the plate and metal/dielectric standoffs. These standoffs provide the only mechanical mounting for the critical microwave components and the constant temperature plate. The ratio of the length of metal to length of dielectric controls the heat flow to the outside walls of the RFI shielded housing and maintains a uniform temperature distribution across the constant temperature plate. The heaters and the thermistor used to provide the control signal to the heater proportional controller are mounted on this plate. The absolute temperature and temperature gradient across the plate are controlled to <0.1 K.

The receiver is located in a RFI shielded housing which is mounted to the side of the radiometer frame. It contains the mixer, preamplifier, local oscillator, and three predetection filters. A block diagram of the receiver is shown in Fig. 3-10. A photograph of the receiver removed from the RFI housing is shown in Fig. 3-11. The local oscillator, mixer, and preamplifier are located on the left while the

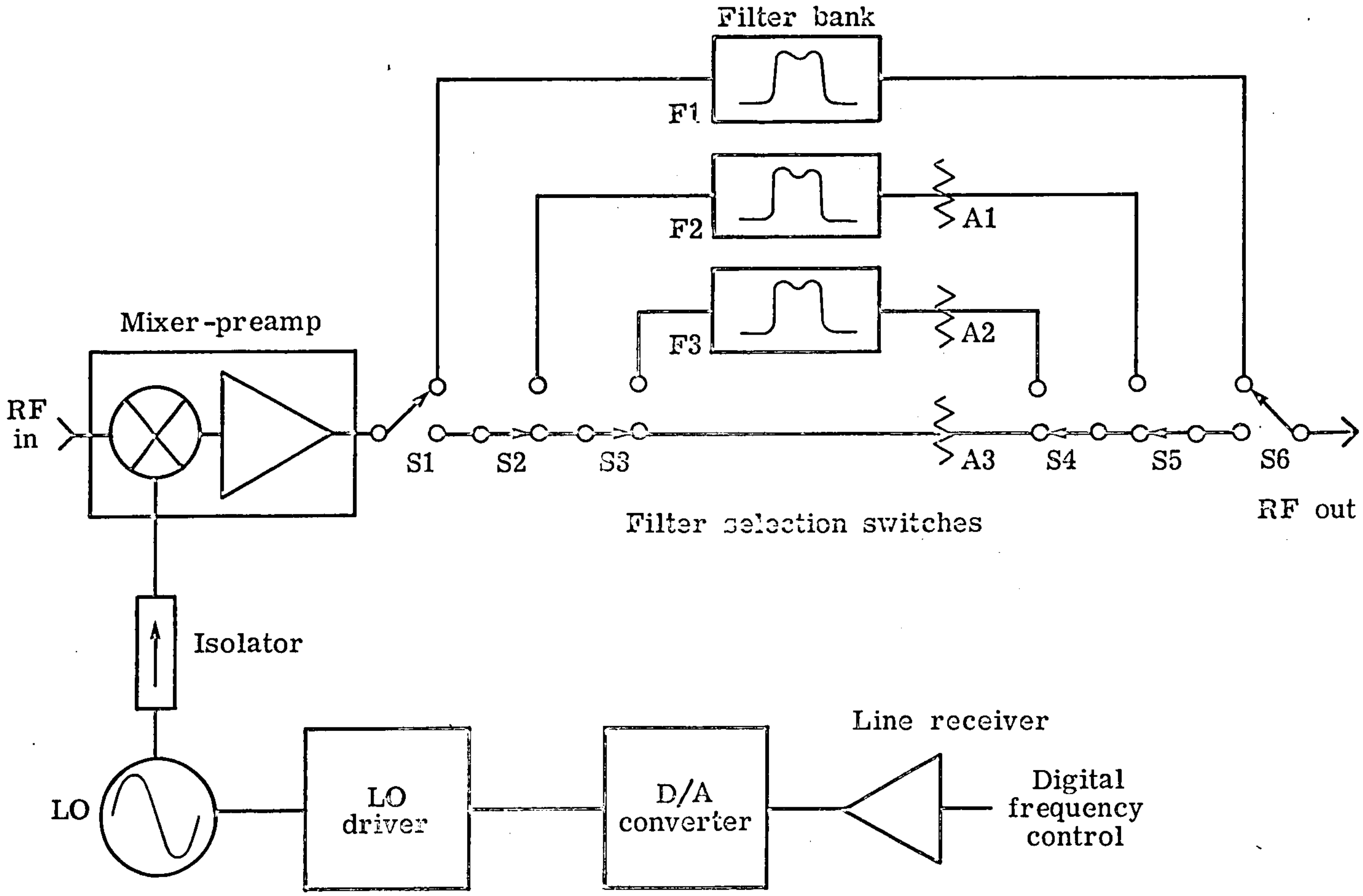

Figure 3-10. Block diagram of the receiver portion of the stepped frequency microwave radiometer.

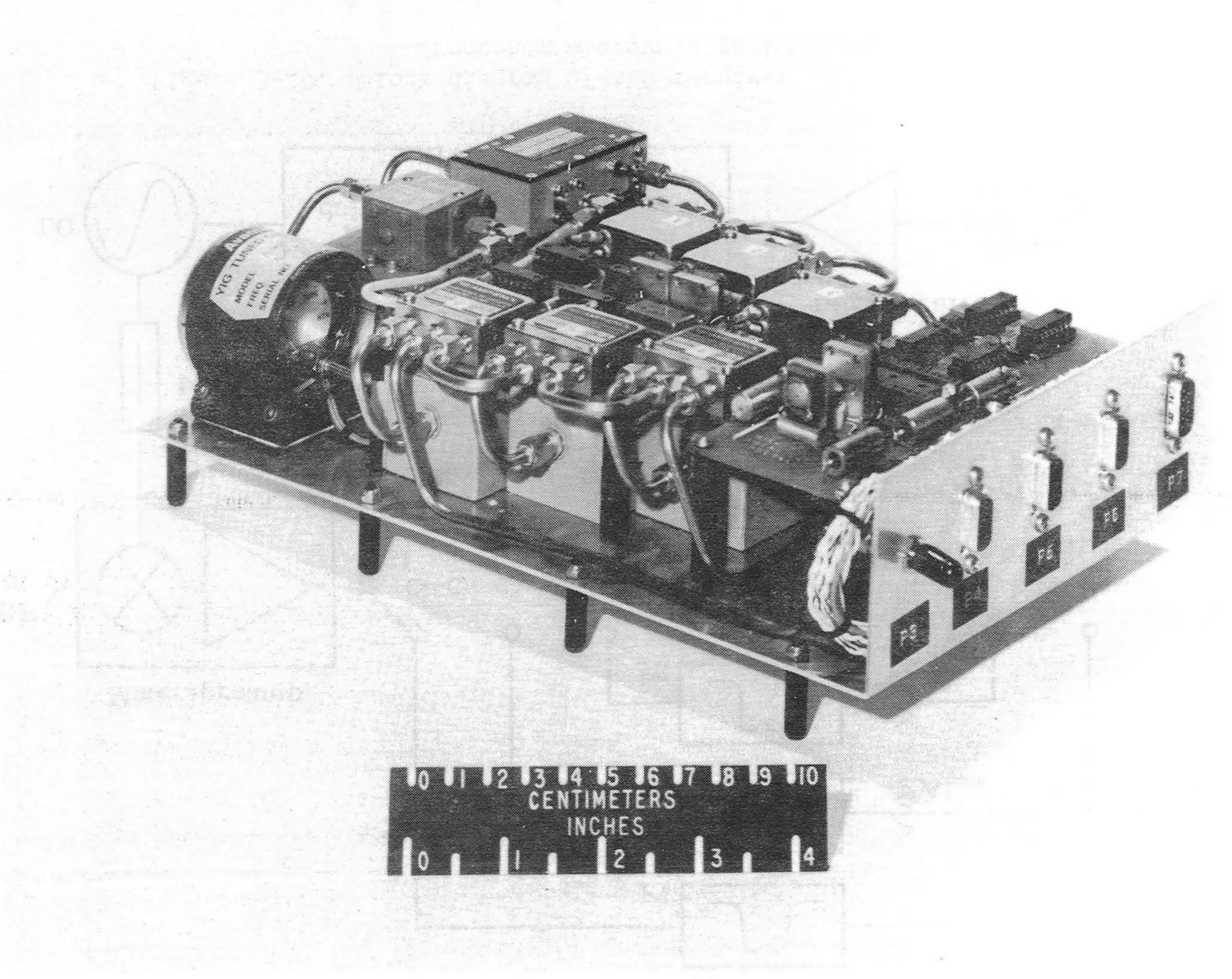

Figure 3-11. View of the receiver showing the local oscillator, mixer-preamplifier, and predetection filters.

predetection filters are mounted below the filter selection switch relays.

The double balanced mixer uses microwave integrated circuits and has an input frequency range from 4 to 8 GHz. The local oscillator provides a 4 to 8 GHz 10 mW signal which is mixed with the microwave input signal to produce a baseband signal containing frequency components from 10 to 1000 MHz. This baseband signal contains both the upper and lower sidebands from the mixing process. The noise figure of the mixer is 8.0 ± 0.3 dB over the frequency range. The overall power gain from the microwave input to the output of the preamplifier is 41 dB.

The local oscillator is a Yttrium Iron Garnet (YIG) tuned microwave transistor oscillator, whose frequency is controlled by a 0 to 10 V signal from the local oscillator (LO) driver. This dc voltage is obtained from a digital to analog (D/A) converter and provides an 8 bit frequency selection digital word to the D/A converter. This word can specify 256 distinct frequencies spaced every 16 MHz between 4 and 8 GHz. Since the minimum bandwidth after combining the upper and lower sidebands is 20 MHz, continuous frequency coverage is achieved.

The capability to measure small changes in the noise temperature is a function of the predetection bandwidth, hence as the bandwidth becomes wider a smaller change in noise temperature can be measured. However, as the bandwidth becomes wider the susceptibility to interference from undesired electromagnetic radiations becomes greater. Therefore, the bandwidth should be as narrow as possible and still satisfy the measurement requirements. The bandwidth is controlled by either switching in one of three filters or using the full bandwidth capability of the mixer preamplifier. The digital subsystem supplies a bandwidth selection digital word which changes switches S1 and S6 to select filter F1, S2 and S5 to select filter F2, or S3 and S4 to select filter F3. Filter F1 is a 10 MHz low pass filter, F2 is a 50 MHz low pass filter, and F3 is a 250 MHz low pass filter.

The amount of noise power transmitted to the square law detector in the analog signal processor should be constant to maintain the same operating point on the square law detector transfer function. Since the noise power is a function of the predetection filter bandwidth, attenuators A1, A2, and A3 were added to the outputs of F2, F3, and the unfiltered path. The attenuation is set so that the output noise power from the receiver is constant within ±2 dB irrespective of the bandwidth selected.

A schematic of the analog signal processor is shown in Fig. 3-12. After square law detection of the filtered baseband signal from the receiver, the detected signal is amplified by a variable gain bandpass amplifier and then correlated with the Dicke switching frequency. The output signal from the correlator is integrated and amplified. The resulting 0 to 10 V signal is a measure of the received antenna noise temperature.

The input to the square law detector is transformer coupled to prevent ground loop noise in the radiometer. The square law detector employs a hot carrier diode which has a silicon Schottky barrier junction. It is biased at an optimum operating point on the transfer curve

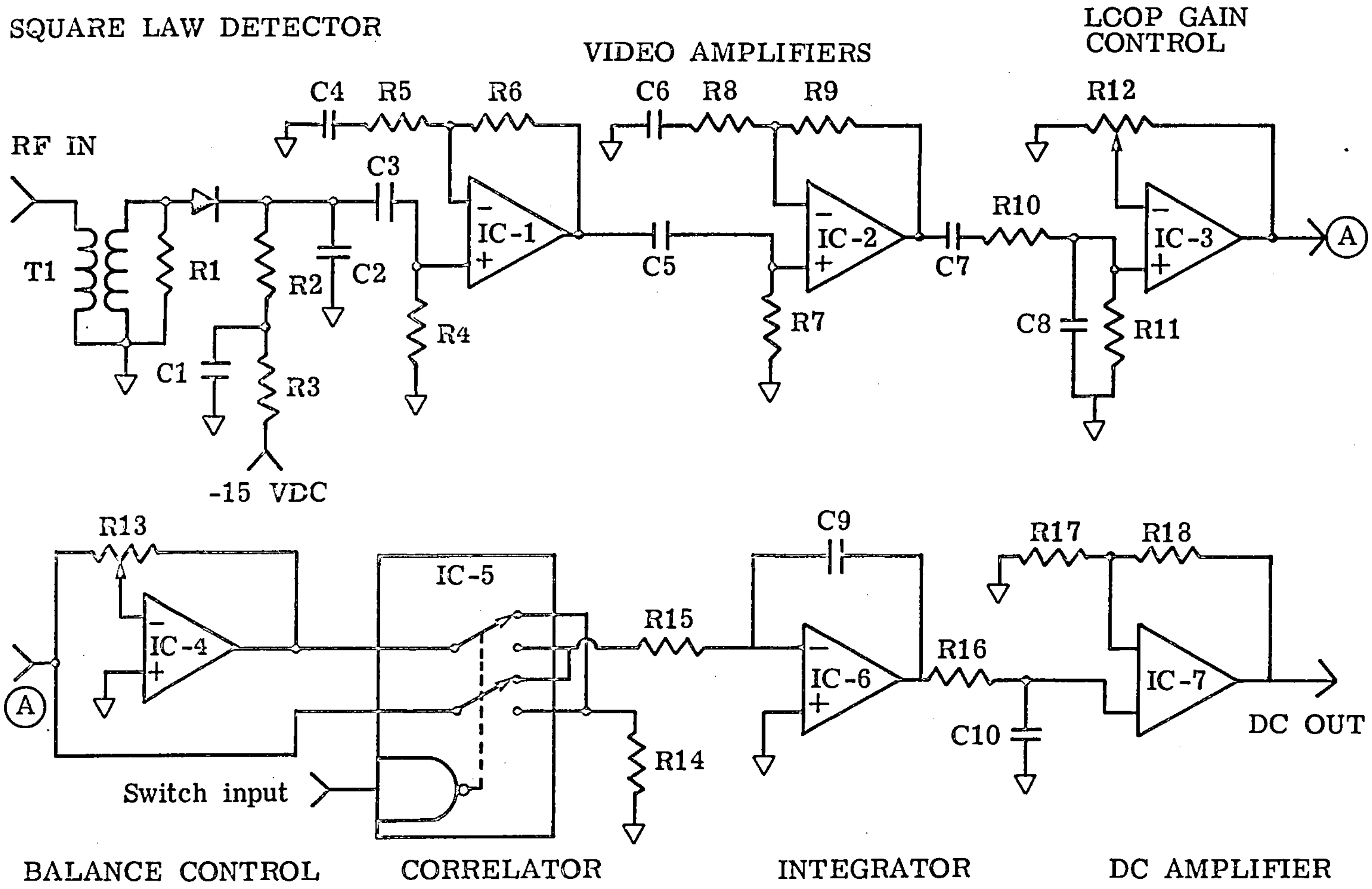

Figure 3-12. Block diagram of the analog signal processor.

by a network consisting of R2, R3, and C1. The output dc voltage is then a linear function of the input power. The corresponding gain constant is approximately 400 V/W. Higher frequency components of the detected output voltage are removed by capacitor C2.

The measure of the received antenna noise temperature is now represented by the fundamental and harmonic components of the Dicke modulated output voltage. These must be amplified in a bandpass video amplifier to a sufficient level prior to the correlation process. IC-1 and IC-2 form a high pass video amplifier with a break frequency near 2 Hz and a voltage gain of approximately 60 dB. Component IC-3 is a bandpass video amplifier with a variable voltage gain ranging from 0 dB to 26 dB in order to control the radiometer loop gain, and to provide a bandpass from 0.3 Hz to 5.6 kHz.

The correlator consists of IC-4 and IC-5. The amplifier IC-4 provides a signal to the metal oxide semiconductor (MOS) analog switch which is exactly equal, but of the opposite polarity, to the output of the video amplifier. The correlator switches the input to the integrator synchronous to the Dicke circulator switch. During one-half of the Dicke cycle the sum signal of the received antenna noise and the injected noise is the input signal to the integrator. During the other half of the Dicke cycle, the Dicke reference noise is the input signal to the integrator, but with the opposite polarity. When the system is balanced, i.e., the received noise plus the injected noise equals the Dicke reference noise, the net input to the integrator is zero and the dc output voltage remains constant. If an unbalance exists, the error either increases or decreases the dc output voltage. This change increases or decreases the injected noise by varying the duty cycle of the injected noise pulses until the balanced condition is again satisfied.

The dc amplifier following the integrator is a simple lag network which amplifies the dc output voltage from the integrator to the 0 to 10 V range required by the voltage to frequency converter in the driver circuit. The optimum performance of the second order control loop used in the SFMR has been determined (Stanley, 1979) to occur when the product of the noise bandwidth and settling time is a minimum. This is accomplished by a simple lag network placed after the integrator such that the second order loop is critically damped.

The driver circuit schematics are shown in Fig. 3-13. These include the voltage to frequency converter, noise modulator driver, output line driver to the digital subsystem, Dicke switching signal square wave oscillator, and the constant current source for the noise diode. The square wave oscillator is a straightforward circuit design which consists of IC-6, IC-7, and IC-8. It provides a 124 Hz square wave to the Dicke switch driver and the correlator located in the analog signal processor. The Dicke switch driver is located outside the constant temperature enclosure since it is required to be physically close to the latching circulator. The driver differentiates the square wave, producing a current pulse at each transition. These current pulses switch the direction of the magnetic fields in the circulator switch as discussed previously.

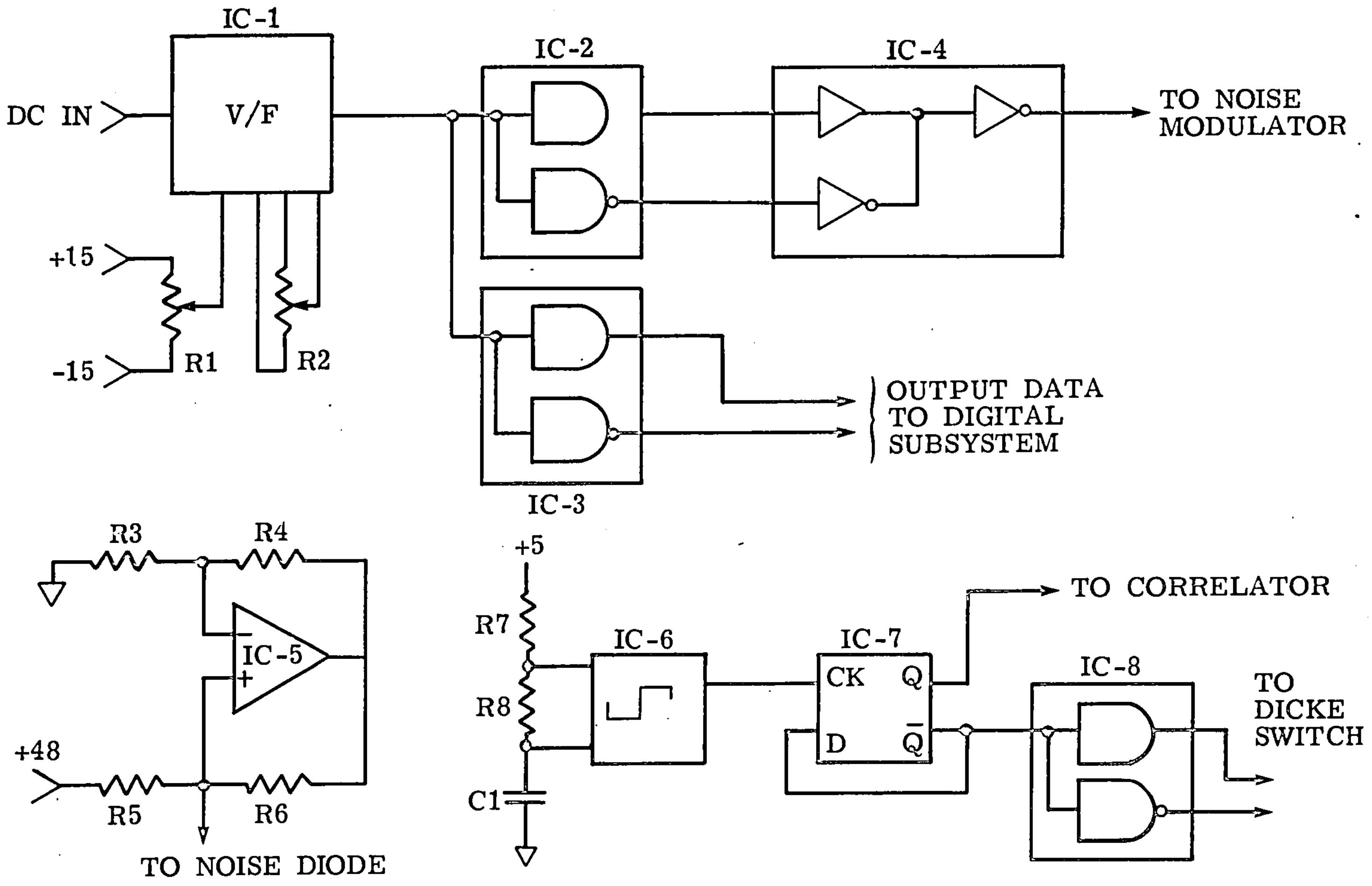

Figure 3-13. Block diagram of the driver circuits.

The dc voltage from the analog signal processor is converted to a variable duty cycle 70 μs pulse train in the voltage to frequency converter. The number of pulses ranges from zero at 0 V to 10,000 at 10 V. Resistors R1 and R2 adjust the zero point and slope of this transfer curve. IC-2 and IC-4 provide a dc bias current of 75 mA to the PIN diodes in the noise modulator when the variable duty cycle pulse is zero. The pulse turns off the dc bias current to the PIN diodes and the noise from the avalanche noise diode is added to the received noise through the noise coupler in the microwave front end. IC-3 is a line driver which transmits the variable duty cycle 70 μs pulses to the digital subsystem. These pulses are a measure of the received noise temperature and are the radiometer output data to the digital subsystem.

The remaining circuit IC-5 is a constant current source which provides current to the noise diode in the microwave front end. The circuit is a Howland circuit (Smith, 1971) and provides a constant current equal to the input voltage (+48) divided by the value of resistor R5. The stability of the current is determined by the stability of the input voltage and the resistor R5.

Figure 3-14 presents a view of the RFI shielded housing which contains the analog signal processor (left) and driver circuits (right) in separate compartments. The use of separate compartments shields the low level analog signals from the high level digital signals. There are only two connections between the two compartments, namely the output dc voltage and the Dicke switching signal, both of which employ RFI feedthroughs. Outputs are provided from the analog signal processor for the

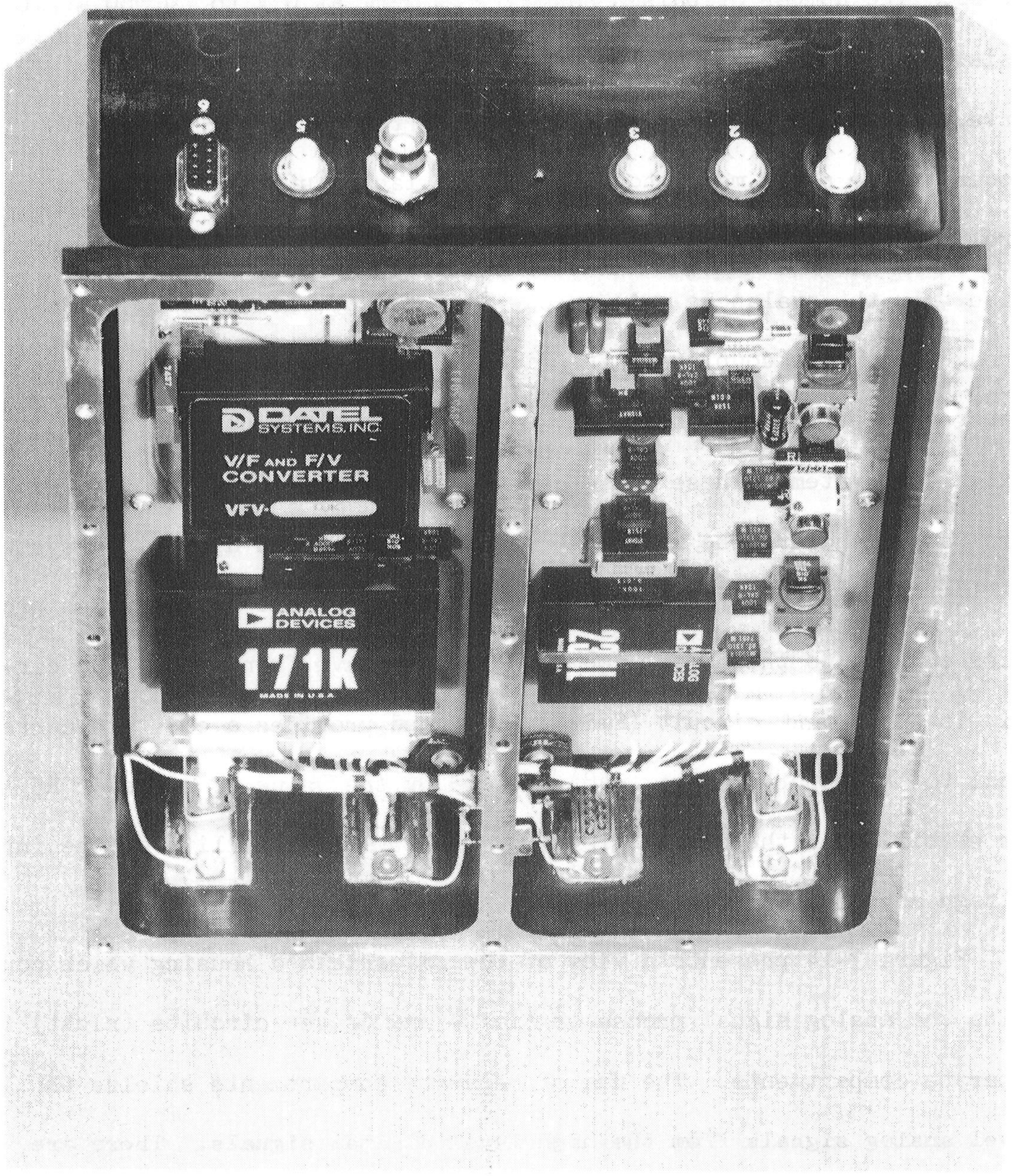

Figure 3-14. View of the analog signal processor
and driver circuits.

video signal and the dc output voltage. These are used for monitoring of the radiometer operation by the operator.

A block diagram of the digital subsystem is shown in Fig. 3-15. The digital subsystem uses an Intel 8080 microprocessor for radiometer control and data processing. These data include time of day, date, radiometer operating parameters, output data, and thermodynamic temperature data. The data are formatted prior to being recorded on a digital tape recorder. Table 3-1 provides a list of data recorded.

TABLE 3-1

DATA RECORDED ON DIGITAL TAPE RECORDER

Identification Number
Day (Julian)
Hour
Minute
Second
1/10 Second
Mode
Frequency
Bandwidth
Delta Frequency
Sample Period
Sample Number
N_{CL}
N_G
Reference Temperature
Radome Temperature
Polarizer Temperature
Commutated Temperature
Commutated Temperature Label

Table 3-2 provides a list of the commutated thermodynamic temperature measurements.

TABLE 3-2

COMMUTATED TEMPERATURES

Waveguide to Coaxial Adapter
Output of Thermal Block
Input to Thermal Block
Antenna
0° C Reference
50° C Reference

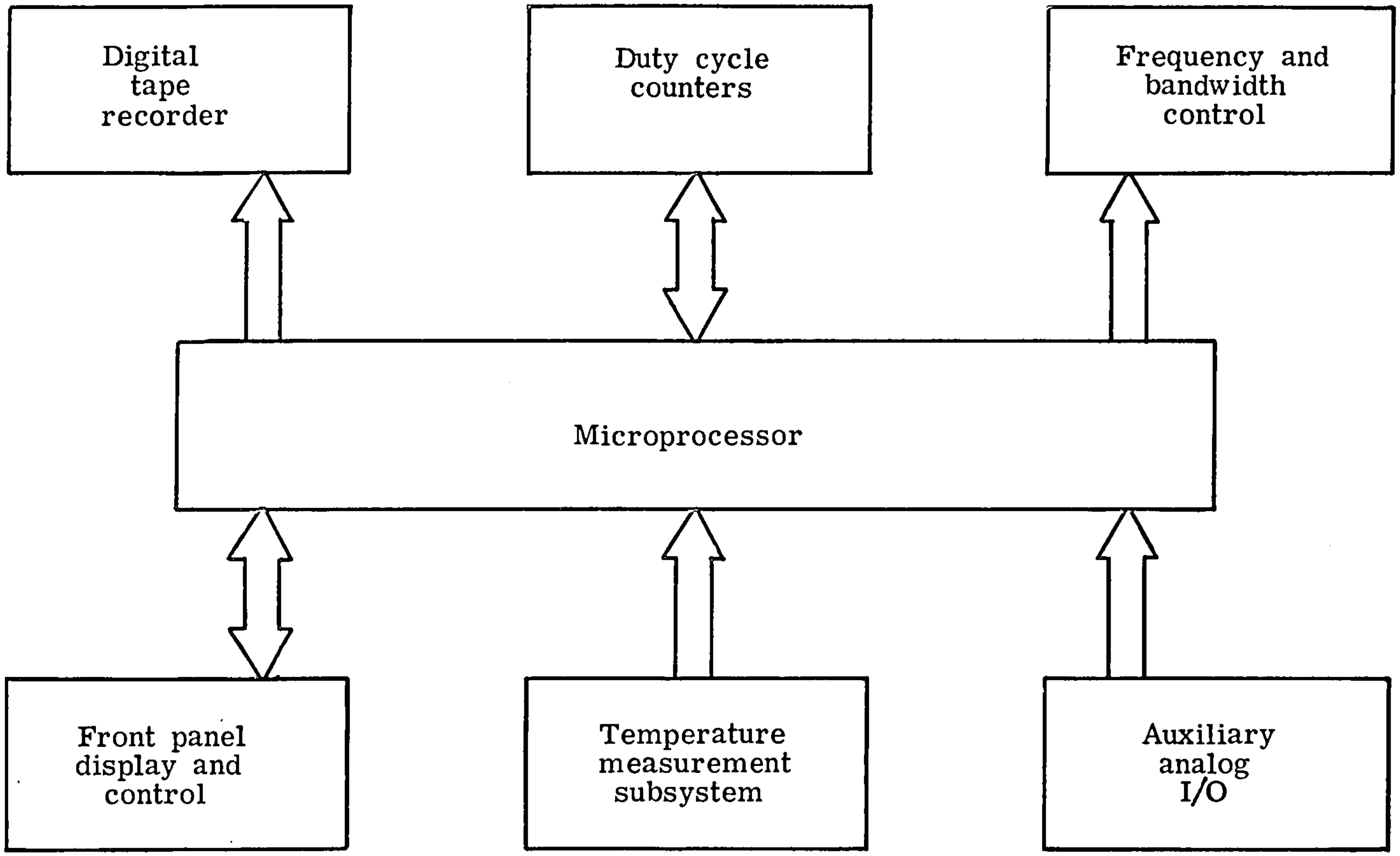

Figure 3-15. Block diagram of the digital subsystem.

The duty cycle of the 70 μs noise pulses is measured by the duty cycle counters. The integration time of the radiometric measurement is determined by the sample period which can be selected to be 0.2, 0.5, 1, 2, 5, 10, or 20 s. The minimum response time of the loop is such that the radiometer accurately responds to input noise temperature changes in 40 ms. The longer the sample period, the smaller a change in received antenna noise temperature can be resolved. However, in a dynamic measurement such as remote sensing from an aircraft, the larger will be the surface area integrated during the sample period. A 5 MHz clock is counted for the sample period and recorded as the N_{CL} counter. The 5 MHz clock is gated by the variable duty cycle 70 μs pulse. This gated 5 MHz signal is counted during the sample period and recorded as the N_G count. During post processing of the data, the duty cycle is obtained from N_G/N_{CL}. The frequency and bandwidth controls were discussed in the previous section on the receiver.

The front panel display and control is shown in Fig. 3-16. This rack mounted unit provides the interface between the operator and the SFMR. The SFMR can be operated either from a random access memory (RAM) which is programmed by the front panel controls or by preprogrammed read only memories (PROM's). The mode switch selects either the RAM or one of the PROM's. After mode selection, the SFMR operates under microprocessor control when the RUN/STOP switch is in the RUN position. A complete data set is recorded on the digital recorder each sample period. The duty cycle is converted to an estimate of the measured radiometric brightness temperature and displayed on the front panel.

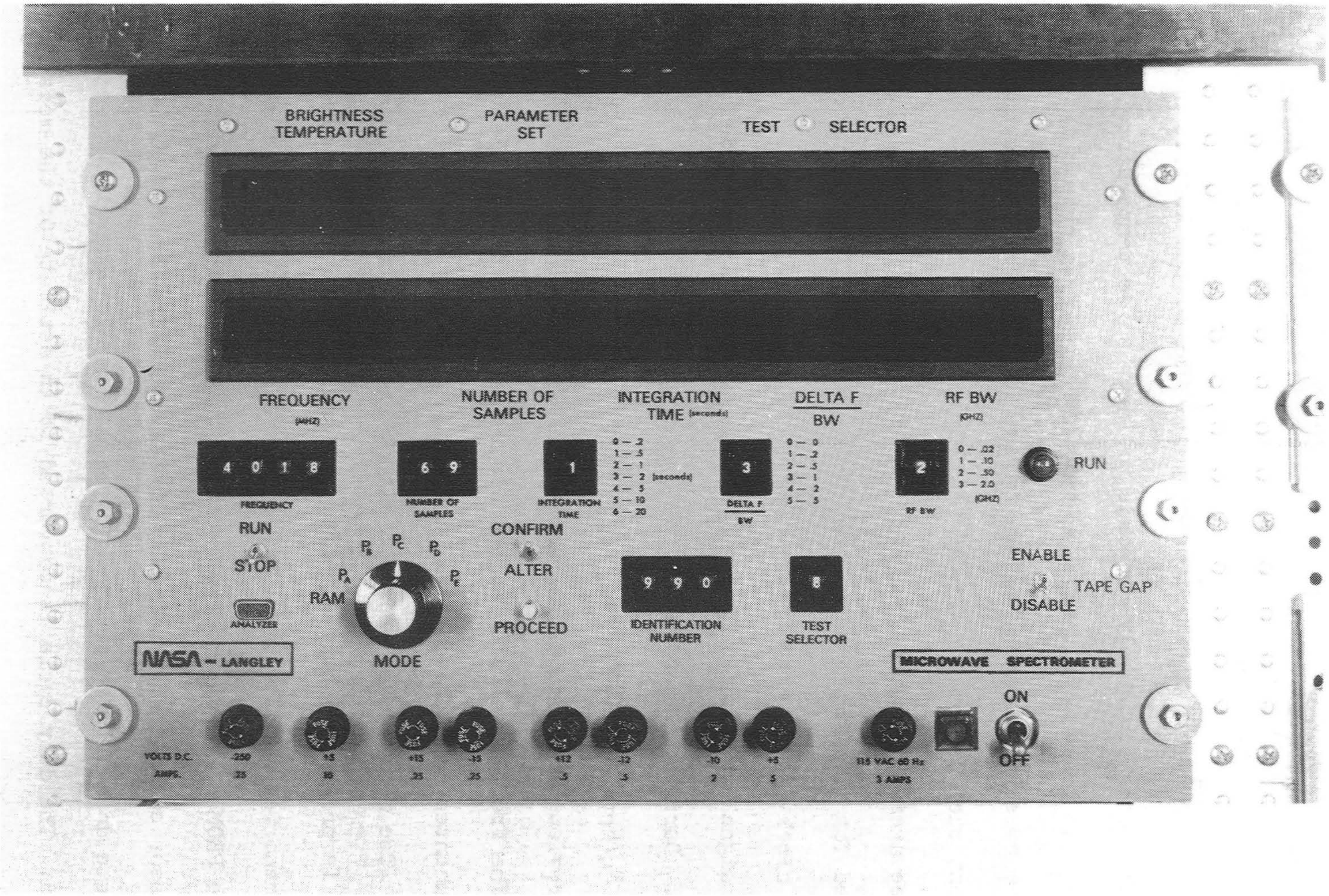

Figure 3-16. Front panel view of the digital controller for the stepped frequency microwave radiometer (microwave spectrometer).

Also, the frequency, sample number, sample period, delta frequency, and predetection bandwidth are displayed while the radiometer is operating.

Analysis

A quantity called ΔT determines the ability of a radiometer to measure changes in the antenna temperature. It is defined as the change in the input noise temperature which produces a change in the output estimate equal to the RMS value of the net output fluctuations. The sensitivity of a Dicke square wave modulated radiometer is (Stanley, 1979a)

$$\Delta T = 2\left(\frac{2B_{no}}{B_{si}}\right)^{1/2} T_{eff} \, . \tag{3-9}$$

The effective temperature T_{eff} is

$$T_{eff} = \left[\frac{(T_A + T_R)^2 + (T_O + T_R)^2}{2}\right]^{1/2} . \tag{3-10}$$

For the balanced Dicke square wave modulated radiometer $T_A = T_O$ and (3-10) become

$$T_{eff} = T_O + T_R \, . \tag{3-11}$$

Substituting (3-11) into (3-9) yields

$$\Delta T = 2\left(\frac{2B_{no}}{B_{si}}\right)^{1/2} (T_O + T_R) \, . \tag{3-12}$$

The equivalent noise bandwidth B_{no} of the output filter is:

$$B_{no} = \frac{1}{H_0^2(0)} \int_0^\infty \left|H_0^2(f)\right|^2 df \tag{3-13}$$

where $H_0(f)$ is the transfer function of the output filter. Since the SFMR uses discrete integration in the form of a summation over the sample period, the equivalent noise bandwidth is (Stanley, 1979a):

$$B_{no} = \frac{1}{2t_s} \tag{3-14}$$

where t_s is the sample period. The sample period is equivalent to the integration time.

The radiometer converts noise power to a noise voltage in a square law detector. For square law devices, B_{si} is the equivalent statistical bandwidth (Bendat and Piersol, 1971) and is defined by:

$$B_{si} = \frac{\left[\int_0^\infty \left|H_i(f)\right|^2 df\right]^2}{\int_0^\infty \left|H_i(f)\right|^4 df} \tag{3-15}$$

where $H_i(f)$ is the transfer function of the predetection filters. The equivalent statistical bandwidths of low pass Butterworth filters up to ten poles and Chebyshev filters up to eight poles for six different passband ripple levels have been computed by Stanley and Peterson (1979) and are tabulated along with the corresponding noise bandwidths. The SFMR uses seven pole low pass Butterworth filters and the equivalent statistical bandwidth is related to the half power bandwidth B_3 by

$$B_{si} = 1.086B_3 . \tag{3-16}$$

The sensitivity of the SFMR can be obtained by substitution of (3-14) and (3-16) into (3-12) which yields

$$\Delta T = 1.92\left(\frac{1}{B_3 t_s}\right)^{1/2}(T_0 + T_R). \tag{3-17}$$

The sensitivity of the SFMR as a function of the predetection bandwidth and integration time is presented in Fig. 3-17. The Dicke reference temperature for the SFMR is 308 K and the receiver temperature is 600 ± 75 K.

The sensitivity of the SFMR calculated from (3-17) determines the sensitivity at the noise temperature comparison point, i.e., the input to the Dicke circulator switch. The sensitivity to changes in the brightness temperature of the surface is the sensitivity of interest in remote sensing applications. The losses between the surface and noise temperature comparison point decreases this sensitivity. If the surface thermodynamic temperature is the geophysical parameter of interest, the sensitivity to a change in surface thermodynamic temperature is additionally reduced by the emissivity of the surface.

The effect of loss α_R between the input to the antenna T_A and the measured noise temperature T_M at the noise temperature comparison point can be determined as follows:

$$T_M = T_A(1 - \alpha_R) + \alpha_R T_\alpha . \tag{3-18}$$

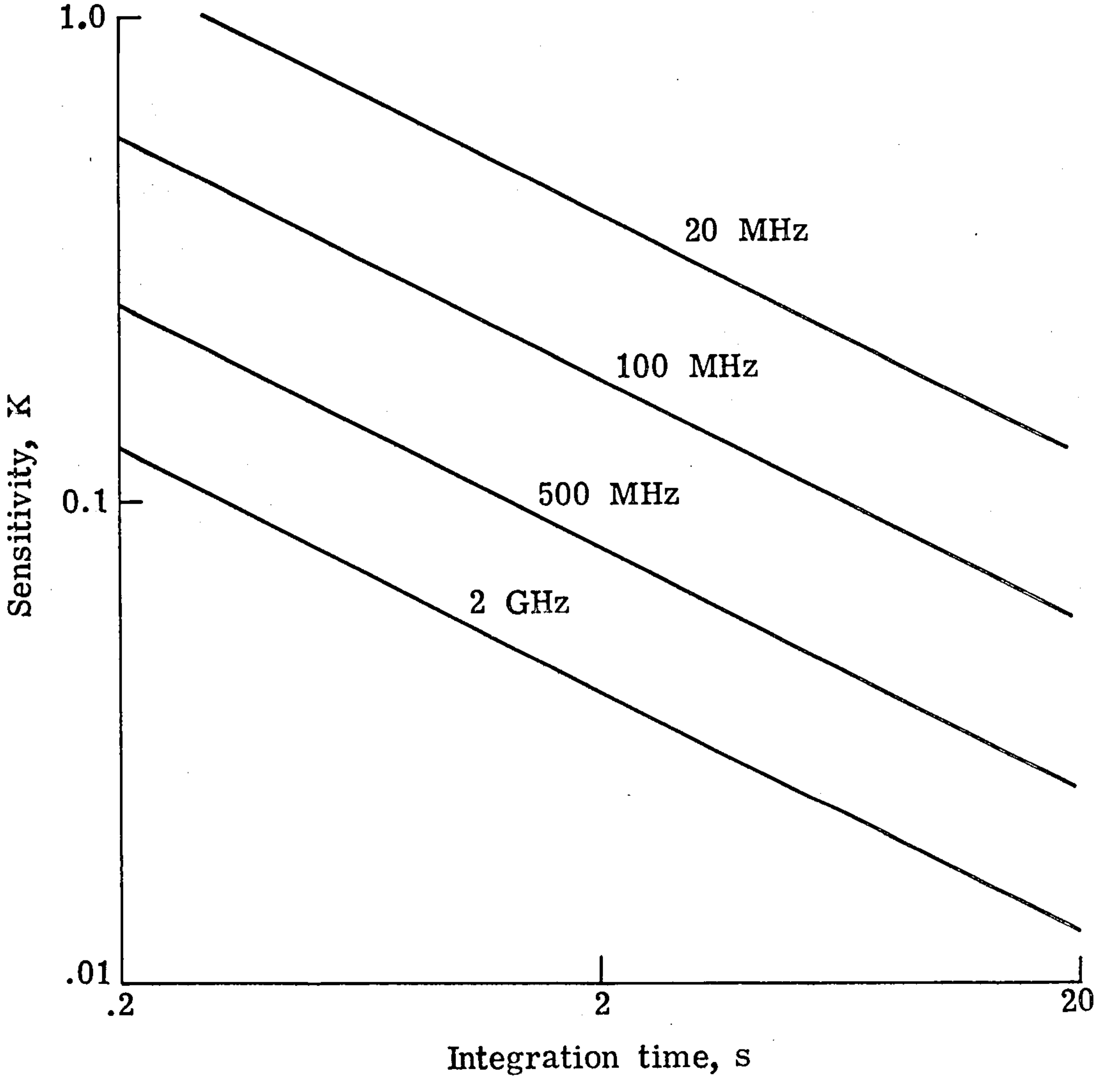

Figure 3-17. Sensitivity of a balanced Dicke radiometer versus integration time for predetection bandwidths from 20 MHz to 2 GHz, receiver noise temperature of 600 K, and a Dicke reference temperature of 308 K.

where T_α is the thermodynamic temperature of the loss. The change in T_A is related to the change in T_M by

$$\Delta T_A = \frac{\partial T_A}{\partial T_M} \Delta T_M . \tag{3-19}$$

The partial derivative obtained from (3-18) is substituted into (3-19) yielding

$$\Delta T_A = \left(\frac{1}{1 - \alpha_R}\right) \Delta T_M . \tag{3-20}$$

The change in surface thermodynamic temperature ΔT_S for a change in antenna noise temperature ΔT_A is

$$\Delta T_S = \frac{\partial T_S}{\partial T_A} \Delta T_A . \tag{3-21}$$

The partial derivative can be determined from (2-36). Substitution of it along with (3-20) into (3-21) yields

$$\Delta T_S = \frac{1}{e(1 - \tau)(1 - \alpha_R)} \Delta T_M . \tag{3-22}$$

The ΔT_M is a function of the radiometer predetection bandwidth and integration time and can be found from Fig. 3-17. The decreased sensitivity expressed as the ratio of ΔT_S to ΔT_M for remote measurement of ocean temperature as a function of radiometer loss α_R is shown in Fig. 3-18. The ratio is computed at a frequency of 6 GHz, emissivity of 0.3624, and opacity of 0.99894 corresponding to an altitude of 300 m. If $\alpha_R = 0$, the ratio of ΔT_S to ΔT_M would be 2.76 which is the

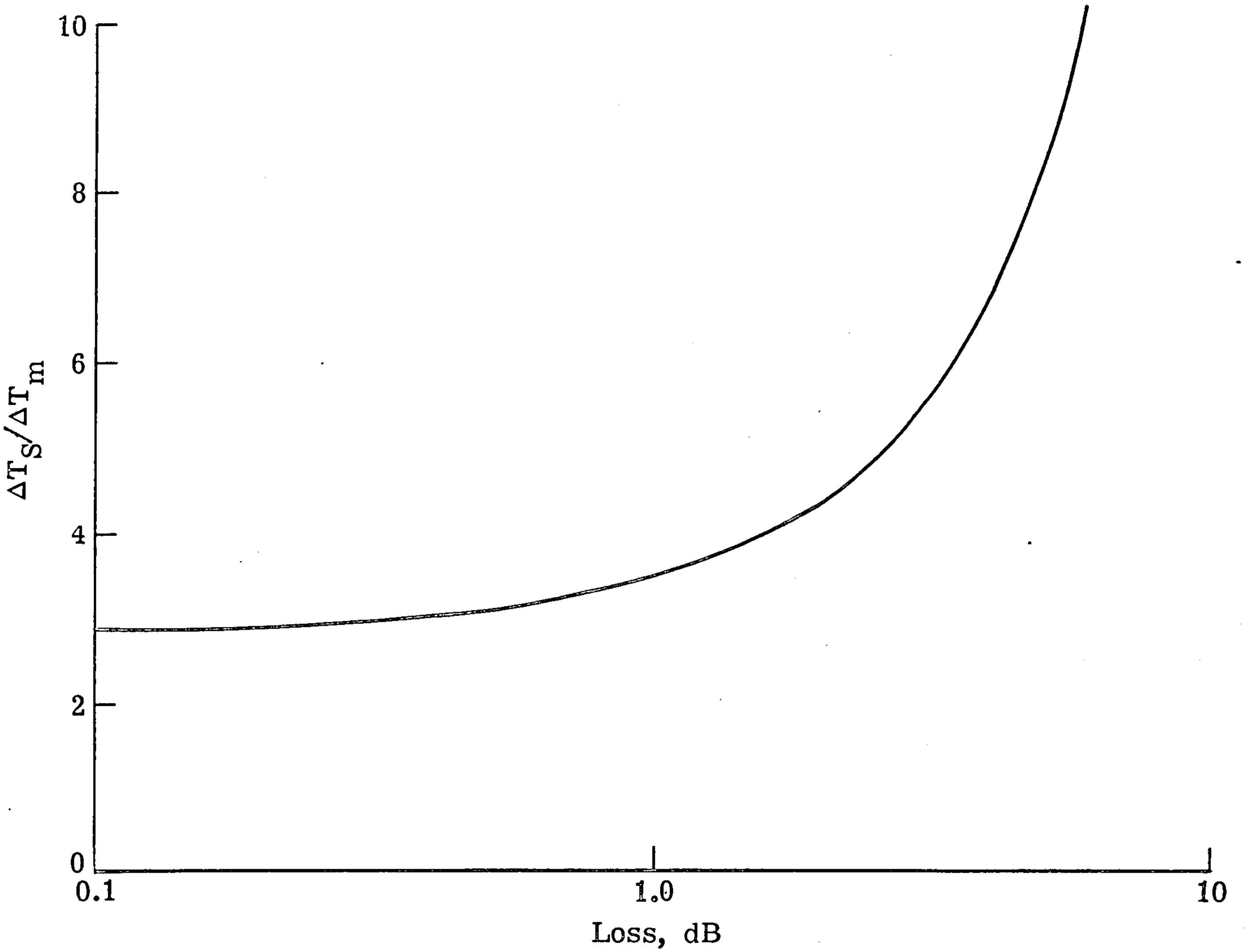

Figure 3-18. Ratio of the change in surface temperature to the resulting change in radiometer measured temperature versus loss prior to comparison junction at a surface temperature of 10° C, emissivity of 0.3624, altitude of 500 m, and frequency of 6 GHz.

result of the emissivity and opacity. As the loss increases to 1 dB, which is the SFMR loss, this ratio increases to 3.48. The ratio increases rapidly for further increases in loss reaching about 9 at 5 dB and 28 at 10 dB. Therefore, it is obvious that it is very important to minimize the losses in the radiometer.

The analysis of the closed loop feedback system used in SFMR has been performed by Stanley, Lawrence, and Jeffords of Old Dominion University Research Foundation in conjunction with a research effort to develop digital signal processing for microwave radiometers. The results from this analysis (Stanley, 1979b) showed that the response time of the second order feedback loop was approximately 40 ms. This was confirmed by step response testing performed on the SFMR.

The transfer function of the SFMR feedback loop is:

$$\frac{V_0(s)}{T_0(s) - T_A(s)} = \frac{K_1}{(s + 50)^2} \qquad (3\text{-}23)$$

where K_1 is the forward gain constant.

A simulation model of the SFMR has been developed using both the Continuous System Modeling Program (CSMP) at Old Dominion University and Advanced Continuous Simulation Language (ACSL) at Langley Research Center. The comparison between the simulation results and laboratory measurements showed excellent agreement (Stanley, et al., 1979, and Lawrence, et al., 1980).

An analysis of the accuracy of the SFMR is accomplished by first developing the equation used to relate the duty cycle of the injected noise pulses to the received antenna noise temperature at the input of the antenna subsystem. The effect of reflection and absorption by the antenna subsystem and microwave front end prior to the noise temperature comparison point is modeled by a single reflection and loss. Both of these are functions of frequency. The noise emitted by the modeled loss will be determined from a composite thermodynamic temperature which is computed from the measured thermodynamic temperature of the different loss elements.

The second order closed loop feedback system of the SFMR ensures the following condition at the comparison point

$$T_O = T_I + T_M + \text{loop error} \tag{3-24}$$

where T_O is the Dicke reference temperature, T_I is the injected noise temperature, and T_M is the received noise temperature at the comparison point. The loop error of a second order loop is zero for steady state conditions which are reached after about three time constants or 120 ms in the SFMR. The injected noise temperature is

$$T_I = \left(\frac{N_G}{N_{CL}}\right)k_R \tag{3-25}$$

where N_G is the count of the gated clock pulses, N_{CL} is the count of the ungated clock pulses, and k_R is a calibration factor which is the effective amplitude of the noise injection pulses in terms of duty cycle. The calibration factor is a function of both frequency and thermodynamic temperature. It is in units of K. Defining the ratio of N_G to N_{CL} as the duty cycle d_N, and substitution of (3-25) into (3-24) yields

$$T_M = T_0 - d_N k_R . \tag{3-26}$$

The relation of T_M to T_A, the antenna noise temperature at the input to the antenna subsystem, for a one loss element model is given by

$$T_M = T_A(1 - r_R)(1 - \alpha_R) + \alpha_R \hat{T}_{\alpha_R} \tag{3-27}$$

where r_R and α_R are the power reflection coefficient and absorption coefficient of the loss element.

The composite thermodynamic temperature $\hat{T}_{\alpha_R}$ is calculated from

$$\hat{T}_{\alpha_R} = \sum_{i=1}^{4} \left(\frac{\alpha_i}{\alpha_R}\right) T_{\alpha_i} \tag{3-28}$$

where the thermodynamic temperature T_{α_1}, T_{α_2}, T_{α_3}, and T_{α_4} are the temperatures of the radome, polarizer, antenna, and microwave front end, respectively. Since the antenna temperature is measured at three different locations, a composite antenna temperature is determined from

$$T_{\alpha_3} = 0.291 T_{ant1} + 0.5 T_{ant2} + 0.209 T_{ant3} . \tag{3-29}$$

The multiplication factors were determined from the cross sectional dimensions of the antenna since the loss per unit length of the antenna is inversely proportional to the area of the antenna (Love, et al., 1975). The nominal losses for the radome, polarizer, antenna, and microwave front end have been measured and are 0.030, 0.035, 0.020, and 0.115, respectively, with a total loss α_R of 0.20. Therefore (3-28) becomes

$$\hat{T}_{\alpha_R} = 0.150T_{rad} + 0.175T_{pol} + 0.03T_{ant1} + 0.05T_{ant2} + 0.02T_{wg} + 0.575T_O. \tag{3-30}$$

The thermodynamic temperature of the radome T_{rad}, polarizer T_{pol}, antenna T_{ant1} and T_{ant2}, waveguide to coaxial adapter T_{wg}, and microwave front end T_O are measured and recorded by the digital subsystem during radiometer operation.

The basic radiometer equation is obtained through the substitution of (3-27) in (3-26) and is

$$T_A = \frac{\left(T_O - d_N k_R - \alpha_R \hat{T}_{\alpha_R}\right)}{(1 - r_R)(1 - \alpha_R)}. \tag{3-31}$$

The effect of the accuracy of the knowledge of each factor in (3-31) can be determined through the partial derivative of T_A with respect to each factor, then substitution of typical values to obtain an estimate of the change in T_A due to a change in each factor. The partial derivatives are

$$\frac{\partial T_A}{\partial r_R} = \frac{\left(T_O - d_N k_R - \alpha_R \hat{T}_{\alpha_R}\right)}{(1 - r_R)^2 (1 - \alpha_R)} \tag{3-32}$$

$$\frac{\partial T_A}{\partial \alpha_R} = \frac{\left(T_O - d_N k_R - \hat{T}_{\alpha_R}\right)}{(1 - r_R)(1 - \alpha_R)^2} \tag{3-33}$$

$$\frac{\partial T_A}{\partial T_O} = \frac{1}{(1 - r_R)(1 - \alpha_R)} \tag{3-34}$$

$$\frac{\partial T_A}{\partial d_N} = \frac{-k_R}{(1 - r_R)(1 - \alpha_R)} \tag{3-35}$$

$$\frac{\partial T_A}{\partial k_R} = \frac{-d_N}{(1 - r_R)(1 - \alpha_R)} \tag{3-36}$$

$$\frac{\partial T_A}{\partial \hat{T}_{\alpha_R}} = \frac{-\alpha_R}{(1 - r_R)(1 - \alpha_R)} \, . \tag{3-37}$$

The various changes in T_A due to a change in each of the six factors are

$$\Delta T_{A_1} = \left(\frac{\partial T_A}{\partial r_R}\right) \Delta r_R \tag{3-38}$$

$$\Delta T_{A_2} = \left(\frac{\partial T_A}{\partial \alpha_R}\right) \Delta \alpha_R \tag{3-39}$$

$$\Delta T_{A_3} = \left(\frac{\partial T_A}{\partial T_O}\right) \Delta T_O \tag{3-40}$$

$$\Delta T_{A_4} = \left(\frac{\partial T_A}{\partial d_N}\right) \Delta d_N \tag{3-41}$$

$$\Delta T_{A_5} = \left(\frac{\partial T_A}{\partial k_R}\right) \Delta k_R \tag{3-42}$$

$$\Delta T_{A_6} = \left(\frac{\partial T_A}{\partial \hat{T}_{\alpha_R}}\right) \Delta \hat{T}_{\alpha_R} \, . \tag{3-43}$$

Since the factors are statistically independent, the overall change in ΔT_A is the root sum square of the individual ΔT_A from (3-38) through (3-43).

$$\Delta T_A = \left(\sum_{i=1}^{6} \Delta T_{A_i}{}^2 \right)^{1/2} . \qquad (3\text{-}44)$$

The following typical values for a measurement by the SFMR are given in Table 3-3 and will be used in the evaluation of the partial derivatives.

TABLE 3-3

TYPICAL VALUES FOR SFMR MEASUREMENT

$T_A = 100$ K
$\hat{T}_{\alpha_R} = 270$ K
$T_O = 308$ K
$k_R = 200$ K
$d_N = 0.5000$
$r_R = 0.05$
$\alpha_R = 0.20$

Substitution of values from Table 3-3 in (3-32) through (3-43) yields

$$\Delta T_{A_1} = 212.7 \; \Delta r_R \qquad (3\text{-}45)$$

$$\Delta T_{A_2} = -103.4 \; \Delta \alpha_R \qquad (3\text{-}46)$$

$$\Delta T_{A_3} = 1.33 \; \Delta T_O \qquad (3\text{-}47)$$

$$\Delta T_{A_4} = -265.1 \; \Delta d_N \qquad (3\text{-}48)$$

$$\Delta T_{A_5} = 0.66\ \Delta k_R \tag{3-49}$$

$$\Delta T_{A_6} = -0.27\ \Delta \hat{T}_{\alpha_R}. \tag{3-50}$$

The accuracy goal of this research is to achieve an absolute accuracy of 0.5 K and a relative accuracy of 0.1 K. In order to obtain these accuracies r_R would have to be known to within ±0.0005, α_R to within ±0.001, T_0 to within ±0.075, d_N to within ±0.0004, k_R to within ±0.15 K, and $\hat{T}_{\alpha_R}$ to within 0.37K. Other than d_N which is known to an accuracy of ±0.00004, α_R, r_R, and k_R must be determined by calibration. The values of T_0 and $\hat{T}_{\alpha_R}$ are measured to within 0.1 K.

The accuracy of the SFMR is achieved through the excellent long term stability of the instrument. This stability has been demonstrated for the design technique used in the SFMR by stability tests on the 2.65 GHz radiometer (Hardy, et al., 1974). This radiometer was calibrated at different times over a $3\frac{1}{2}$ year period with an RMS variation in the calibration repeatability of 0.7 K (Blume, 1977). The long term stability of this design technique allows an accurate calibration to be performed prior to each mission. This composite calibration factor accounts for the effects of r_R, α_R, and k_R thereby eliminating the requirement of a precise knowledge of each factor.

The calibration of the radiometer is performed by two different methods to obtain an accurate antenna noise temperature for use as a calibration source. One method is to point the radiometer towards the zenith and use the zenith value of the radiometric brightness temperature of the sky as the calibration temperature. The second method is shown in Fig. 3-19. A cooled reference termination was used to provide a known calibration noise temperature input to the radiometer. This was developed for calibration of the 2.65 GHz precision radiometer (Hardy, 1973). The termination consists of a porous microwave absorber which is filled with liquid nitrogen. The absorber is nearly a perfect blackbody and therefore the radiometric brightness temperature is equal to the thermodynamic temperature. The emissivity of this type of termination has been measured and found to be 0.9999 (Hardy, 1973). The thermodynamic temperature is the boiling point of liquid nitrogen which is

$$T_{CAL} = 77.36 + 0.011(P_C - 760.) \tag{3-51}$$

where P_C is the barometric pressure in mm of mercury during calibration.

The calibration factor can be determined when the antenna noise temperature is accurately known by setting $T_A = T_{CAL}$ in (3-31) yielding

$$k_R + \left(\frac{\alpha_R}{d_{N_C}}\right)\hat{T}_{\alpha RC} + \left(\frac{r_R + \alpha_R}{d_{N_C}}\right)T_{CAL} = \frac{1}{d_{N_C}}(T_0 - T_{CAL}) \tag{3-52}$$

where d_{N_C} is the duty cycle during calibration and $\hat{T}_{\alpha_C}$ is the composite thermodynamic temperature of the loss during calibration. The only factor which varies between the calibration at a specific frequency

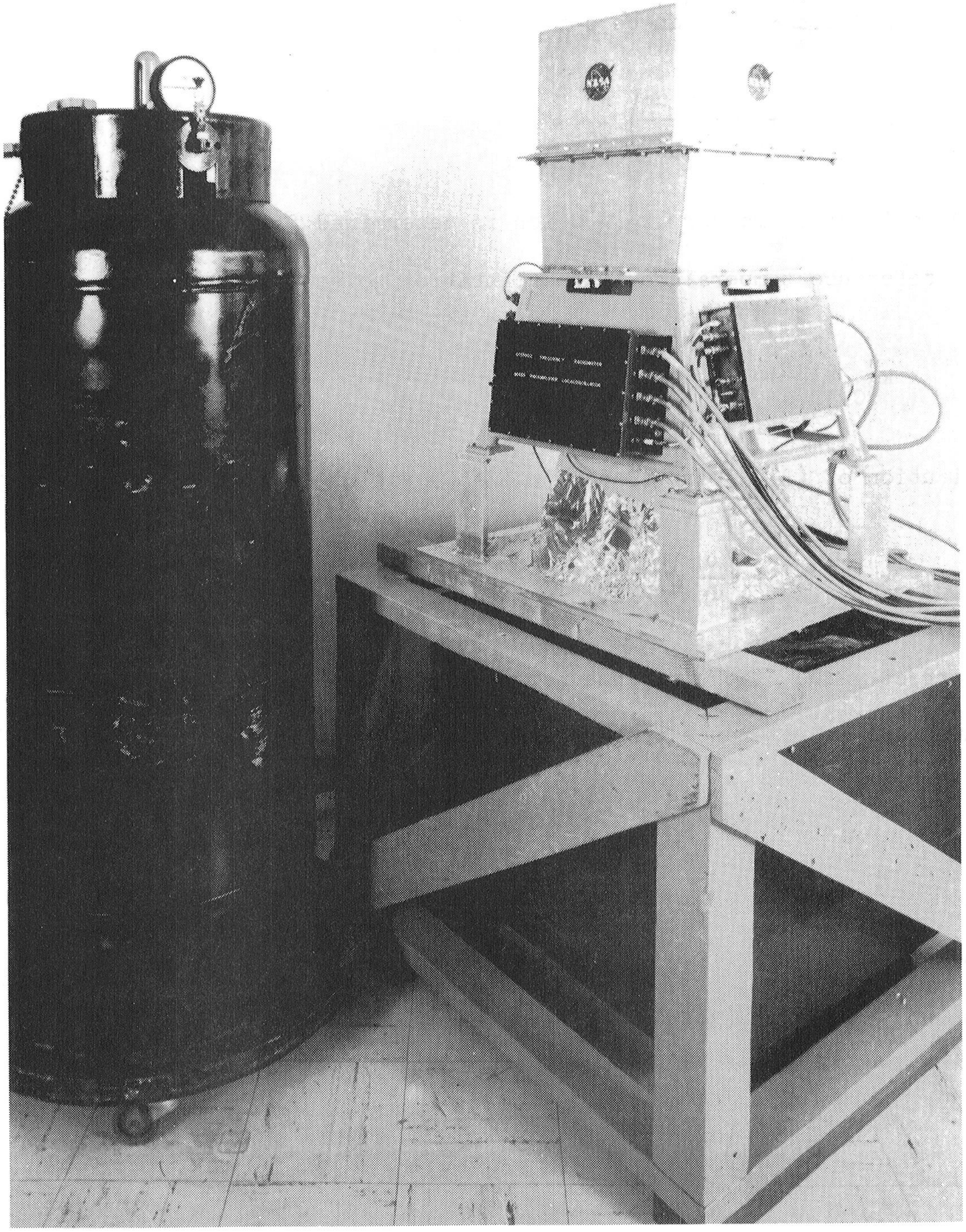

Figure 3-19. Calibration of the stepped frequency microwave radiometer.

and a measurement at the same frequency is $\hat{T}_{\alpha_R}$. Therefore a new calibration factor k_R' can be defined as

$$k_R' = k_R + \left(\frac{r_R + \alpha_R}{d_{N_C}}\right) T_{CAL} \, . \tag{3-53}$$

A calibration factor k_{R_C}'' which is determined from the duty cycle, reference temperature, and calibration noise temperature is

$$k_{R_C}'' = \frac{1}{d_{N_C}}(T_0 - T_{CAL}) \, . \tag{3-54}$$

Substitution of (3-53) and (3-54) in (3-52) yields

$$k_{R_C}'' = k_R' + \left(\frac{\alpha_R}{d_{N_C}}\right)\hat{T}_{\alpha_C} \, . \tag{3-55}$$

The correct value of the antenna noise temperature can be obtained from the duty cycle, reference temperature, and calibration factor by

$$T_A = T_0 - d_{N_M} k_{R_M}'' \tag{3-56}$$

where k_{R_M}'' is the calibration factor during the measurement. It is different from k_{R_C}'' since $\hat{T}_{\alpha_M}$ is different from $\hat{T}_{\alpha_C}$. In an analogous fashion to (3-55), k_{R_M}'' is

$$k_{R_M}'' = k_R' + \left(\frac{\alpha_R}{d_{N_M}}\right)\hat{T}_{\alpha_M} . \tag{3-57}$$

Substitution of (3-55) in (3-57) yields

$$k''_{R_M} = k''_{R_C} + \alpha_R \left[\left(\frac{\hat{T}_{\alpha_M}}{d_{N_M}} \right) - \left(\frac{\hat{T}_{\alpha_C}}{d_{N_C}} \right) \right] . \tag{3-58}$$

The first term in (3-58) is the composite calibration factor determined during calibration including the effects of reflection and absorption in the antenna subsystem and microwave front end. This composite calibration factor is a function of frequency. The second term is a correction factor that corrects for the different thermodynamic temperature of the radiometer during calibration and measurement.

The accuracy of the measurements results from the bias errors which determine the absolute accuracy and the random noise errors which determine the relative accuracy. Random noise errors can be both rapidly changing errors such as the ΔT error due to radiometer sensitivity or slowly varying errors due to slow changes in thermodynamic temperatures. The bias errors can be divided into those errors at the time of calibration which result in an absolute error between the true calibration factor and the estimate of the calibration factor, changes in the true calibration factor between the time of calibration and time of measurement, and bias errors in the correction factor. The random errors are determined by the quantization error in T_O, quantization error in the correction factor due to quantization of $\hat{T}_{\alpha_M}$ and $\hat{T}_{\alpha_C}$, and the sensitivity ΔT.

The error in the calibration factor k''_{R_C} can be estimated from (3-54). Taking the partial derivative of k''_{R_C} with respect to T_O and T_{CAL} yields

$$\frac{\partial k''_{R_C}}{\partial T_O} = \frac{1}{d_{N_C}} \tag{3-59}$$

$$\frac{\partial k''_{R_C}}{\partial T_{CAL}} = -\frac{1}{d_{N_C}} \tag{3-60}$$

$$\frac{\partial k''_{R_C}}{\partial (T_O - T_{CAL})} = \frac{1}{d_{N_C}} \tag{3-61}$$

where (3-61) represents the error due to radiometer sensitivity ΔT during calibration.

Typical values taken during calibration prior to a mission and measurements during that mission are given in Table 3-4. These will be used in obtaining an estimate of the absolute and relative accuracies of the SFMR.

TABLE 3-4

TYPICAL VALUES DURING CALIBRATION AND MEASUREMENT

	Calibration	Measurement
T_{rad}	292.84 K	270.68 K
T_{pol}	296.28 K	279.59 K
T_{ant1}	296.74 K	282.40 K
T_{ant2}	297.99 K	288.02 K
T_{wg}	303.46 K	303.65 K
$\hat{T}_{\alpha_R}$	300.01 K	295.71 K
T_{CAL}	77.51 K	---
T_0	308.25 K	308.24 K
k''_{R_C}	367.7 K	---
ΔT	0.25 K	0.36 K
d_{N_C}	0.62738	---
d_{N_M}	---	0.56000

Substitution of values from Table 3-4 in (3-59), (3-60), and (3-61), and formation of the root sum square of the individual errors (since each is statistically independent) result in an estimate of the bias error in k''_{R_C} of 0.457 K.

The error in k''_{R_M} can be estimated from (3-58) by taking the partial derivative of k''_{R_M} with respect to k''_{R_C}, α_R, $\hat{T}_{\alpha_M}$, and $\hat{T}_{\alpha_C}$. The partial derivatives are

$$\frac{\partial k''_{R_M}}{\partial k''_{R_C}} = 1 \tag{3-62}$$

$$\frac{\partial k''_{R_M}}{\partial \alpha_R} = \left(\frac{\hat{T}_{\alpha_M}}{d_{N_M}} - \frac{\hat{T}_{\alpha_C}}{d_{N_C}}\right) \tag{3-63}$$

$$\frac{\partial k''_{R_M}}{\partial \hat{T}_{\alpha_M}} = \frac{\alpha_R}{d_{N_M}} \tag{3-64}$$

$$\frac{\partial k''_{R_M}}{\partial \hat{T}_{\alpha_C}} = -\frac{\alpha_R}{d_{N_C}}\,. \tag{3-65}$$

Substitution of values from Table 3-4 in (3-62) through (3-65) and taking the root sum square of each error (since each error source is statistically independent) result in an estimate of the bias error in k''_{R_M} of 0.71 K.

The error in measurement of the antenna noise temperature T_A can be estimated from (3-56) by taking the partial derivatives of T_A with respect to T_O and k''_{R_M}. Substitution of typical values from Table 3-4 and the estimate of error in k''_{R_M}, the bias error in T_A is the root sum square of the statistically independent error sources and is 0.41 K.

The random root mean square (RMS) error due to quantization of T_O, $\hat{T}_{\alpha_M}$, and $\hat{T}_{\alpha_C}$ is equal to 0.29 times the quantization step (Bendat and Piersol, 1971). The quantization steps in T_O, $\hat{T}_{\alpha_M}$, and $\hat{T}_{\alpha_C}$ are 0.04, 0.16, and 0.16, respectively. The RMS error in T_A due to quantization error can be found by taking the partial derivatives of T_A with respect to T_O, $\hat{T}_{\alpha_M}$, and $\hat{T}_{\alpha_C}$; multiplying by the RMS error in T_O,

$\hat{T}_{\alpha_M}$, and $\hat{T}_{\alpha_C}$; and taking the root sum square of each error source since each is statistically independent. The resulting error in T_A due to quantization of T_0, $\hat{T}_{\alpha_M}$, and $\hat{T}_{\alpha_C}$ is 0.014 K.

The other component of the random noise error is due to the radiometer sensitivity which is a function of the predetection bandwidth and integration time and can be determined from Fig. 3-17 for the SFMR. The measurement used as an example in Table 3-4 used a bandwidth of 100 MHz and an integration time of 1 s, the resulting ΔT was 0.36K. To achieve a sensitivity of 0.1 K, either the bandwidth must be increased to 500 MHz or the integration time to 6 s. However, in all cases except a bandwidth of 2 GHz with an integration time >10 s, the effective noise error is determined by the radiometer sensitivity. Measurements of the stability of the instrument over periods of several hours have shown that any slow drifts in the calibration factor are of an undetectable magnitude.

The relative accuracy of the SFMR is only a function of the sensitivity ΔT which can be set anywhere between 1.25 K and 0.0125 K depending on the choice of predetection bandwidth and integration time. The absolute accuracy of the SFMR is the root sum square of the bias error and the relative accuracy. For a ΔT of 0.1 K, the absolute accuracy is 0.42 K.

CHAPTER IV

RADIOMETER ALGORITHMS

Radiative Transfer Equation Algorithm

The solution of the radiative transfer equation (2-36) developed in Chapter II requires the evaluation of a complex equation including several time consuming numerical integration routines. It is desired to calculate the theoretical brightness temperature for each of the multitude of actual data measurements and compare these with the measured brightness temperature from the stepped frequency microwave radiometer (SFMR). Therefore, a simplified algorithm to replace the exact solution of the radiative transfer equation described in Appendix B is required in order to improve the computational efficiency. This simplification is accomplished through the development of regression fit equations to compute the opacity of the atmosphere at the measurement altitude and the total atmospheric opacity. An expression for the mean thermodynamic temperature of the atmosphere and the effective downwelling brightness temperature of the atmosphere is determined that meets the accuracy requirements of this research.

The equations for opacity were determined by parametrically solving the equations for the absorption coefficients due to oxygen and water vapor, then numerically integrating over the altitude range to solve for opacity. Explicit regression fit equations for opacity as functions of the required dependent variables were developed using a least squares fit to the parametric opacity equations. These equations must be established to an accuracy sufficient to determine the theoretical radiometric antenna temperature to within 0.1 K. A sensitivity analysis of the radiative transfer equation is accomplished to determine the accuracy to which the various factors must be established to realize the overall accuracy requirement.

Prior to performing the sensitivity analysis, (2-36) is simplified by the elimination of the two integrations. The first integration determines the downwelling brightness temperature T'_{dw} of the atmosphere due to the absorption coefficient $\alpha_a(z,f)$ and is defined by

$$T'_{dw} = \int_0^{\infty} \alpha_a(z,f)T(z)\left[1 - \sec\theta\tau(z,f)\right] dz . \tag{4-1}$$

The second integration determines the upwelling brightness temperature T_{uw} of the atmosphere between the radiometer and the surface. This is defined by

$$T_{uw} = \int_0^{h_r} \alpha_a(z,f)T(z)\left[1 - \sec\theta\tau(z,f)\right] dz . \tag{4-2}$$

Replacing $T(z)$ in (4-1) and (4-2) with a mean thermodynamic temperature $\langle T \rangle$ and $\tau(z,f)$ with a mean opacity $\langle \tau \rangle$, then (4-1) and (4-2) become after substitution of (2-34) and (2-35)

$$T'_{dw} = \left(1 - \sec\theta\langle\tau\rangle_a\right)\langle T\rangle_a \,\tau(\infty,f) \tag{4-3}$$

and

$$T_{uw} = \left(1 - \sec\theta\langle\tau\rangle_h\right)\langle T\rangle_h \,\tau(h,f) \tag{4-4}$$

where $\langle \tau \rangle_a$ and $\langle \tau \rangle_h$ represent the mean total atmospheric opacity and the mean opacity between the surface and altitude h_r respectively. The mean atmospheric thermodynamic temperature between the surface and the tropopause is represented by $\langle T \rangle_a$, and the mean atmospheric thermodynamic temperature between the surface and radiometer altitude h_r is represented by $\langle T \rangle_h$. The altitude of the tropopause represents the upper limit since 99.99 percent of the absorption occurs below this altitude. Substitution of (4-3) and (4-4) into (2-36) yields

$$\begin{aligned} T_A = \Bigg(eT_S + (1 - e)\Bigg\{&(1 - \sec\theta\tau_\infty)T_\infty \\ &+ \sec\theta\Big[\Big(1 - \sec\theta\langle \tau \rangle_a\Big)\langle T \rangle_a\,\tau_\infty\Big]\Bigg\}\Bigg)(1 - \sec\theta\tau_h) \\ &+ \sec\theta\Big(1 - \sec\theta\langle \tau \rangle_h\Big)\tau_h\langle T \rangle_h + C_1 + C_2 + C_3 \end{aligned} \qquad (4\text{-}5)$$

where C_1, C_2, and C_3 represent the antenna pattern correction, the wind correction, and the cloud correction factors, respectively. These are subsequently developed in this chapter.

The total downwelling temperature includes the extraterrestrial component T_∞, which is attenuated by the atmosphere, plus the component emitted by the atmosphere T'_{dw} and is determined by

$$T_{dw} = (1 - \sec\theta\tau_\infty)T_\infty + T'_{dw}\,. \qquad (4\text{-}6)$$

Substitution of (4-4) and (4-6) in (4-5) yields

$$T_A = \left[eT_S + (1 - e)T_{dw}\right](1 - \sec\theta\tau_h) \cdot + \sec\theta T_{uw} + C_1 + C_2 + C_3 \tag{4-7}$$

The accuracy to which the antenna temperature can be determined depends upon the accuracy of the knowledge of emissivity, surface thermodynamic temperature, downwelling brightness temperature, upwelling brightness temperature, opacity at altitude, incidence angle, and the three correction factors. The error in antenna temperature is the root sum square

$$\varepsilon_{T_A} = \left(\varepsilon_e^2 + \varepsilon_{T_S}^2 + \varepsilon_{T_{dw}}^2 + \varepsilon_{T_{uw}}^2 + \varepsilon_{\sec\theta}^2 + \varepsilon_{\tau_h}^2 + \varepsilon_{C_1}^2 + \varepsilon_{C_2}^2 + \varepsilon_{C_3}^2\right)^{1/2} \tag{4-8}$$

since each error source is statistically independent. Each error term in (4-8) can be determined from

$$\varepsilon_i = \left(\frac{\partial T_A}{\partial i}\right)\Delta i \tag{4-9}$$

where i represents the various variables.

The sensitivity factors, $\partial T_A/\partial i$, are evaluated using (4-7) and are listed below.

$$\frac{\partial T_A}{\partial e} = (T_S - T_{dw})(1 - \sec\theta\tau_h) \tag{4-10}$$

$$\frac{\partial T_A}{\partial T_S} = e(1 - \sec\theta\tau_h) \qquad (4\text{-}11)$$

$$\frac{\partial T_A}{\partial T_{dw}} = (1 - e)(1 - \sec\theta\tau_h) \qquad (4\text{-}12)$$

$$\frac{\partial T_A}{\partial T_{uw}} = \sec\theta \qquad (4\text{-}13)$$

$$\frac{\partial T_A}{\partial \sec\theta} = -\tau_h\left[eT_S + (1 - e)T_{dw}\right] + T_{uw} \qquad (4\text{-}14)$$

$$\frac{\partial T_A}{\partial \tau_h} = -\sec\theta\left[eT_S + (1 - e)T_{dw}\right] \qquad (4\text{-}15)$$

$$\frac{\partial T_A}{\partial C_1} = \frac{\partial T_A}{\partial C_2} = \frac{\partial T_A}{\partial C_3} = 1. \qquad (4\text{-}16)$$

The more stringent accuracy requirement occurs during the measurement of ocean surface temperature. A set of typical values for the various parameters from a measurement of ocean surface temperature is used in the evaluation of the sensitivity factors. Values selected are Emissivity = 0.36, Surface temperature = 288 K, Opacity at altitude = 0.01, Total opacity = 0.012, and Extraterrestrial temperature = 3 K. The upwelling and downwelling temperatures are determined from (4-4) and (4-6). Typical values are 3 K for the upwelling temperature and 6 K for the downwelling temperature. Substitution of the typical values into the sensitivity factors in (4-10) through (4-16) and evaluation of (4-8) yield

$$\varepsilon_{T_A} = \Big[(279\ \Delta e)^2 + (0.36\ \Delta T_S)^2 + (0.63\ \Delta T_{dw})^2 + (\Delta T_{uw})^2 + (2\ \Delta \sec\theta)^2 + (-108\ \Delta\tau_h)^2 + (\Delta C_1)^2 + (\Delta C_2)^2 + (\Delta C_3)^2\Big]^{1/2}. \qquad (4\text{-}17)$$

The errors in the upwelling and downwelling temperatures, ΔT_{uw} and ΔT_{dw}, respectively, are dependent on the errors in the mean atmospheric thermodynamic temperature $\Delta\langle T\rangle_h$, extraterrestrial temperature ΔT_∞, incidence angle $\Delta \sec\theta$, and opacities $\Delta\tau_\infty$, $\Delta\tau_h$, $\Delta\langle\tau\rangle_a$, and $\Delta\langle\tau\rangle_h$. The upwelling temperature error using the same typical parameter values is

$$\Delta T_{uw}^2 = (0.01\ \Delta\langle T\rangle_h)^2 + (-0.03\ \Delta\sec\theta)^2 + (288\ \Delta\tau_h)^2 + (-2.88\ \Delta\langle\tau\rangle_h)^2. \qquad (4\text{-}18)$$

The downwelling temperature error is

$$\Delta T_{dw}^2 = (\Delta T_\infty)^2 + (-0.077\ \Delta\sec\theta)^2 + (0.012\ \Delta\langle T\rangle_a)^2 + (285\ \Delta\tau_\infty)^2 + (-3.46\ \Delta\langle\tau\rangle_a)^2. \qquad (4\text{-}19)$$

The error in the mean atmospheric thermodynamic temperature for the entire atmosphere $\Delta\langle T\rangle_a$ is directly related to the error in the mean atmospheric thermodynamic temperature at altitude and is

$$\Delta\langle T\rangle \doteq \Delta\langle T\rangle_a = \Delta\langle T\rangle_h. \qquad (4\text{-}20)$$

The error in the mean total opacity $\Delta\langle\tau\rangle_a$ and the error in the mean opacity at altitude $\Delta\langle\tau\rangle_h$ are approximately equal and directly related to the error in the opacity, $\Delta\tau_h$ and $\Delta\tau_\infty$. Therefore,

$$\Delta\langle\tau\rangle_h \approx \Delta\langle\tau\rangle_a \approx \Delta\tau_\infty \approx \Delta\tau_h . \tag{4-21}$$

Substitution of (4-18) through (4-21) in (4-17) yields

$$\begin{aligned} \varepsilon_{T_A} = \Big[&(279\ \Delta e)^2 + (0.36\ \Delta T_S)^2 + (0.63\ \Delta T_\infty)^2 \\ &+ (1.92\ \Delta\sec\theta)^2 + (355\ \Delta\tau)^2 + (0.0176\ \Delta\langle T\rangle)^2 \\ &+ (\Delta C_1)^2 + (\Delta C_2)^2 + (\Delta C_3)^2\Big]^{1/2} . \end{aligned} \tag{4-22}$$

In order to achieve an overall accuracy of 0.1 K in the knowledge of the antenna temperature and with nine contributing terms in (4-22), each term must be known to 0.0333. If three terms could be eliminated due to being insignificant, this only improves the error allowance to 0.0408. Assuming nine terms and equal error allowance, the required accuracy for each component is given in Table 4-1.

TABLE 4-1

ERROR BUDGET FOR 0.1 K ACCURACY

Emissivity	0.0001
Surface temperature	0.1 K
Extraterrestrial temperature	0.05 K
Incidence angle	2°
Opacity	0.0001
Mean atmospheric thermodynamic temperature	2 K
Antenna correction	0.03 K
Wind correction	0.03 K
Cloud correction	0.03 K

Table 4-1 gives the accuracy to which each factor in the radiative transfer equation (4-7) must be determined in the simplified algorithm to achieve an overall accuracy of 0.1 K.

The mean atmospheric thermodynamic temperature $\langle T \rangle_h$ at altitude h_r is determined from the arithmetic mean of the surface temperature and the total air temperature measured by the aircraft carrying the radiometer. The mean atmospheric thermodynamic temperature of the total atmosphere $\langle T \rangle_a$ is determined from the arithmetic mean of the surface temperature and the atmospheric temperature at the tropopause. The difference between the exact solution using the numerical integration routines in Appendix B and the method above was less than 1 K for all combinations of water vapor density, scale height, surface temperature, and frequency. Thus, the use of the mean temperatures easily meets the 2 K requirement given in Table 4-1.

The total opacity is the sum of the opacity due to oxygen and water vapor. The opacity as a function of altitude is determined from the sum of each opacity multiplied by an altitude function. The total opacity due to oxygen was obtained by integrating (2-35) using the absorption coefficient determined from (2-37), (2-38), and the 1976 U.S. Standard Atmosphere. The approximation equation developed using regression analysis techniques is a function of frequency and surface temperature and is

$$\tau_{O_2}(\infty,f,T_S) = 1.419 \times 10^{-2} - (2.1 \times 10^{-4})T_S + (1.6 \times 10^{-6})T_S^2 + (1.4 \times 10^{-4})f - (2 \times 10^{-6})fT_S . \tag{4-23}$$

The altitude function for oxygen is

$$\tau_{O_2}(h,f,T_S) = \left[1.-1.03 \exp(-0.2h)\right]\tau_{O_2}(\infty,f,T_S) . \tag{4-24}$$

The total opacity due to water vapor was obtained by integrating (2-35) using the absorption coefficient determined from (2-39), (2-40), (2-41), and the 1976 U.S. Standard Atmosphere. The approximation equation developed using regression analysis techniques is a function of frequency, surface temperature, water vapor density at the surface, and scale height of the water vapor density and is

$$\tau_{wv}(\infty,f,T_S,\rho_w,s_h) = 0.298\rho_w^{1.0269} s_h^{0.392} \left[(1.4 \times 10^{-5}) - (8.66 \times 10^{-6})f + (7.5 \times 10^{-6})f^2 - (5.34 \times 10^{-7})fT_S + (1.6 \times 10^{-6})T_S\right]. \tag{4-25}$$

The altitude function for water vapor is

$$\tau_{wv}(h,f,T_S,\rho_w,s_h) = \left[1. - \exp(-h/s_h)\right] \tau_{wv}(\infty,f,T_S,\rho_w,s_h). \tag{4-26}$$

The total opacity is the sum of (4-23) and (4-25). The opacity as a function of altitude is the sum of (4-24) and (4-26). The upwelling temperature is determined by the following simplifications to (4-4). The mean opacity $\langle \tau \rangle_h$ is 1/2 the opacity at altitude h, and the mean temperature is the average of the measured surface temperature and the aircraft measured atmospheric temperature, TAT. The upwelling temperature is

$$T_{uw} = (1 - 0.5 \sec \theta\tau_h)\tau_h\left(\frac{T_S + TAT}{2}\right). \tag{4-27}$$

The downwelling temperature is obtained from (4-6) and is

$$\begin{aligned} T_{dw} &= (1 - \sec \theta\tau_\infty)T_\infty \\ &\quad + (1 - 0.5 \sec \theta\tau_\infty)\tau_\infty(T_S - 28.25) . \end{aligned} \tag{4-28}$$

The accuracy of the determination of the antenna temperature using the simplified algorithm versus the exact solution given in Appendix B to the radiative transfer equation was investigated. Table 4-2 gives the range of values used in parametrically solving both the exact and approximate radiative transfer equation.

TABLE 4-2

VARIATION IN DEPENDENT VARIABLES

Surface temperature	-5° C to $+25^\circ$ C in 5° C steps
Salinity	0 o/oo and 35 o/oo
Frequency	4 GHz to 8 GHz in 1 GHz steps
Water vapor density	1 g/m^3 to 10 g/m^3 in 1 g/m^3 steps
Scale height	1 km to 5 km in 1 km steps
Altitude	0.3 km to 6 km in 8 steps

Typical remote sensing missions were flown during this research at altitudes between 500 m and 2 km or at 6 km. The typical error between the exact and approximate solution at 500 m was less than 0.02 K. The typical error at 6 km was less than 0.06 K. The maximum error at any combination of dependent variables was less than 0.1 K. Therefore, it can be concluded that the simplified algorithm meets the objective of radiometric antenna temperature calculations to within 0.1 K.

Antenna Pattern Correction

The antenna temperature during the measurement of the radiometric brightness temperature by a radiometer was given in Chapter II by (2-9) and is

$$\hat{T}_A = \frac{\int_\Omega T_B(\Omega)G(\Omega)d\Omega}{\int_\Omega G(\Omega)d\Omega} \tag{4-29}$$

where $\hat{T}_A$ is the antenna temperature measured by an antenna with a power pattern function $G(\Omega)$. Since the antenna usually has a narrow beam, a simplification to (4-29) is to replace $G(\Omega)$ with a delta function. Therefore the antenna temperature is now given by (2-11) and is

$$T_A = T_B(\theta_a, \phi_a) \tag{4-30}$$

where θ_a and ϕ_a are the pointing angles of the infinitely narrow radiometer antenna beam.

The antenna correction factor C_1 is the difference between the true brightness temperature measured by an infinitely narrow beam antenna T_A and the estimated value $\hat{T}_A$ determined by the finite antenna beam. The SFMR antenna was employed as a nadir viewing radiometer during this research and assuming circular symmetry in both the pattern and radiometric surface brightness temperature distribution, the antenna correction factor is

$$C_1 = T_B(0^\circ) - \frac{\int_0^\pi T_B(\theta)G(\theta) \sin\theta \, d\theta}{\int_0^\pi G(\theta) \sin\theta \, d\theta} . \qquad (4\text{-}31)$$

The antenna power pattern $G(\theta)$ has been measured over the frequency range of the SFMR from 4.5 to 7.2 GHz. An example of the antenna power pattern is shown in Fig. 3-5. The variation of brightness temperature with incidence angle $T_B(\theta)$ for a smooth surface can be obtained from the Fresnal reflection coefficients given by (2-74) and (2-75). The antenna correction for the SFMR at 4.8 and 6.0 GHz for measurements of sea surface temperatures of 5° C and 25° C has been computed using (4-31). The results are given in Table 4-3.

TABLE 4-3

ANTENNA CORRECTION FACTOR

Sea surface temperature	Frequency	
	4.8 GHz	6.0 GHz
5° C	0.018 K	0.025 K
25° C	0.019 K	0.027 K

The antenna correction factor for the SFMR as given in Table 4-3 is less than the error allowance given in the error budget for the antenna correction factor (Table 4-1). Therefore, when the SFMR is used as a nadir viewing circular polarized radiometer, the antenna correction factor can be neglected.

Windspeed Correction

The windspeed correction factor, which is required in the measurement of sea surface temperature, is based on an empirically derived correction factor. The increase in brightness temperature for a wind roughened sea is the result of two factors. Below approximately 7 m/s, foam and white caps are not produced and the increase in brightness temperature is entirely due to surface roughness. This increase is approximately a linear function of windspeed with a constant slope. Above 7 m/s, white caps and foam are produced. A significant increase in brightness temperature is observed due to the foam as discussed in Chapter II and illustrated in Fig. 2-9. The increase in brightness temperature is also a linear function of windspeed above 7 m/s, however the slope is significantly greater.

The windspeed correction factor is based on the determination of the correct slope to use below and above a windspeed of 7 m/s. The slope is a function of frequency, increasing with increasing frequency until 10 GHz, then remaining fairly constant for a nadir incidence angle. The slope increases slightly for off nadir incidence angles using horizontal polarization above 10 GHz and decreases slightly for off nadir incidence angles using vertical polarization above 10 GHz (Webster, et al., 1976). The slope is also a function of incidence angle. It is fairly constant from nadir to approximately 40°, then increases for horizontal polarization and decreases for vertical polarization (Hollinger, 1971).

An estimate of the windspeed at the surface is needed to determine the windspeed correction factor in terms of radiometric brightness temperature. The windspeed can be obtained either from the aircraft inertial navigation system (INS) or by direct measurement by a radar scatterometer. The measurement of the radar cross section by the scatterometer can be used to determine the surface roughness and infer the windspeed. The aircraft INS determines the wind at the aircraft's altitude and theoretical models are used to extrapolate these measurements to surface winds.

The windspeed correction factor used during this research is shown in Fig. 4-1. The slope below 7 m/s is 0.2 ± 0.1 K/ms^{-1}. This slope is based on a value measured by Blume, et al. (1977) of 0.18 K/ms^{-1} for

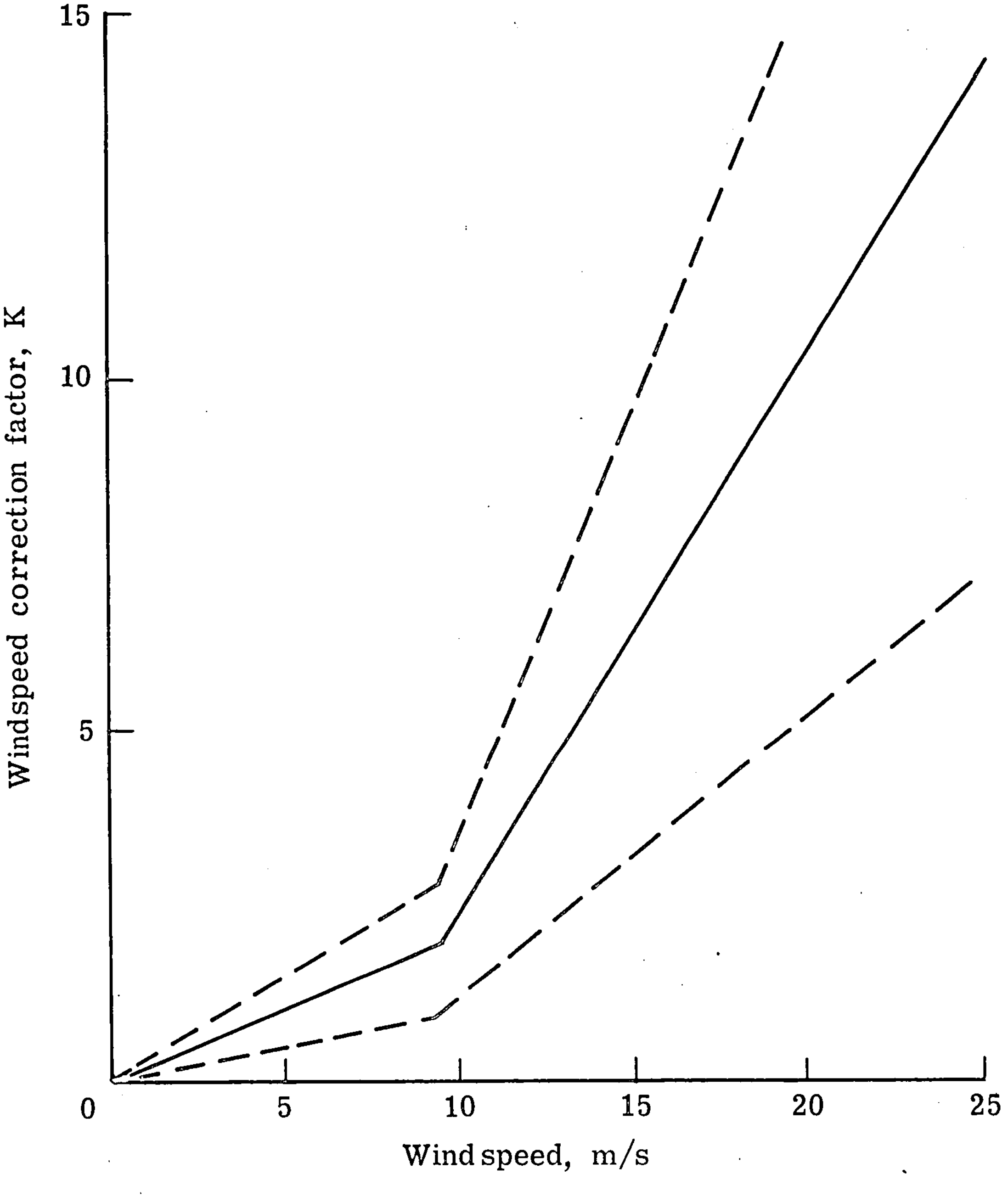

Figure 4-1. Windspeed correction factor.

2.65 GHz at a nadir incidence angle. Also Hollinger (1971) measured a value of 0.2 K/ms^{-1} at 1.41 GHz and 20° incidence angle. The slope above 7 m/s is based on a measurement of 0.54 K/ms^{-1} for vertical polarization and 0.94 K/ms^{-1} for horizontal polarization at 5 GHz and an incidence angle of 38° (Webster, et al., 1976). Since the SFMR is circular polarized and is used at a nadir incidence angle, the two values above were averaged and rounded to 0.8 ± 0.4 K/ms^{-1}.

The windspeed correction factor varies from near 0 K to above 15 K. This correction factor represents the single greatest unknown factor in the accurate determination of sea surface temperature. However, if the wind remains fairly constant, the correction factor should appear as a bias and relative changes in sea surface temperature could be determined. This result will be shown by actual measurements of a strong gradient in sea surface temperature during high winds.

Cloud Correction

The absorption coefficient α_{CL} in nepers per meter for nonprecipitating clouds is a function of the liquid water content of the clouds L, the real and imaginary components of the complex dielectric constant for liquid water at the cloud temperature, the radiometer frequency, and the water density ρ. It can be determined from (2-42) using values of L from the cloud models shown in Fig. 4-2 (Love, et al., 1975). The total absorption is obtained by integrating the absorption coefficient as a function of L and altitude over the range of altitudes for the particular cloud type encountered.

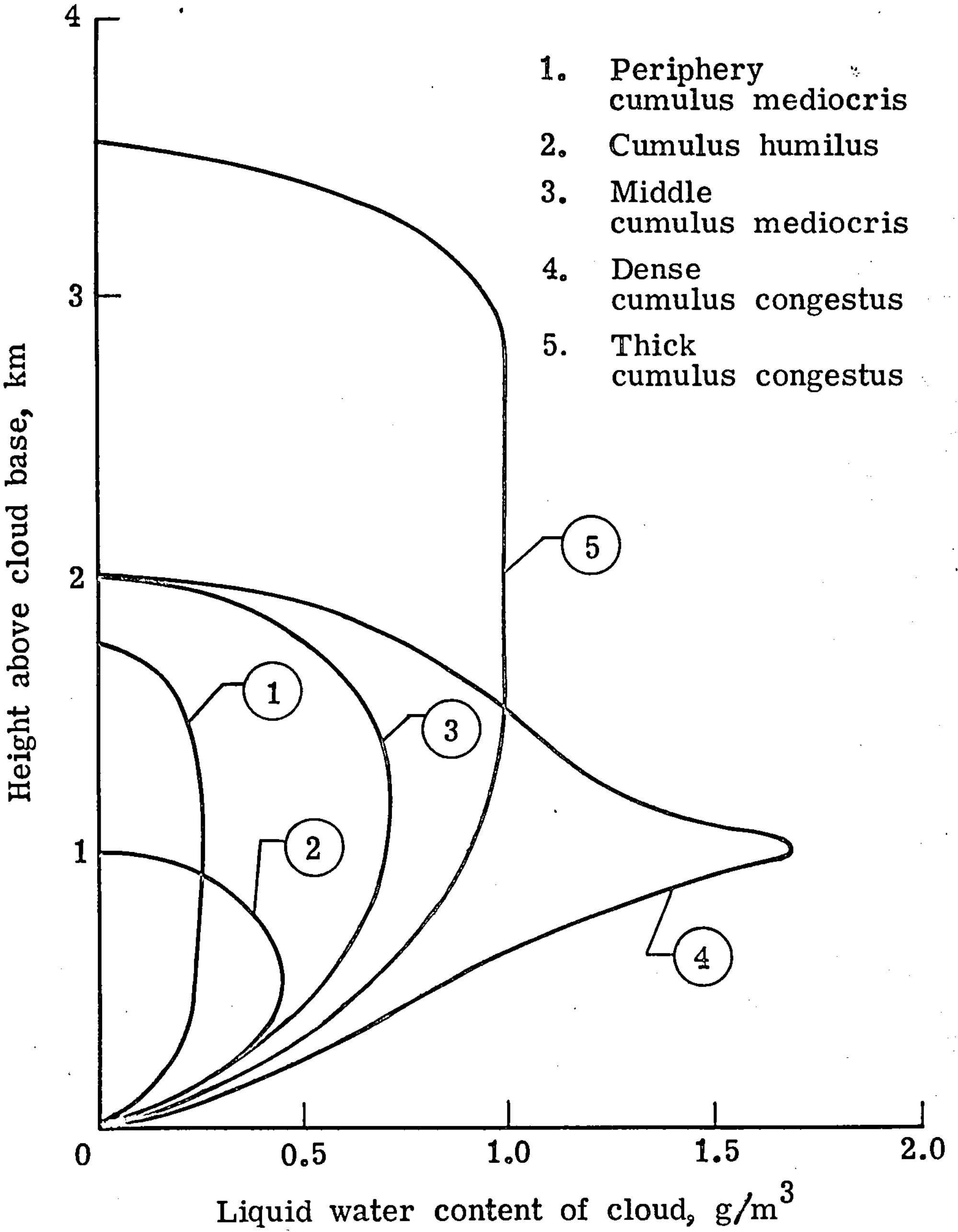

Figure 4-2. Cloud models of liquid water content versus height of cloud above cloud base (Love, et al., 1975).

A total absorption due to the cloud is obtained from

$$a_{CL} = \int_{h_1}^{h_2} \alpha_{CL}(L,z)dz \tag{4-32}$$

where h_1 and h_2 are the altitudes of the base and ceiling of the cloud, respectively. This absorption attenuates the received radiometric brightness temperature along with emitting an electromagnetic radiation proportional to the thermodynamic temperature of the cloud. The antenna temperature when an absorbing cloud is present in the antenna field of view is

$$\hat{T}_A = T_A(1 - a_{CL}) + a_{CL}T_{CL} \tag{4-33}$$

where $\hat{T}_A$ is the measured antenna temperature. Rearranging (4-33), the cloud correction factor is

$$C_3 = \hat{T}_A - T_A = a_{CL}(T_{CL} - T_A) + C_3' \tag{4-34}$$

and is a function of the difference between the cloud thermodynamic temperature and the antenna temperature T_A in the absence of clouds. C_3' is a small correction required due to the effect of the cloud on the reflected downwelling temperature.

The values of a_{CL} for light, moderate, and overcast clouds are given in Table 4-4 for 4, 6, and 8 GHz (Love, et al., 1975).

TABLE 4-4

CLOUD ATTENUATION

Type	Frequency		
	4 GHz	6 GHz	8 GHz
Light	0.9×10^{-3}	2.0×10^{-3}	3.6×10^{-3}
Moderate	4.5×10^{-3}	1.0×10^{-2}	1.6×10^{-2}
Overcast	9.0×10^{-3}	2.0×10^{-2}	3.6×10^{-3}

The cloud correction factor at 6 GHz for a typical sea surface measurement with T_A equal to 110 K and T_{CL} equal to 273 K varies from 0.33 K to 3.3 K for light to overcast clouds. The majority of the remote sensing radiometric measurements made during this research required photographic coverage of the surface. Therefore, the measurements were made below the clouds and the cloud correction factor would consist of a small correction due to the effect of the clouds above the aircraft on the reflected downwelling temperature.

Sea Surface Temperature Inversion Algorithm

The algorithm for determination of sea surface temperature from the SFMR output data is presented in the following steps.

Step 1: Compute the antenna temperature T_A from (3-57) in conjunction with (3-31) and (3-59).

Step 2: Assume a value for the sea surface temperature T_S.

Step 3: (a) Compute τ_h from (4-24) and (4-26).

(b) Compute T_{uw} from (4-27).

(c) Compute τ_∞ from (4-23) and (4-25).

(d) Compute T_{dw} from (4-28).

(e) Compute e from (2-29) and (2-74) through (2-76).

(f) Determine correction factors C_1, C_2, and C_3.

(g) Compute an estimated $\hat{T}_A$ from (4-7).

Step 4: If $\hat{T}_A$ is within an acceptable error band of T_A, then T_S is a reasonable estimate of the sea surface temperature. If the error band is not acceptable, return to step 2, assume a new value of T_S, and repeat steps 3 and 4.

The determination of surface temperatures for ice or any other geophysical type of surface can be accomplished by using the emissivity for that surface in step 3(e) above. If the surface temperature is independently measured, an estimate of the emissivity can be obtained by interchanging emissivity and surface temperature in the algorithm. Determination of other geophysical parameters of interest can be made from the estimate of emissivity.

CHAPTER V

AIRCRAFT REMOTE SENSING RESULTS

Radiometric Mapping of an Ocean Polar Front

The development of a radiometer with the capability of accurately measuring sea surface temperature was an objective of this research. Although the inversion from radiometric brightness temperature to thermodynamic sea surface temperature for the stepped frequency microwave radiometer (SFMR) has not been accomplished, this has been accomplished for earlier radiometers (Blume, et al., 1978). When the inversion algorithm is completed, the accomplishment of this objective will have been demonstrated by the radiometric mapping of an ocean polar front near Bear Island in the Barents Sea. The location of this region between Norway and Svalbard is shown in Fig. 5-1. These measurements were made during the Norwegian Remote Sensing Experiment (NORSEX) which was conducted in the Fall of 1979. The overall objective of NORSEX was to investigate the ice-ocean dynamics in the marginal ice zone with particular attention focused on some related problems. One of these problems was to evaluate the capability of passive microwave systems (radiometers) to detect ocean frontal characteristics. This permanent ocean frontal system is formed by the warm and saline Atlantic water flowing into the Barents Sea and interacting with the outflowing cold and less saline arctic water (Johannessen and Foster, 1978).

The stepped frequency microwave radiometer (SFMR) was installed in a nadir viewing location on the National Aeronautics and Space Administration (NASA) C-130 "Earth Survey 2" along with an array of other remote

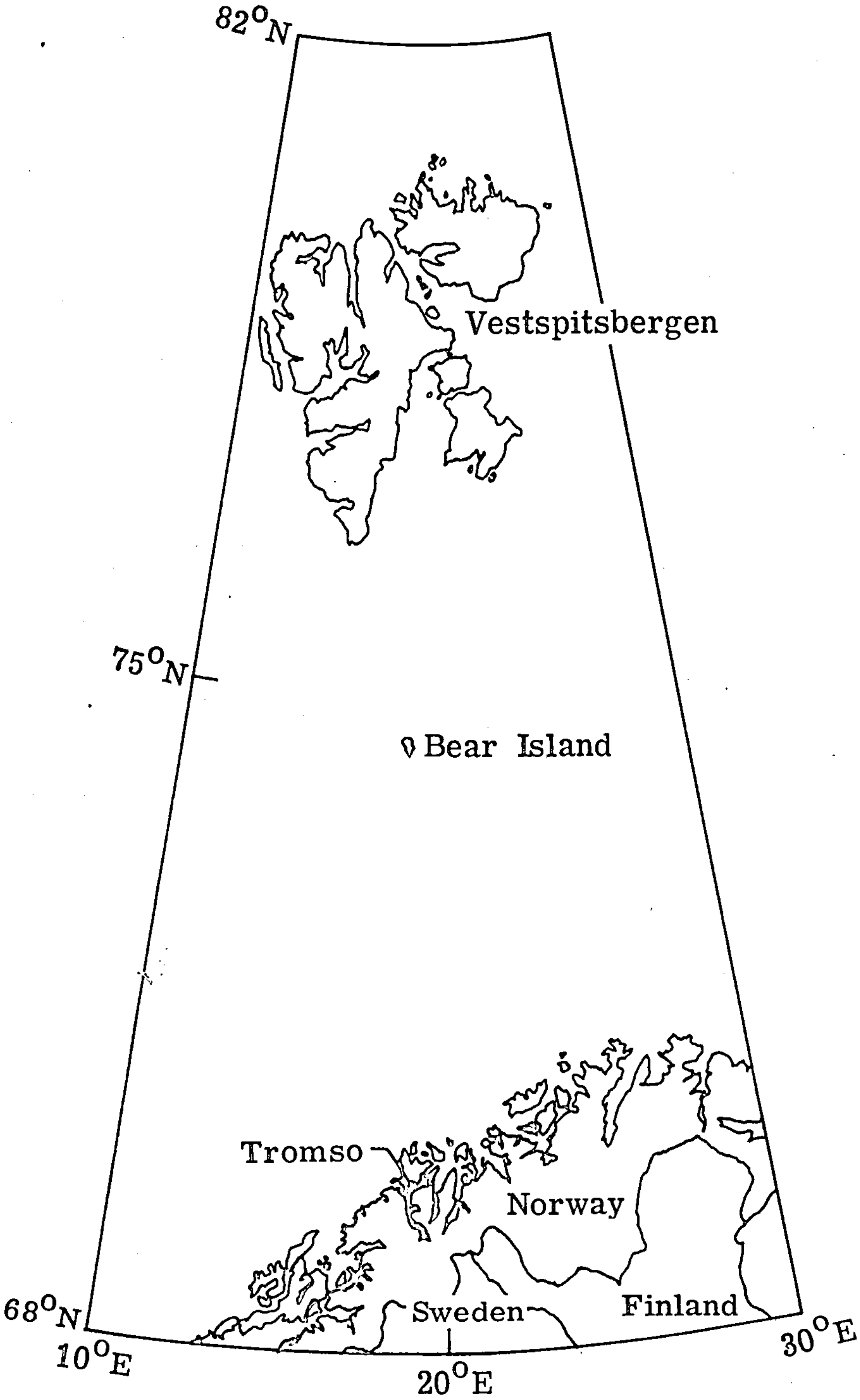

Figure 5-1. Location of the polar front region near Bear Island in the Barents Sea.

sensing instruments. An infrared radiometer (PRT-5) was used to measure surface temperature, and an aerial camera provided surface photographs during clear weather. The mapping of the polar front was accomplished between latitudes 73°30'N and 75°00'N and longitudes 18°40'E and 21°40'E. Four north south transects along 18°40'E, 19°40'E, 20°40'E, and 21°40'E were flown by the NASA C-130. "In-situ" measurements of the sea surface temperature were made by Airborne Expendable Bathythermographs (AXBT's) dropped by a Norwegian Navy P-3 on October 5, 1979. The results of the AXBT measurements are shown in Fig. 5-2. The dots indicate the AXBT drop locations. Contours of sea surface temperatures spaced every 0.5° C between 2.5° C and 7° C have been generated from the AXBT measurements and are shown in Fig. 5-2.

The sea surface temperature along the north south transect at 20°40'E longitude was continuously measured by the Norwegian ice breaker Polarsirkel on October 5, 1979. These measurements are shown in Fig. 5-3 along with the AXBT measurements at the 20°40'E longitude. The indicated gradient in sea surface temperature, which is the indication of the polar front, occurred between latitudes 74°10'N and 74°20'N on October 5. The NASA C-130 mapped the polar front on October 8, 1979. The sea surface temperature measured by the infrared radiometer, sea surface temperature obtained from the radiometric brightness temperature, and the radiometric brightness temperature obtained from the SFMR are shown in Fig. 5-3. This figure shows that between October 5 and October 8, the gradient has moved south and lies between 74°0'N and 74°10'N. The two peaks in the radiometric brightness temperature

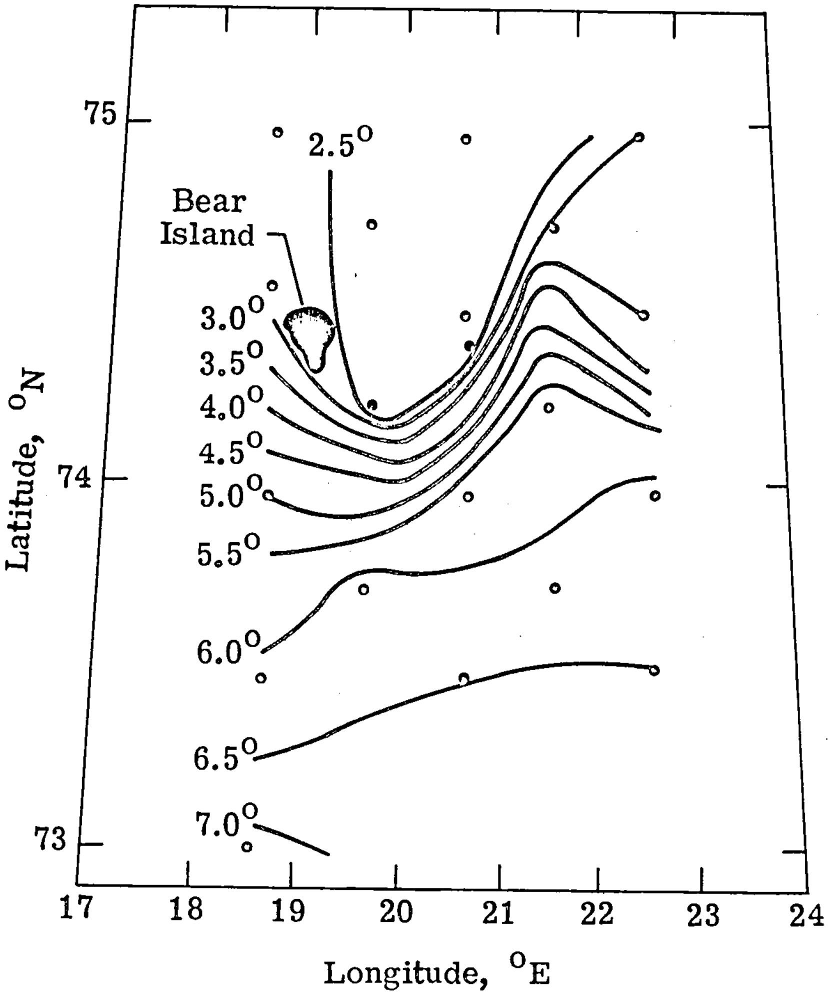

Figure 5-2. Synoptic sea surface temperature on October 5, 1979 in the Bear Island region as observed by Airborne Expendable Bathythermograph (AXBT). (Dots indicate drop sites.)

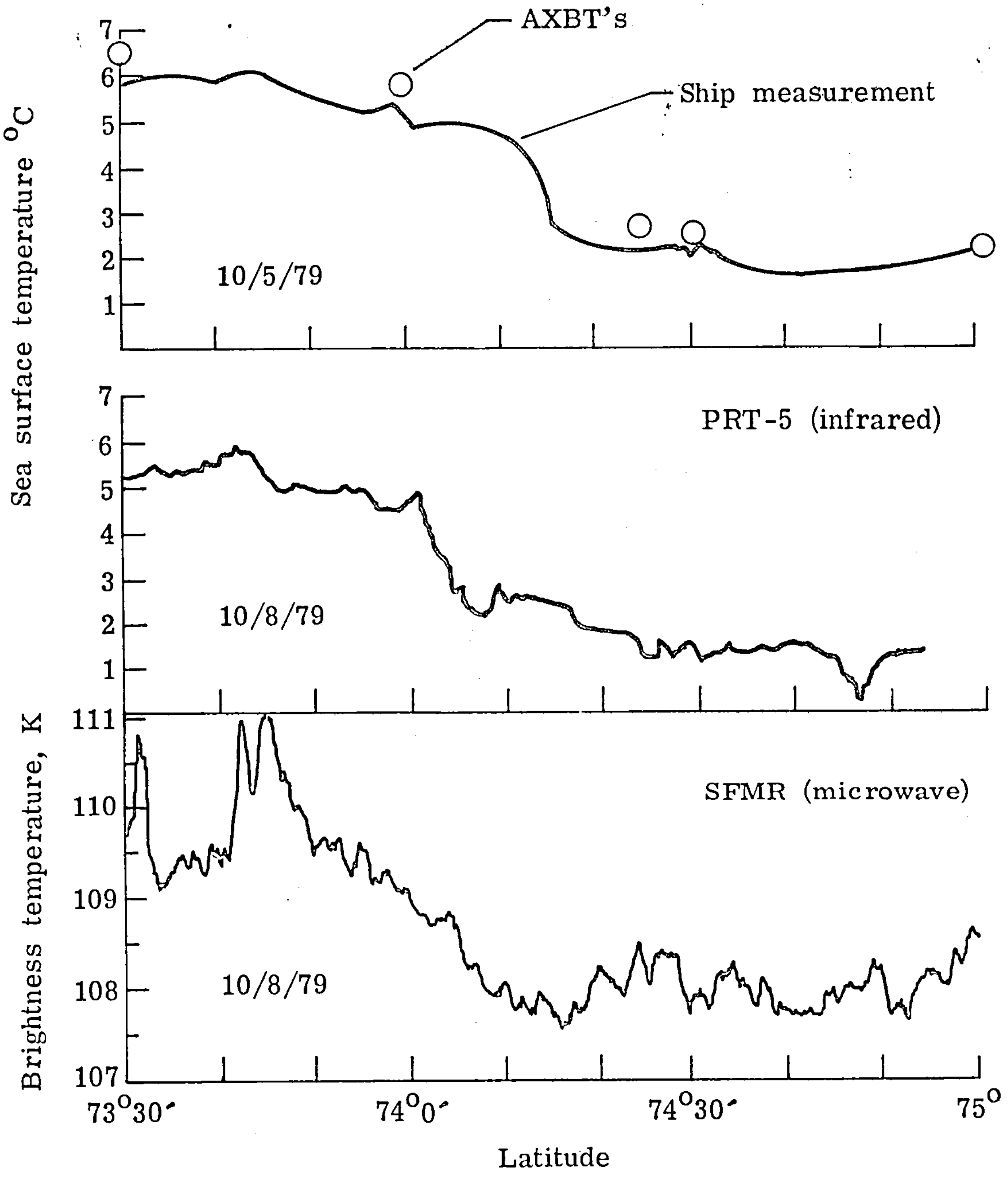

Figure 5-3. Aircraft remote sensing observations on October 8, 1979 of the sea surface variations of microwave brightness temperature, sea surface thermodynamic temperature measured by the aircraft infrared radiometer, and "in-situ" thermodynamic temperature measured by a surface vessel on October 5, 1979 along the north south transect across the Barents Sea ocean front.

located between 73°40'N and 73°45'N latitude are the result of two rain cells located between the aircraft and the surface. The smaller variations are due to the variation in the density of white caps and foam on the sea surface within the radiometer antenna field of view. These conclusions were confirmed through analysis of the aerial photographs.

The radiometric brightness temperature measurements along the four north south transects flown on October 8, 1979 are shown in Fig. 5-4. The synoptic sea surface temperature derived from AXBT's is shown in Fig. 5-2. The temperatures decreased from 6° C to 3° C along 18°40', and from 6° C to 2.5° C along 19°40' and 20°40'. This 3° C to 3.5° C decrease in sea surface temperature should cause a corresponding 0.75 K to 0.79 K decrease in radiometric brightness temperature as computed from (4-7). The actual change in radiometric brightness temperature decreased 2.5 K along 18°40', 4.5 K along 19°40', 2 K along 20°40', and 3 K along 21°40'. The difference is most likely due to brightness temperature biasses induced by variations in wind stress.

This research has shown that a passive microwave radiometer can detect ocean frontal systems. Further investigations are in progress to correct for the wind bias in order to provide more quantitative results.

Ice Thickness Measurements

Another objective of this research was to develop a radiometer capable of measuring ice thickness. Two techniques of measuring ice thickness were discussed in Chapter II. The first technique employed the frequency stepping capability of the SFMR to provide a method based on observing the characteristic Fabry-Perot interference fringes of an ice-water layered dielectric media. However, when the surface is rough,

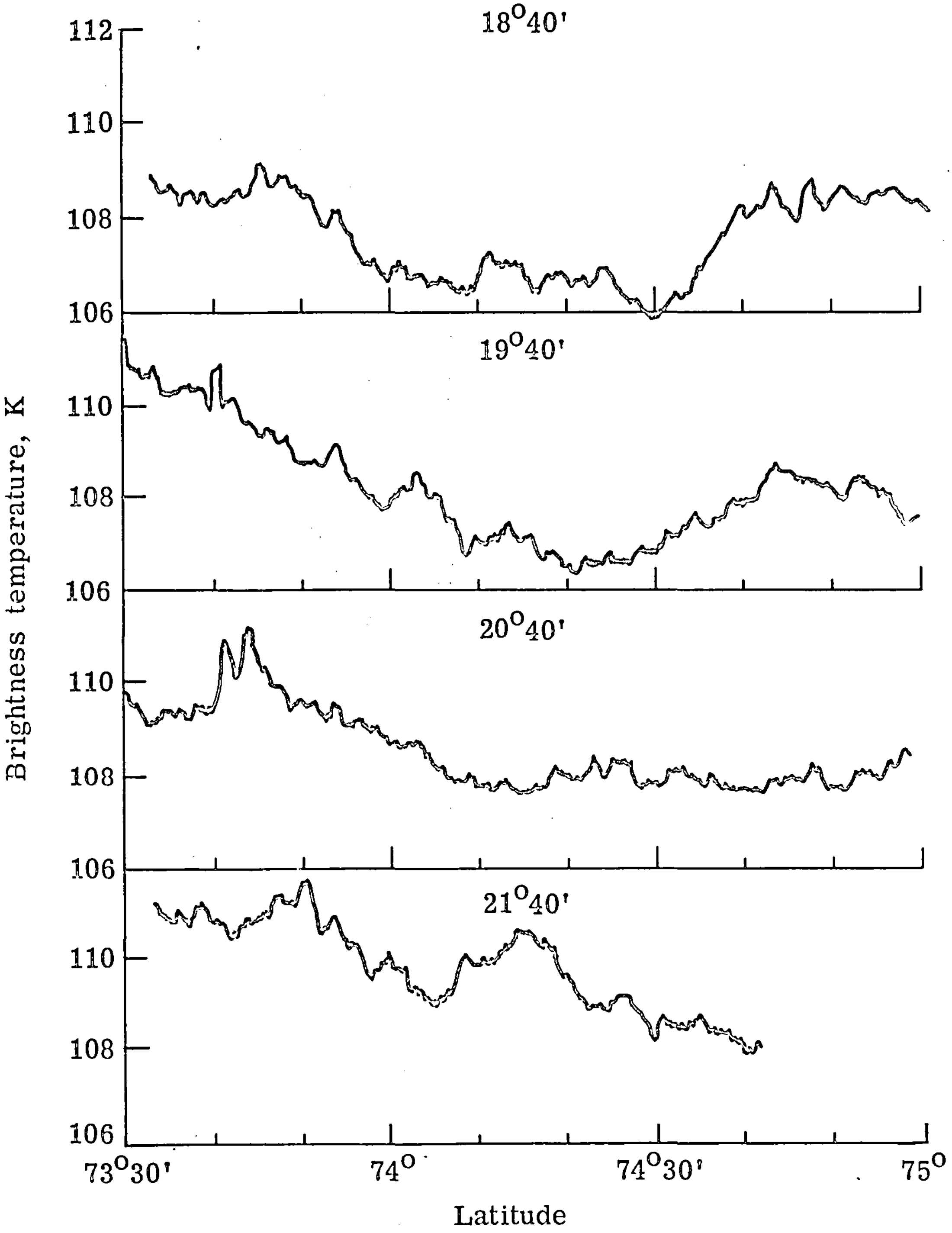

Figure 5-4. Sea surface radiometric brightness temperature on October 8, 1979 along four north south transects across the Barents Sea ocean front.

or the ice has a high loss tangent, the Fabry-Perot resonances are damped out. When this occurs, the resulting radiometric brightness temperature response is a monotonically increasing function of the total attenuation of the ice layer. Since the attenuation coefficient can be determined for lake ice from an independent measurement of surface temperature, the radiometric brightness temperature is a direct function of the ice thickness.

The first reported measurement of lake ice thickness utilizing SFMR was made from the NASA C-130 over Lake Erie on March 9, 1978 (Swift, et al., 1980). These measurements confirmed the capability of the SFMR to determine thickness by measuring the total attenuation. A more extensive aircraft remote sensing measurement of lake ice was subsequently performed over Lake Michigan by the NASA C-130 on March 10, 1979. The objective of this experiment was to evaluate active and passive microwave techniques for identification of ice coverage, clear water passages, pressure ridges, and ice thickness.

The 1979 Great Lakes experiment consisted of mapping the radiometric brightness temperature of the Mackinac Straits in Lake Michigan using the SFMR. The location of the test area and the flight lines are shown in Fig. 5-5. The SFMR was installed in a nadir viewing location on the NACA C-130 along with an infrared radiometer, an aerial camera for surface photography, and other remote sensing instruments. A Coast Guard helicopter was used to land personnel on the ice to make "in-situ" ground truth measurements of ice thickness. The locations of the ground truth measurements are also shown in Fig. 5-5. Eight east west transects were

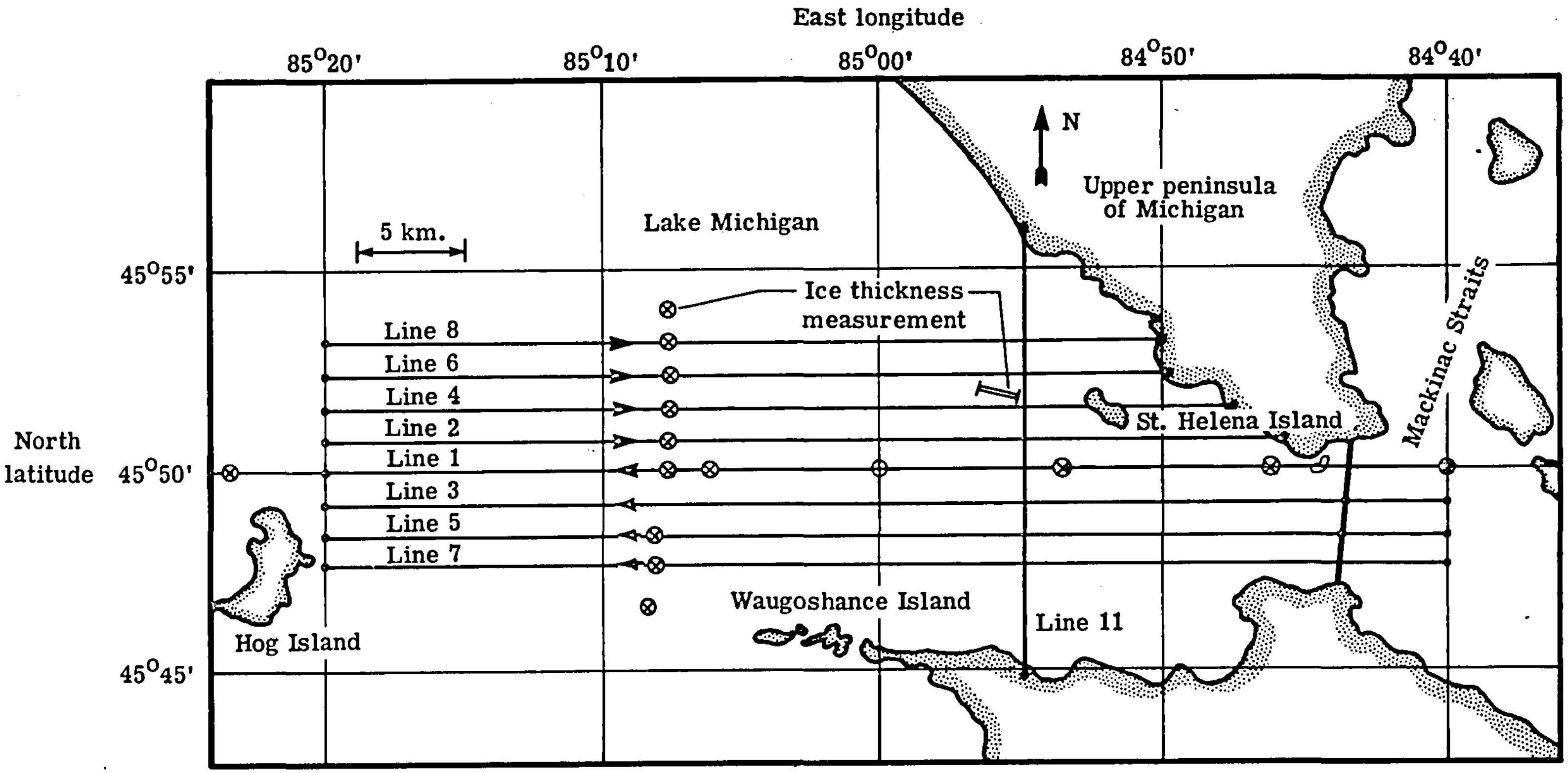

Figure 5-5. Location of the lake ice measurements conducted in Mackinac Straits, Lake Michigan, showing flight lines and location of ground truth measurements.

flown between longitudes 84°40'W and 85°20'W. One north south transect which crossed all eight east west transects was flown along longitude 84°55'W.

The radiometric brightness temperature for line 2 is shown in Fig. 5-6. The radiometric brightness temperature for the lake ice varied from 202 K to 238 K. The peak at 84°45'W of 256 K is land. When the radiometric brightness temperature is less than 210 K, the ice was smooth or consisted of very small rubble. Values between 210 K and 220 K represented either ice rubble, pressure ridges, or rough ice surfaces. The measurement of 230 K at 84°57'W was the signature of a refrozen ship's lead. The peaks at 85°10'W result from rubble piles located at White Shoals Light.

A detailed comparison between the increase in radiometric brightness temperature due to base ice caused by ice rubble which has been built up in the shallow water at White Shoals is shown in Fig. 5-7. The peak at 85°08'W to approximately 240 K is a result of the increase in effective ice thickness due to rubble over White Shoals. An aerial photograph with the ground track of the aircraft is shown in Fig. 5-7. The radiometric brightness temperature as measured by the SFMR is plotted beneath the aerial photograph.

The radiometric brightness temperature for line 4 is shown in Fig. 5-8. The measurements at 84°49'W and between 84°56'W and 85°W longitudes of 198 K to 200 K represent smooth ice which is thinner than the ice measured on line 2. The large response rising to 255 K at the eastern end of line 4 is due to St. Helena Island and the upper

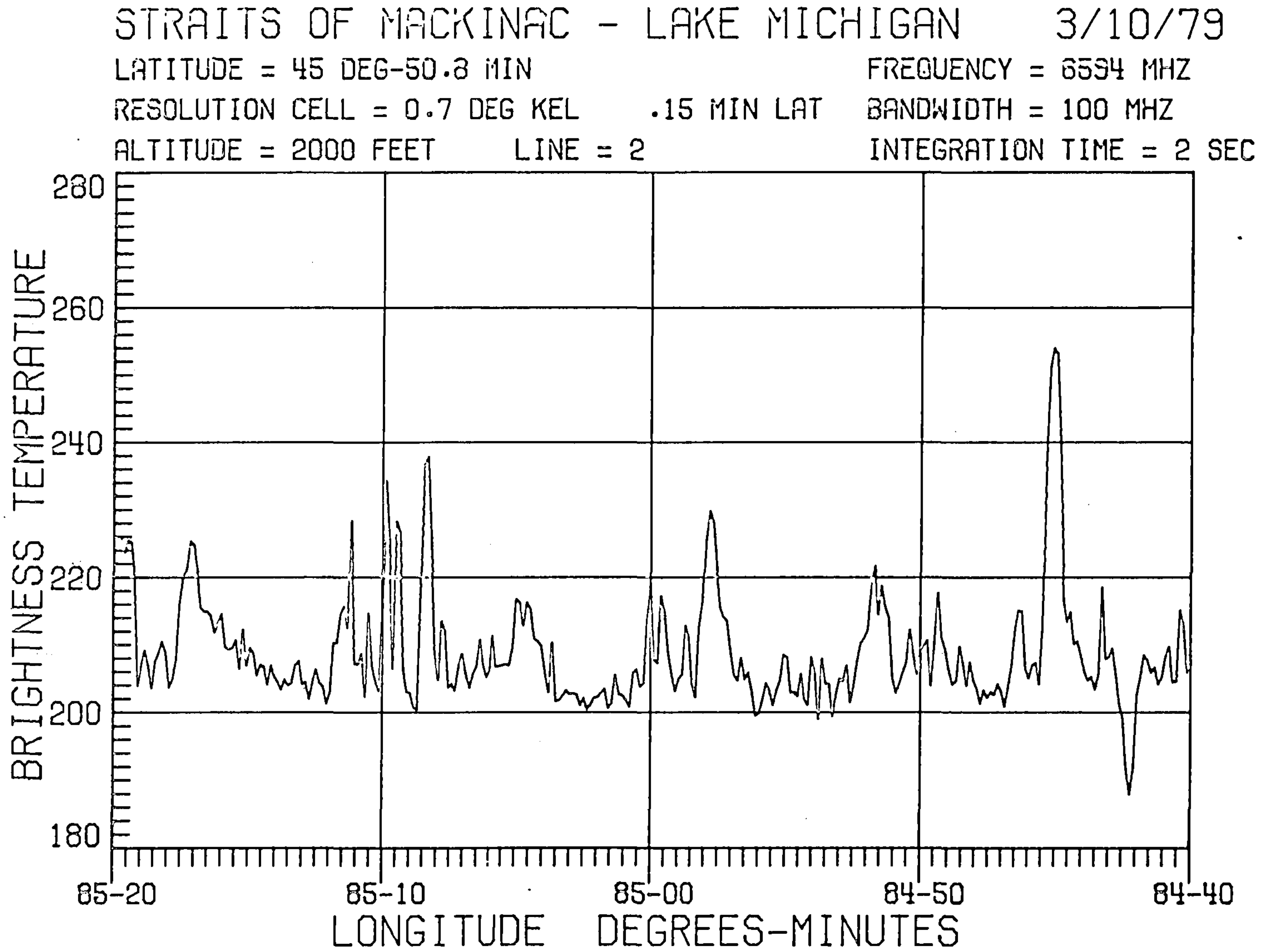

Figure 5-6. Radiometric brightness temperature of lake ice versus longitude for line 2.

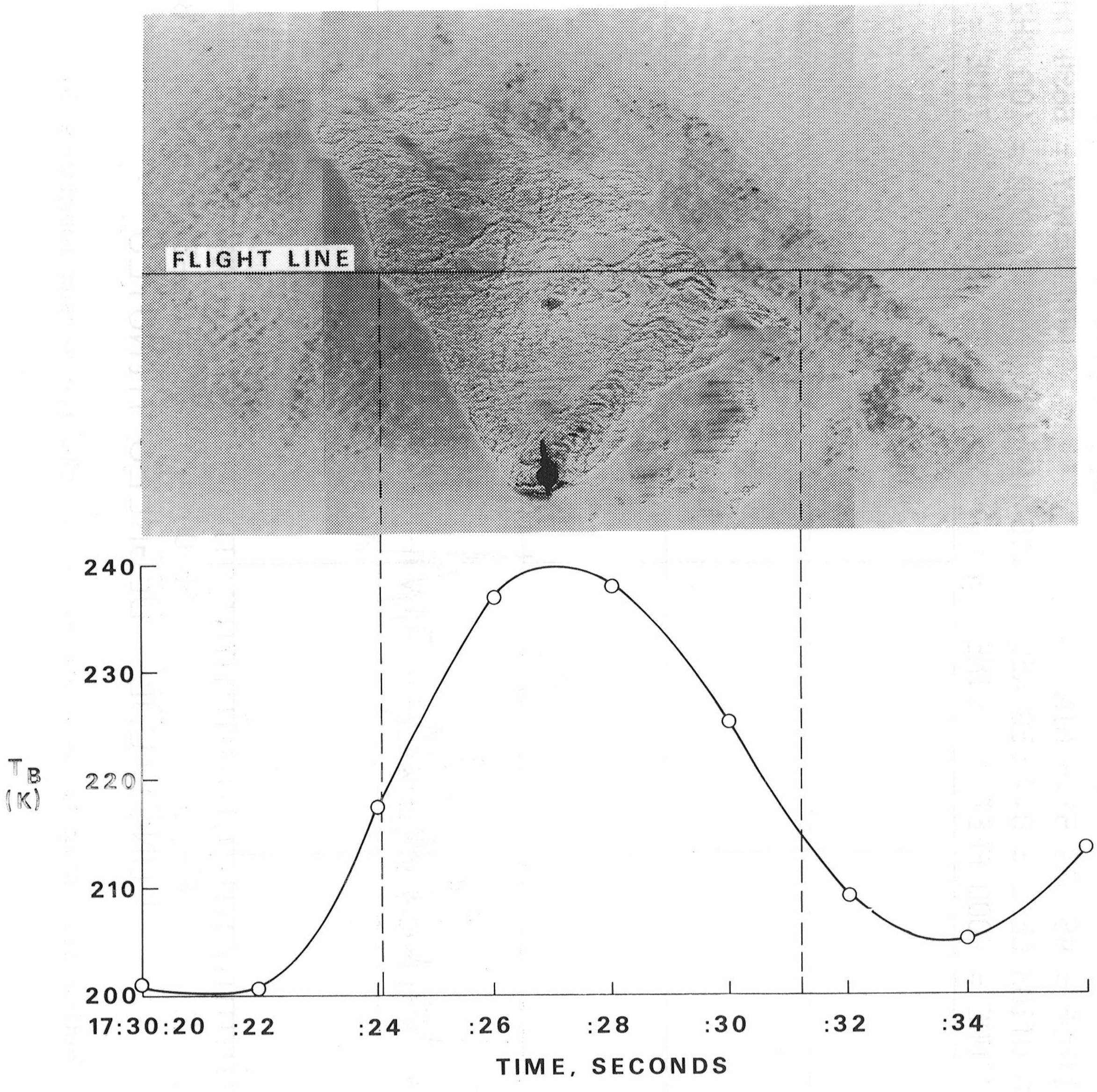

Figure 5-7. Radiometric brightness temperature of lake ice at White Shoal Light on line 2.

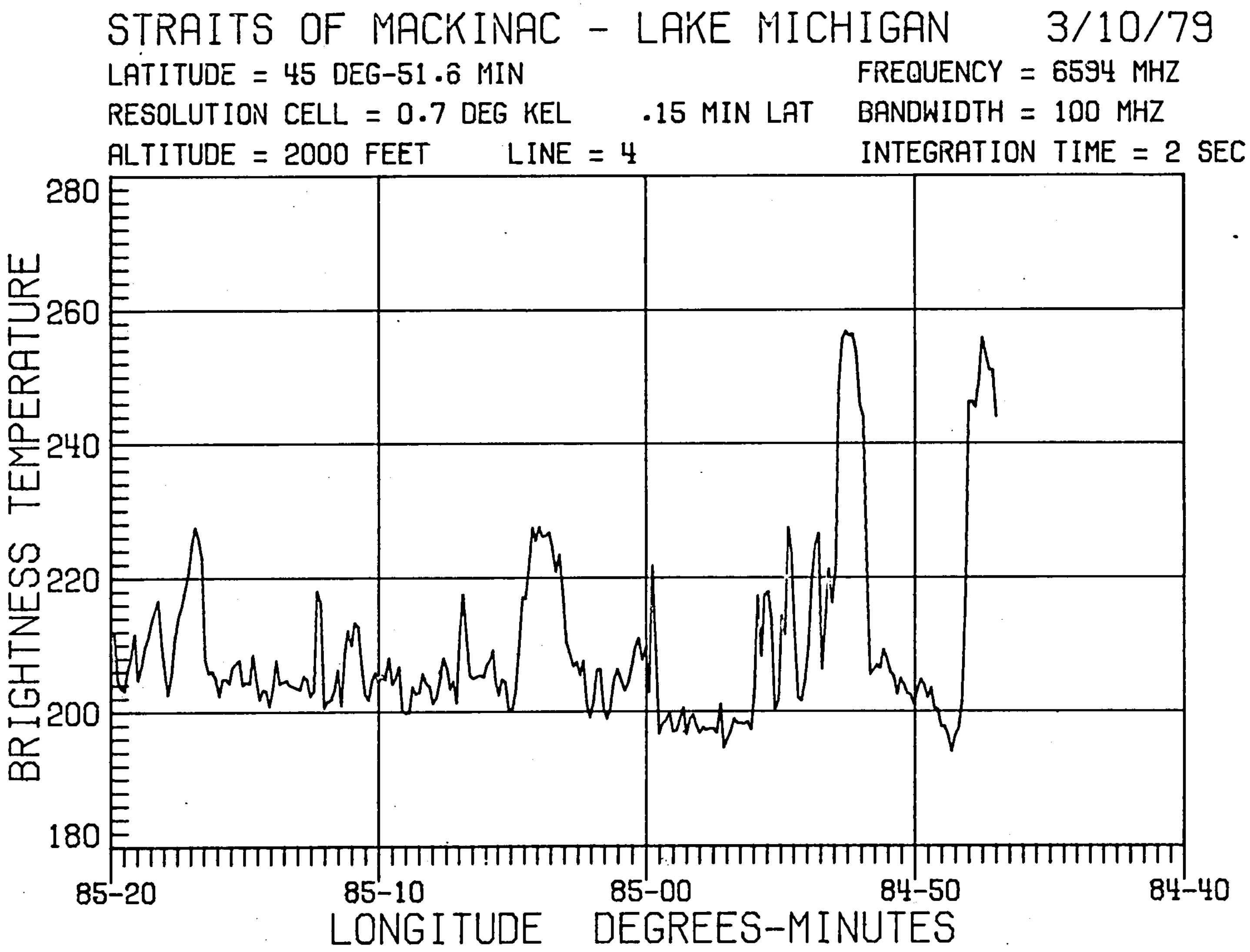

Figure 5-8. Radiometric brightness temperature of lake ice versus longitude for line 4.

peninsula of Michigan. The peaks between St. Helena and the smooth ice near 85°W are rubble piles. The 228 K measurement at 85°04'W was a refrozen ship's lead which went along the aircraft ground track for a short time period.

The thickness of the ice in a section between 84°55'W and 84°59'W along line 4, shown in Fig. 5-8, was computed from the measured radiometric brightness temperature of 198 K. The thickness was calculated to be 60 cm using (2-85) assuming an absorption coefficient of 2.5 dB/m for fresh water ice. Measurement of the ice thickness made by observers on the ice showed an average thickness in this region of 60 cm.

The stability and repeatability of the SFMR is demonstrated in Fig. 5-9. The east west lines 1, 2, 3, and 4 were flown between 12:09 PM and 12:54 PM. The aircraft inertial navigation system (INS) failed, which required the aircraft to land for maintenance. While the INS was being replaced with a spare unit, all instruments had to be turned off. After the INS replacement, lines 5, 6, 7, and 8 were flown between 3:24 PM and 4:42 PM. After line 8 was completed, the north south transect, line 11, was flown. The measurements deduced from lines 1 through 8 are plotted along with the radiometric brightness temperature measured by the SFMR along line 11. This combined plot is shown in Fig. 5-9. No bias adjustments nor changes in calibration were required, which illustrates the stability of the instrument.

The measurement of lake ice thickness has been demonstrated using the total attenuation technique. However, the detection of Fabry-Perot interference fringes was not observed during the 1979 Great Lakes

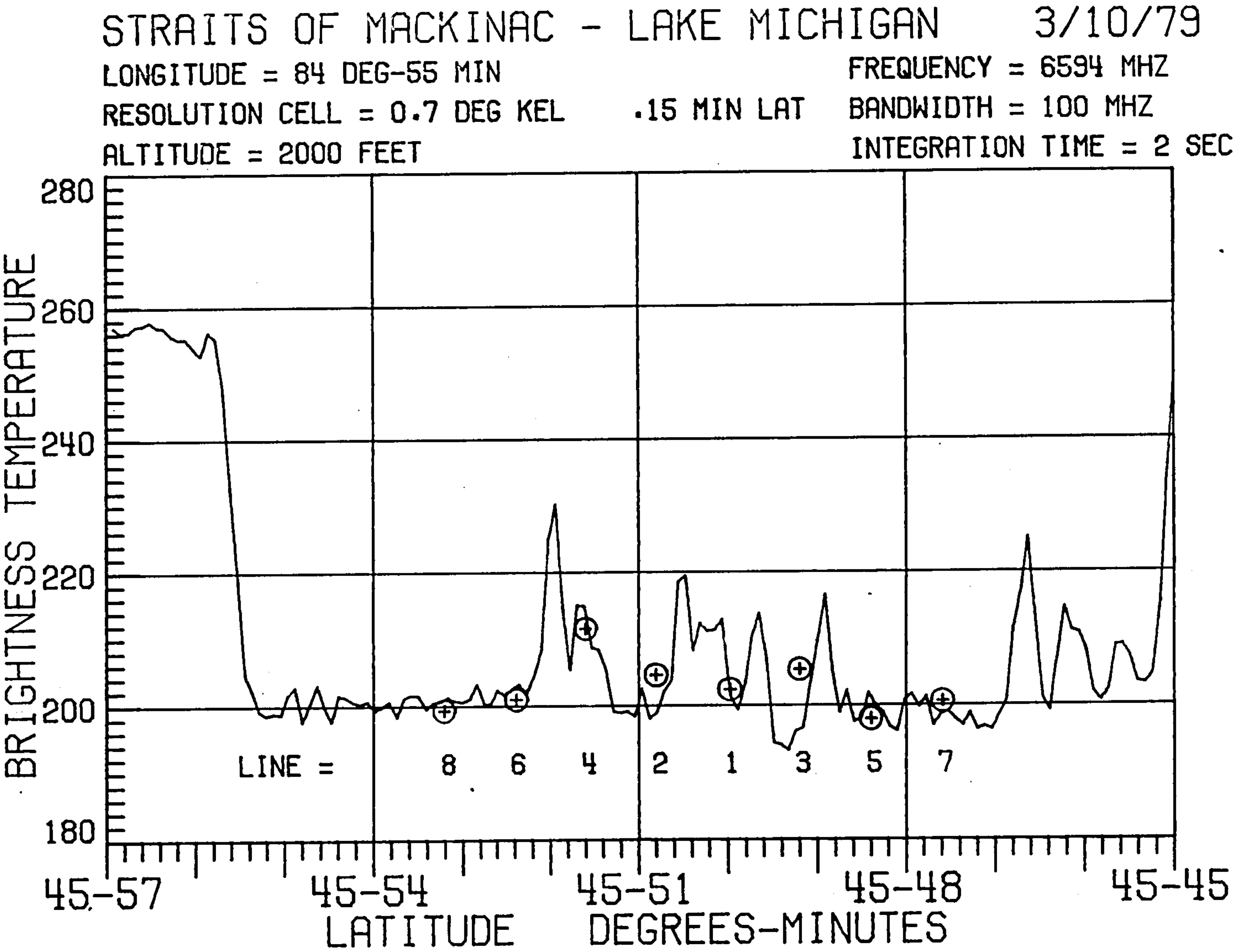

Figure 5-9. Radiometric brightness temperature of lake ice versus latitude during north-south transect of lines 1 through 8.

experiment due to excessive roughness of the region as a result of winter shipping traffic.

Quarter wavelength oscillations due to the Fabry-Perot interference fringes were observed during a functional check flight for the SFMR on the NASA C-130. This flight was flown over thin smooth ice on Claytor Lake in Western Virginia on March 7, 1978. The SFMR was scanning over five frequencies from 5000 MHz to 5288 MHz. Because of the small size of the lake and the short time for measurement due to aircraft limitations, insufficient data were obtained for quantitative measurements of the Fabry-Perot interference fringes. However, the presence of the interference fringes was confirmed.

Sea Ice Measurements

An objective of this research was to develop a microwave radiometer with a capability to determine sea ice type and sea ice thickness. To evaluate the ability of the SFMR to meet these objectives, the instrument was flown in a nadir viewing configuration on the NASA C-130 during the Sea Ice Radar Experiment (SIRE). This experiment was conducted in March 1979. The objectives of SIRE were to determine the interactions and to develop correlations between active and passive all weather sensors and ice phenomena, both surface and subsurface, associated with commercial applications in the Arctic. Long range goals are to determine and characterize remote sensing techniques and sensor combinations capable of measuring ice properties at the necessary temporal and spatial frequencies.

Measurements of sea ice type and thickness were made on March 20, 1979 in an area north of Prudhoe Bay in the Beaufort Sea. This area is located between latitudes 71°45'N and 71°55'N and longitudes 145°W to 146°W and is shown in Fig. 5-10. The capability to distinguish between first year and multiyear ice had not been accomplished by radiometers operating below 10 GHz prior to the measurements on March 20. This was primarily due to the insufficient accuracy and stability of previous radiometers to perform these measurements. Multiyear ice, which is thicker and less saline than first year ice, is defined as ice which has survived one or more summer melt seasons. It appears weathered and may have refrozen melt ponds. An example of an isolated piece of multiyear ice embedded in first year ice is shown in Fig. 5-11. The SFMR antenna footprint is approximately equal to this piece of multiyear ice, and the instrument was therefore able to discriminate it from the surrounding first year ice. The SFMR measured a radiometric brightness temperature of approximately 226 K for this isolated piece of multiyear ice, as compared with a radiometric brightness temperature of 232 K for the surrounding first year ice.

A large area of all multiyear ice is shown in Fig. 5-12. Refrozen melt ponds and the weathered appearance of multiyear ice are clearly evident in this photograph. The NASA C-130 made several measurement runs across this large area of multiyear ice at an altitude of 330 m.

The radiometric brightness temperature of the sea ice at a frequency of 7.2 GHz and integration time of 0.5 s is shown in Fig. 5-13. The large section of multiyear ice shown in Fig. 5-12 exhibited a

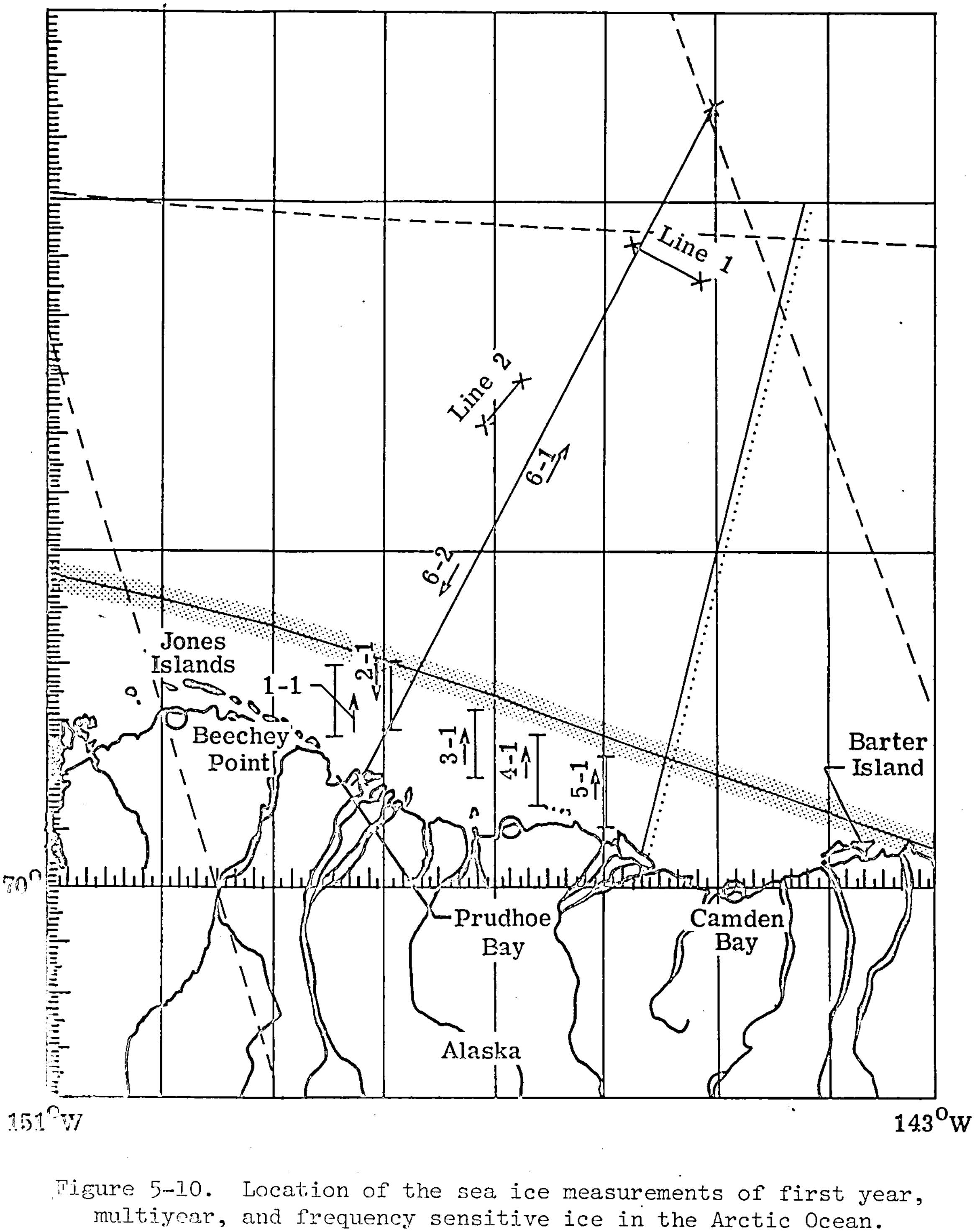

Figure 5-10. Location of the sea ice measurements of first year, multiyear, and frequency sensitive ice in the Arctic Ocean.

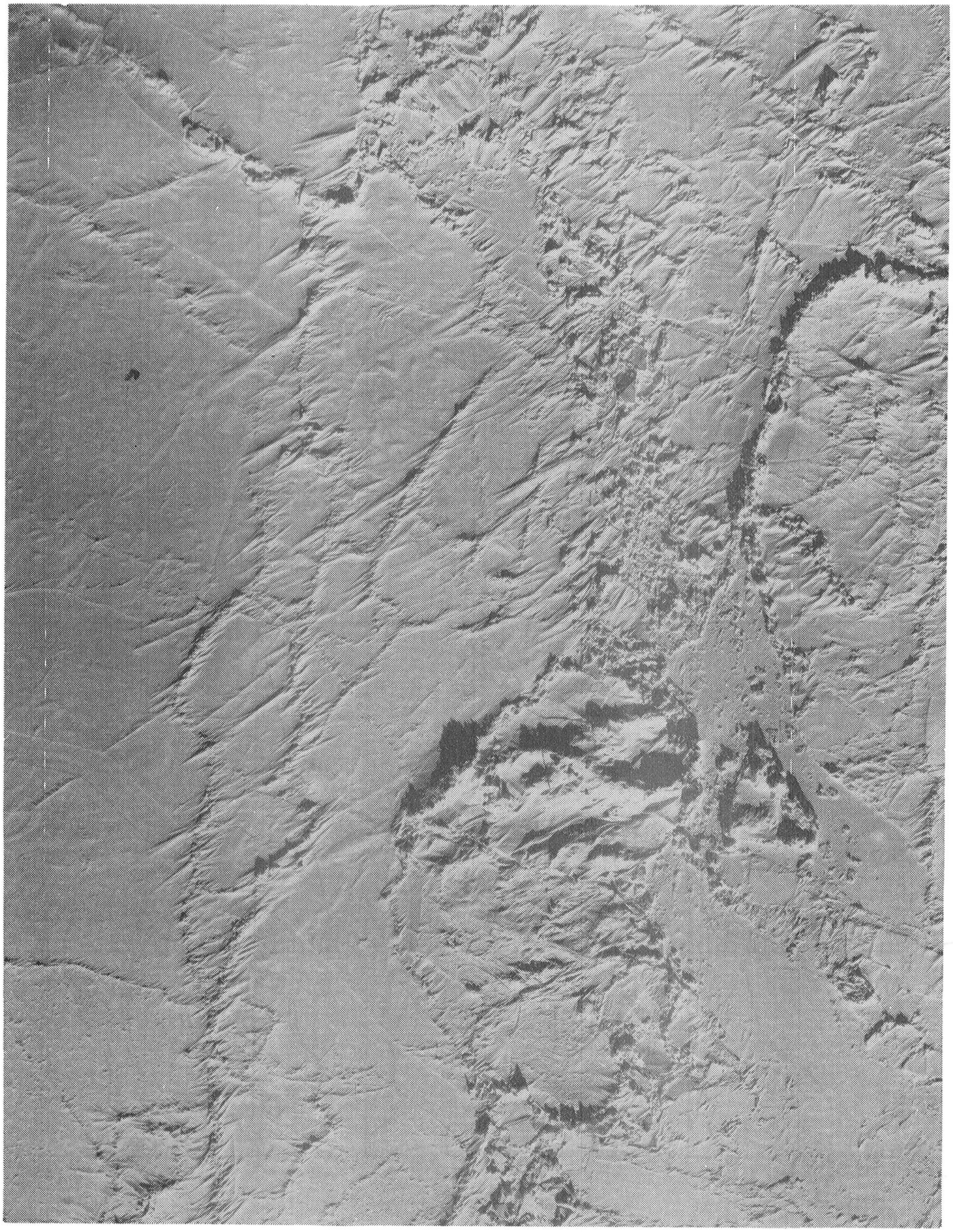

Figure 5-11. Aerial photograph of an isolated piece of multiyear ice embedded in first year ice along line 1 in Fig. 5-10.

Figure 5-12. Aerial photograph of multiyear ice along line 1 in Fig. 5-10.

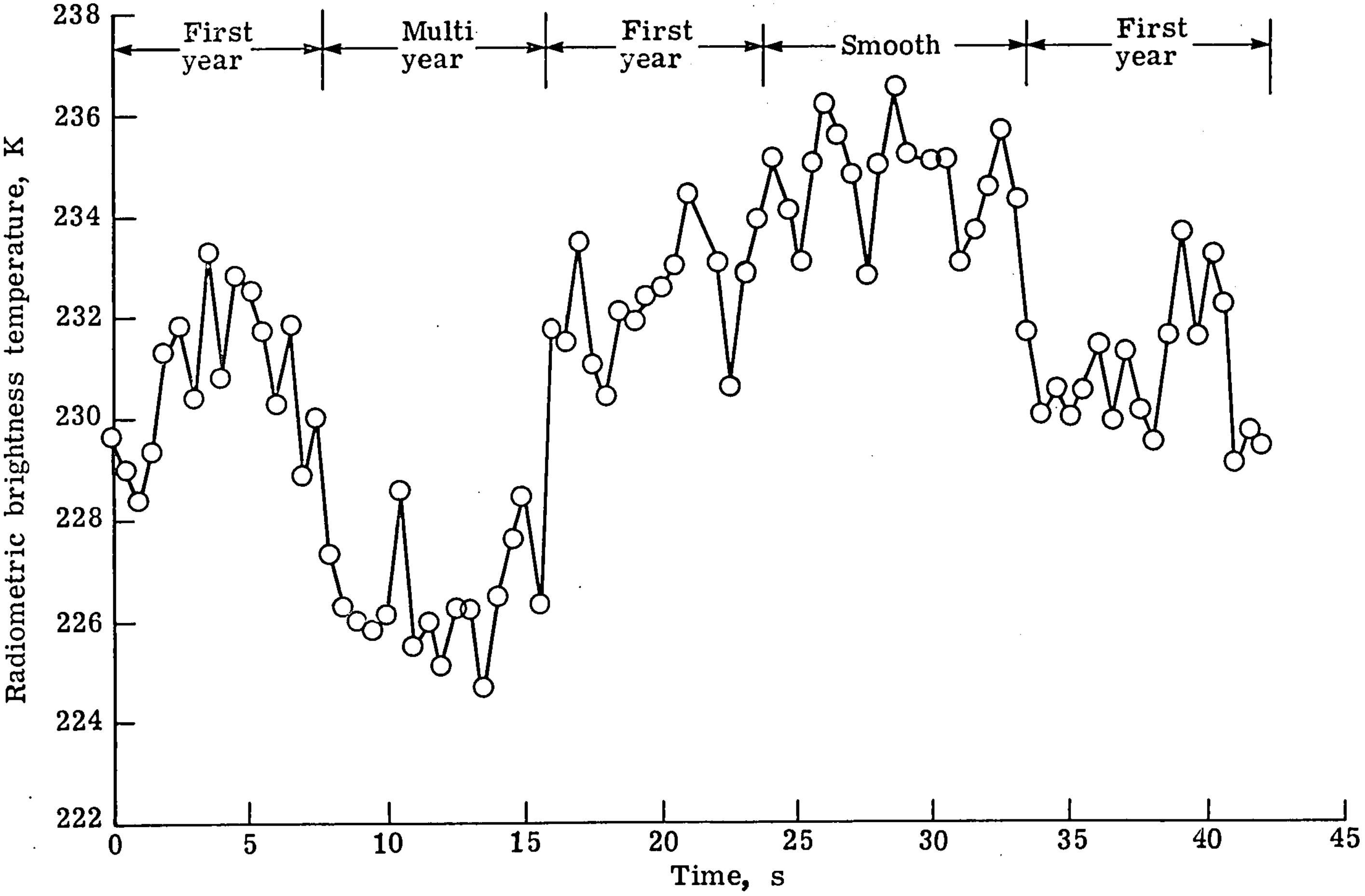

Figure 5-13. Radiometric brightness temperature of sea ice versus time for run 8 at a frequency of 7.2 GHz and an integration time of 0.5 s.

radiometric brightness temperature of approximately 226 K. The first year ice on either side of the multiyear ice indicated a radiometric brightness temperature between 231 K and 232 K. The smooth first year ice had a radiometric brightness temperature of 235 K. These measurements were made during run 8 along line 1 between a point located at latitude 71°45'N, longitude 145°10'W and a point located at latitude 71°52'N, longitude 145°45'W.

Figure 5-14 shows the radiometric brightness temperature during run 6 along line 1 (same coordinates as Fig. 5-13). The SFMR frequency was alternating between 5.6 GHz and 6.6 GHz every 0.5 s during this run. The radiometric brightness temperature for the large area of multiyear ice at 5.6 GHz and 6.6 GHz was between 225 K and 228 K. This is approximately the same for the 7.2 GHz. The measurement of first year ice for 5.6 GHz and 6.6 GHz resulted in a radiometric brightness temperature between 231 K and 234 K. This also agrees with the measurement at 7.2 GHz. The measured radiometric brightness temperatures of 226 K at 18 s and 224 K at 49 s for a frequency of 6.6 GHz are isolated chunks of multiyear ice as shown in Fig. 5-11. The measurement of 223 K at 52 s for a frequency of 5.6 GHz also was that of an isolated chunk of multiyear ice.

The measurement of the smooth ice portion of line 1 shown in Fig. 5-13 for 7.2 GHz and Fig. 5-14 for 5.6 GHz and 6.6 GHz shows evidence of quarter wavelength oscillations due to the Fabry-Perot interference fringes. These would be indicative of ice thickness measurements as discussed in Chapter II. The measurement at 5.6 GHz varied

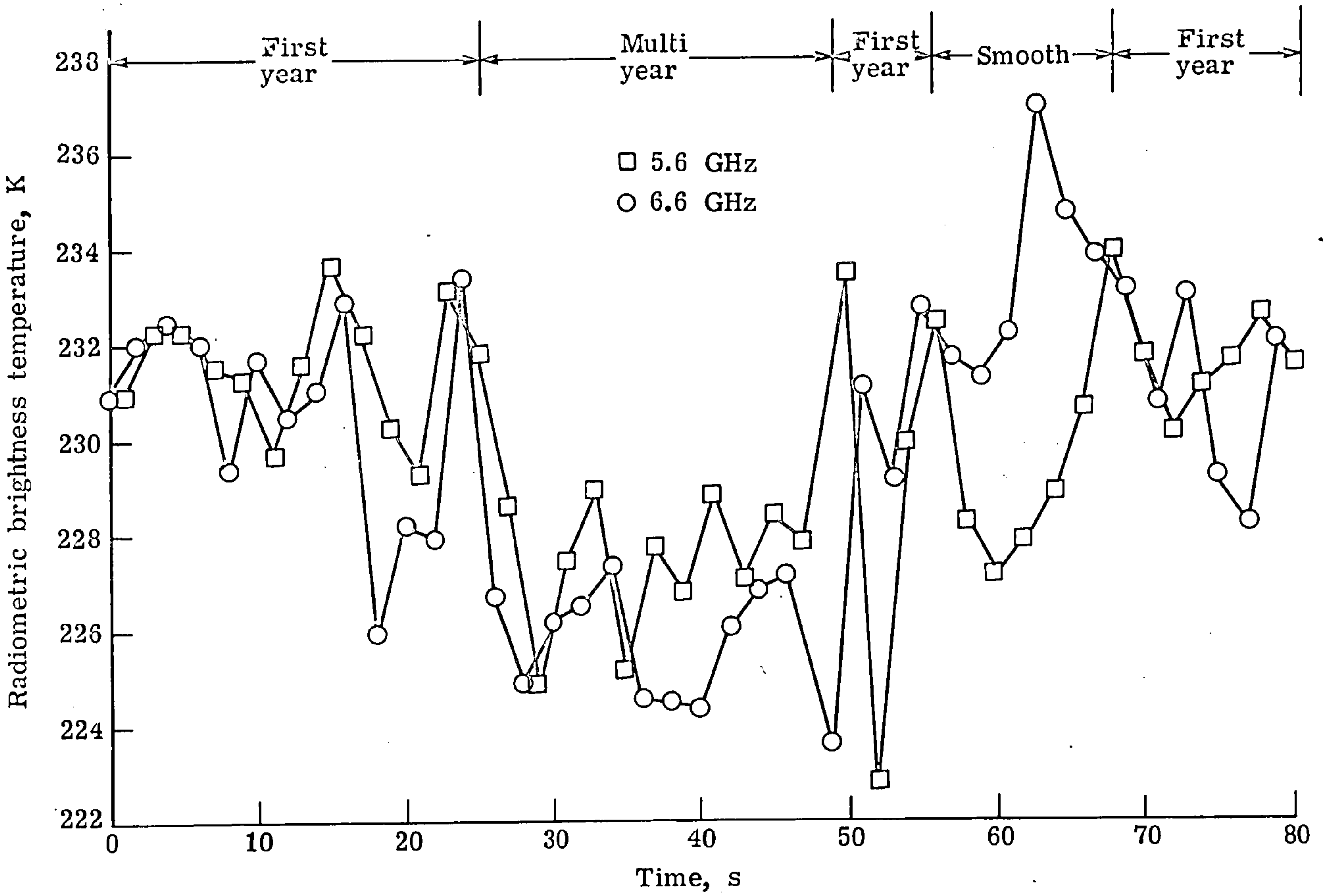

Figure 5-14. Radiometric brightness temperature of sea ice versus time for run 6 at frequencies alternating between 5.6 GHz and 6.6 GHz every 0.5 s.

from 232 K down to 227 K and back to 234 K as the aircraft crossed the area of smooth ice. The measurement at 6.6 GHz varied from 232 K up to 237 K, then back to 232 K. The measurement at 7.2 GHz remained fairly constant at 235 K. The aerial photograph of this area showed a smooth snow covered region with no indication of multiyear ice.

A pronounced quarter wavelength oscillation due to the Fabry-Perot interference fringes was observed over a piece of smooth ice. An aerial photograph of this area is shown in Fig. 5-15. An interesting feature is the presence of two cracks on either side of the region of ice which showed the frequency sensitive responses in the radiometric brightness temperature. The location of this ice is near latitude 71°47'N and longitude 145°21'W. Five passes over this area of ice were made by the NASA C-130 at an altitude of 330 m.

The radiometric brightness temperature measured at 5.6 GHz by the SFMR for three passes over this area is shown in Fig. 5-16. As the antenna field of view passed between the two cracks in Fig. 5-15, the radiometric brightness temperature decreased from approximately 233 K to a value near 215 K. Runs 4, 5, and 9 all showed the same responses. The measurement for run 8 at 7.2 GHz is shown in Fig. 5-17. The radiometric brightness temperature decreased from about 233 K to 227 K over this section of ice. The SFMR was operated in a frequency stepping mode during run 7. The frequency was alternating each second between 5.6 GHz and 6.6 GHz. The radiometric brightness temperature measured at these frequencies by the SFMR is shown in Fig. 5-18. The response at 5.6 GHz

Figure 5-15. Aerial photograph of a section of smooth, frequency sensitive sea ice along line 1 in Fig. 5-10.

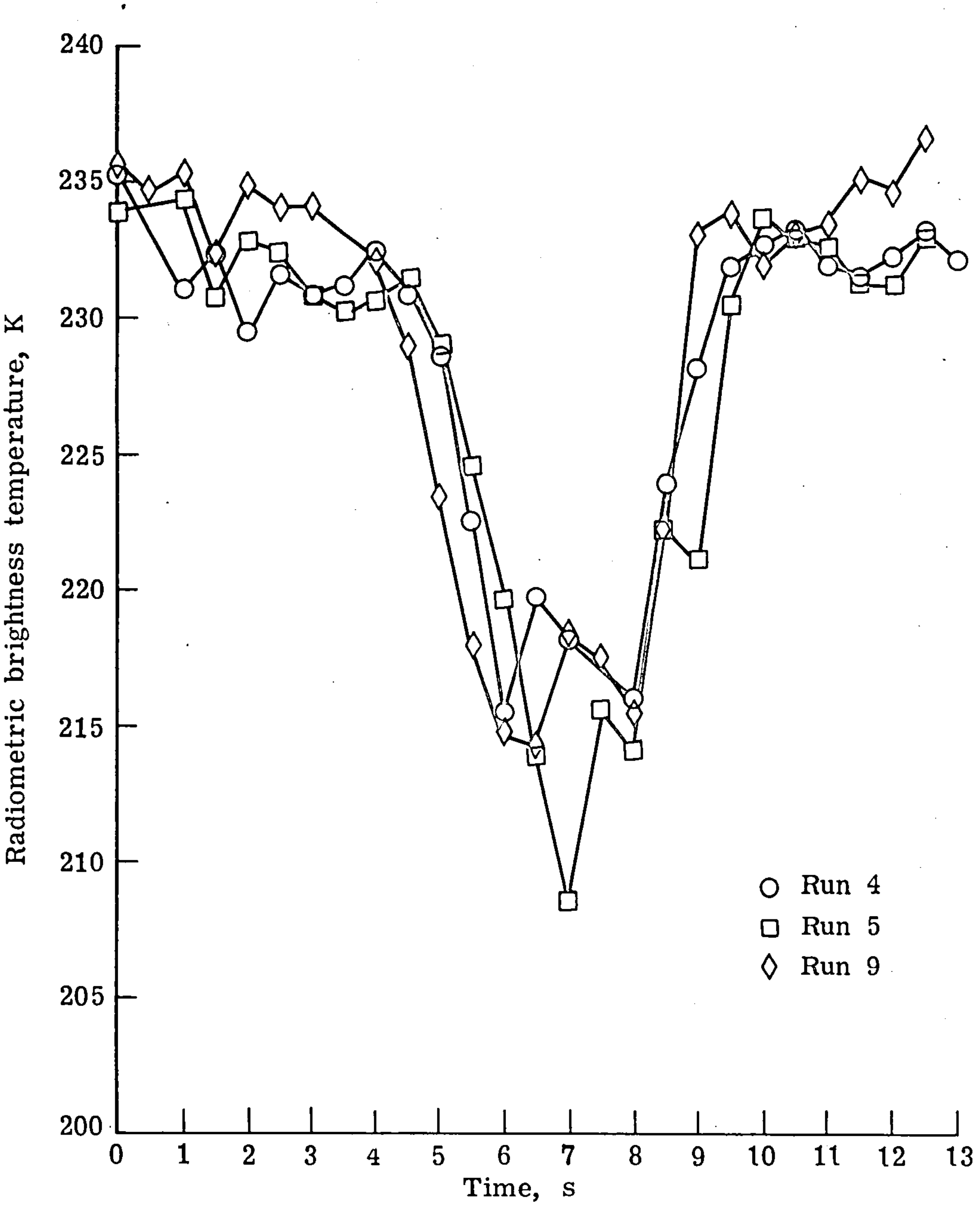

Figure 5-16. Radiometric brightness temperature of the frequency sensitive sea ice versus time for runs 4, 5, and 9 at a frequency of 5.6 GHz.

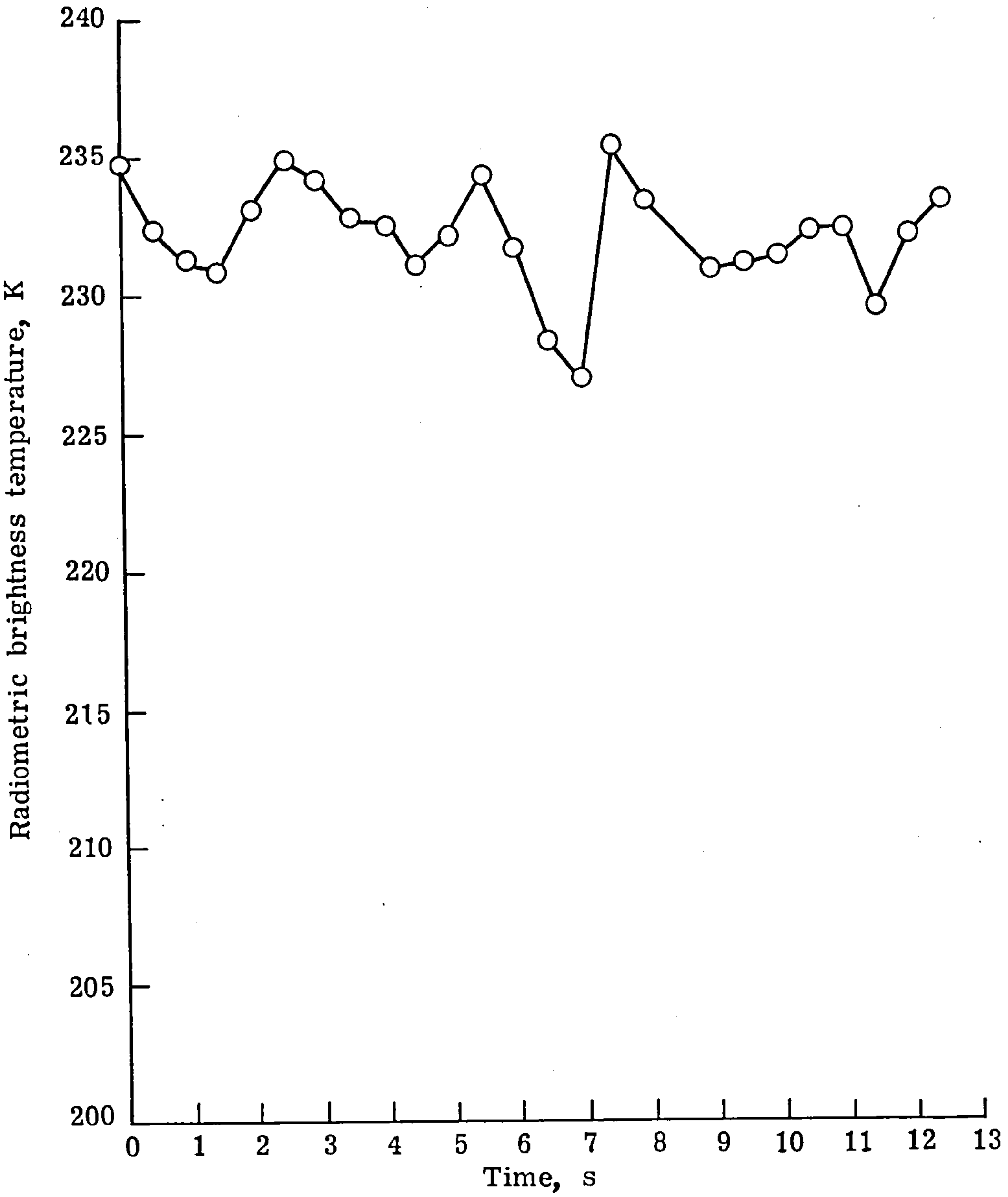

Figure 5-17. Radiometric brightness temperature of the frequency sensitive sea ice versus time for run 8 at a frequency of 7.2 GHz.

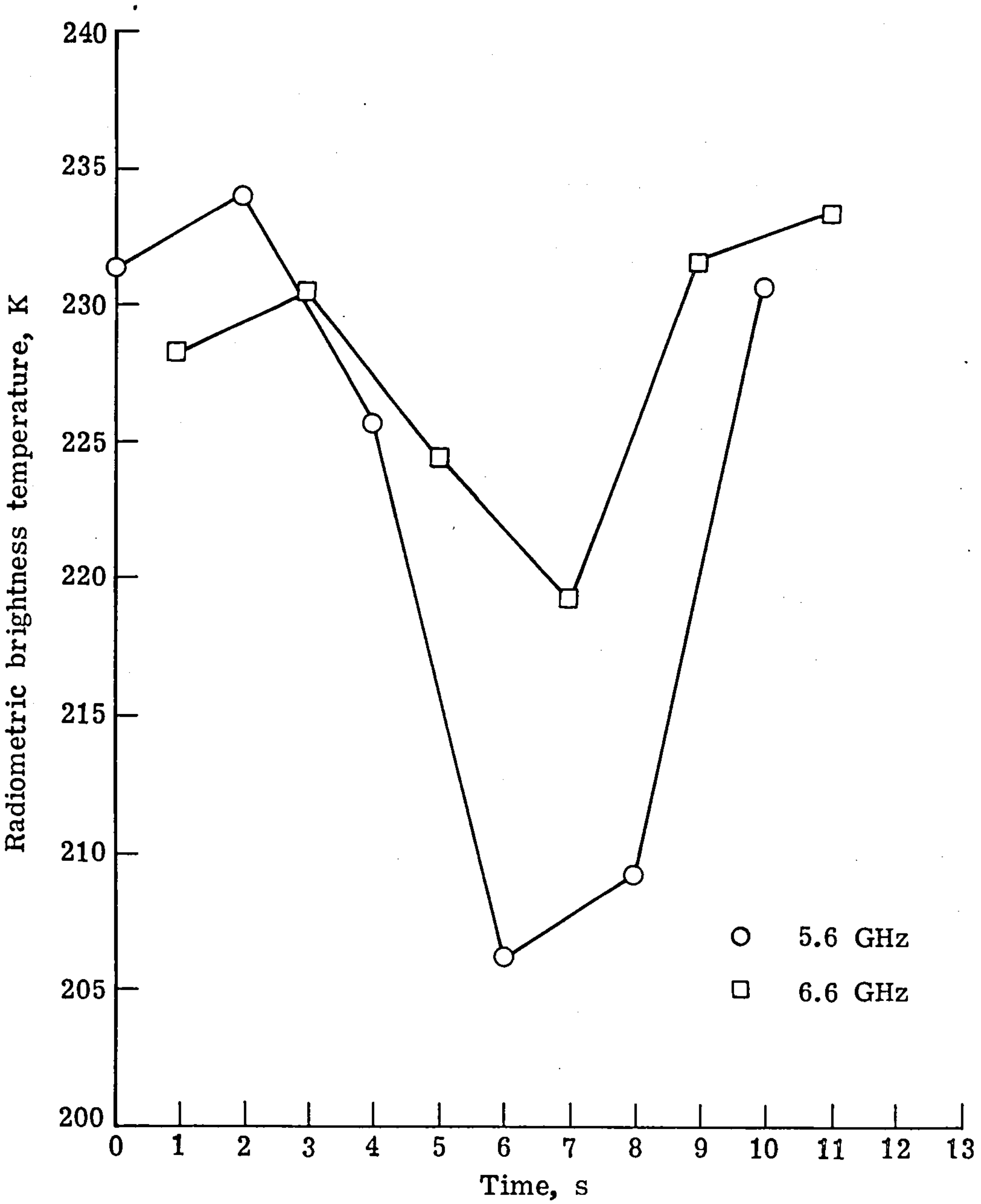

Figure 5-18. Radiometric brightness temperature of the frequency sensitive sea ice versus time for run 7 at frequencies alternating between 5.6 GHz and 6.6 GHz every second.

agrees with those measured during runs 4, 5, and 9 as shown in Fig. 5-16. The decrease in the radiometric brightness temperature at 6.6 GHz was greater than that at 7.2 GHz and less than that at 5.6 GHz reaching a value of 219 K over this area.

The results of runs 4, 5, 7, 8, and 9 over this particular area of sea ice prove the capability of a frequency stepping radiometer to detect sea ice which has a frequency dependent radiometric brightness temperature. The evidence indicates that this frequency dependent response is due to the Fabry-Perot interference fringes from a thin layer of sea ice over water as discussed in Chapter II. The visual appearance of the ice indicates either snow covered thin ice or first year white ice. The thickness of white ice would be approximately 0.5 m to 1.0 m. However, based on an estimate from the frequency dependent radiometric brightness temperature measurements from the SFMR, this is a section of snow covered thin ice only a few centimeters thick. Actual ground truth measurements of the ice thickness were not available due to the remote location of the area.

CHAPTER VI

CONCLUSIONS

This research resulted in the design and development of the stepped frequency microwave radiometer (SFMR) whose versatility, accuracy, and stability are such that remote sensing experiments can be conducted which should produce significant measurements of sea surface temperature, lake ice thickness, sea ice type, and sea ice thickness. The development of inversion techniques for determination of geophysical parameters from the radiometric brightness temperature measured by the SFMR is required and presently being pursued by the author and others at the NASA Langley Research Center. Also, accurate, empirically developed wind correction models are needed. These can be developed using the computer algorithms and SFMR developed during this research.

Computational procedures and a simplified algorithm were developed to accurately predict the radiometric brightness temperature at the input to the SFMR antenna as a function of the geophysical parameters. A computer model of the SFMR was developed that determines the radiometric brightness temperature at the input to the SFMR antenna as a function of the SFMR output.

The SFMR is a balanced Dicke switched microwave radiometer which operates at any frequency between 4.5 GHz and 7.2 GHz. It employs a noise injection design technique. The noise injection is controlled by a second order feedback loop. The critical components of the microwave front end are contained in a constant temperature enclosure in order to accurately predict the effect of microwave losses. The SFMR is capable of operating at four bandwidths and six integration times at either a fixed frequency or in a frequency stepping mode. The radiometer operation and the digital output data are controlled and recorded by a microprocessor based digital controller. An accuracy analysis of the radiometer was performed which demonstrated that the absolute accuracy is better than 0.5 K for a sensitivity of 0.1 K. The sensitivity is a function of the bandwidth and integration time and can be set anywhere between 0.0125 K and 1.25 K depending on the bandwidth and integration time selected.

An algorithm was developed which can determine the expected radiometric brightness temperature at the input to the SFMR antenna as a function of the aircraft altitude, atmospheric thermodynamic temperature, and the surface thermodynamic temperature measured by the aircraft infrared radiometer. This algorithm was based on regression fits to the parametric studies performed using the computer program developed during this research. This algorithm matched the computer program to within 0.1 K. Computer programs were developed to predict the emissivity of layered dielectric media such as lake ice, sea ice, and wind generated ocean foam.

The SFMR was flown in several aircraft remote sensing experiments, and four significant scientific observations were accomplished with this instrument. The results from the 1979 Norwegian Remote Sensing Experiment (NORSEX) measurements represent the first successful mapping of the ocean polar front in the Barents Sea by a microwave radiometer. The

SFMR performed measurements of lake ice thickness in the Great Lakes by measuring the total ice attenuation. Indications of Fabry-Perot interface fringes were also observed over Claytor Lake for thin smooth lake ice. The first measurement of ice age by a radiometer operating below 10 GHz was accomplished during the 1979 Sea Ice Radar Experiment (SIRE) north of Alaska in the Beaufort Sea. The SFMR collected the first reported airborne measurements of frequency sensitive sea ice, which is an indication of Fabry-Perot interference fringes, which represent the capability to measure sea ice thickness. The results from these various measurements demonstrate that the objective of this research was achieved.

LIST OF REFERENCES

Apinis, John J.; and Peake, William H.: Passive Microwave Mapping of Ice Thickness. ElectroScience Laboratory, The Ohio State University Final Report 3892-2, August 1976.

Bendat, Julius S.; and Piersol, Allan G.: Random Data: Analysis and Measurement Procedures. Wiley-Interscience, John Wiley & Sons, Inc., 1971.

Blume, Hans-Juergen C.: Noise Calibration Repeatability of an Airborne Third-Generation Radiometer. IEEE Transactions on Microwave Theory and Techniques, Vol. MTT-25, No. 10, October 1977, pp. 852-855.

Blume, Hans-Juergen C.; Love, A. W.; Van Melle, M. J.; and Ho, William W.: Radiometric Observations of Sea Temperature at 2.65 GHz Over the Chesapeake Bay. IEEE Transactions on Antennas and Propagation, Vol. AP-25, No. 1, January 1977, pp. 121-128.

Blume, Hans-Juergen C.; Kendall, Bruce M.; and Fedors, John C.: Measurement of Ocean Temperature and Salinity Via Microwave Radiometry. Boundary-Layer Meteorology, Vol. 13, Nos. 1, 2, 3, and 4, January 1978, pp. 295-308.

Blume, Hans-Juergen C.; Kendall, Bruce M.; and Fedors, John C.: Submarine Fresh Water Outflow Detection With a Two Frequency Microwave Radiometer System. Paper to be presented at the COSPAR/SCOR/IUCRM Symposium Oceanography From Space, Venice, Italy, May 1980.

Campbell, W. J.; Gloersen, P.; Nordberg, W.; and Wilheit, T. T.: Dynamics and Morphology of Beaufort Sea Ice Determined From Satellites, Aircraft, and Drifting Stations. Proceedings of the Symposium on Approaches to Earth Survey Problems Through Use of Space Techniques, Constance F.R.G., May 1973, pp. 311-327.

Campbell, W. J.; Wayenberg, J.; Ramsever, J. B.; Ramseier, R. O.; Vant, M. R.; Weaver, R.; Redmond, A.; Arsenault, L.; Gloersen, P.; Zwally, H. J.; Wilheit, T. T.; Chang, A. T. C.; Hall, D.; Gray, L.; Meeks, D. C.; Bryan, M. L.; Barath, F. T.; Elachi, C.; Leberl, F.; and Farr, I.: Microwave Remote Sensing of Sea Ice in the AIDJEX Main Experiment. Boundary-Layer Meteorology, Vol. 13, Nos. 1, 2, 3, and 4, January 1978, pp. 309-337.

Campbell, W. J.; Deily, F. H.; Flatow, F. S.; Kellogg, W. W.; Ramseier, R. O.; Untersteiner, N.; Weeks, W. F.; Weller, G. E.; Zwally, H. J.; and Stowell, D. Y.: Ice and Climate Experiment. Report of the Science and Applications Working Group. NASA Goddard, 1979.

Chang, A. T. C.; Hall, D. K.; Foster, J. L.; Rango, A.; and Schmugge, T. J.: Studies of Snowpack Properties by Passive Microwave Radiometry. NASA TM-79671, 1978.

Cox, Charles; and Munk, Walter: Measurement of the Roughness of the Sea Surface From Photographs of the Sun's Glitter. Journal of the Optical Society of America, Vol. 44, No. 11, November 1954, pp. 838-850.

Delnore, V. E.; Harrington, R. F.; Jones, W. L.; and Swift, C. T.: Combined Active-Passive Microwave Measurements of the Sea Surface in the Grand Banks Frontal Region. Paper to be presented at the Joint Meeting of the American and Canadian Geophysical Union, Toronto, Canada, May 1980.

Dicke, R. H.: The Measurement of Thermal Radiation at Microwave Frequencies. The Review of Scientific Instruments, Vol. 17, No. 7, July 1946, pp. 268-275.

Gloersen, P.; Nordberg, W.; Schmugge, T. J.; and Wilheit, T. T.: Microwave Signatures of First Year and Multiyear Sea Ice. Journal of Geophysical Research, Vol. 78, No. 18, June 20, 1973, pp. 3564-3572.

Gloersen, Per; and Barath, Frank T.: A Scanning Multichannel Microwave Radiometer for Nimbus-G and SeaSat-A. IEEE Journal of Oceanic Engineering, Vol. OE-2, No. 2, April 1977, pp. 172-178.

Gloersen, P.; Zwally, H. J.; Chang, A. T. C.; Hall, D. K.; Campbell, W. J.; and Ramseier, R. O.: Time Dependence of Sea Ice Concentration and Multiyear Ice Fraction in the Arctic Basin. Boundary Layer Meteorology, Vol. 13, Nos. 1, 2, 3, and 4, January 1978, pp. 339-359.

Goggins, William B., Jr.: A Microwave Feedback Radiometer. IEEE Transactions on Aerospace and Electronic Systems, Vol. AES-3, No. 1, January 1967, pp. 83-90.

Hall, Dorothy K.; Foster, James L.; Rango, Albert; and Chang, Alfred T. C.: Passive Microwave Studies of Frozen Lakes. NASA TM-79613, 1978.

Hardy, Walter N.: Precision Temperature Reference for Microwave Radiometry. IEEE Transactions on Microwave Theory and Techniques, Vol. MTT-21, No. 3, March 1973, pp. 149-150.

Hardy, Walter N.; Gray, Kenneth W.; and Love, A. W.: An S-Band Radiometer Design With High Absolute Precision. IEEE Transactions on Microwave Theory and Techniques, Vol. MTT-22, No. 4, April 1974, pp. 382-390.

Hidy, G. M.; Hall, W. F.; Hardy, W. N.; Ho, W. W.; Jones, A. C.; Love, A. W.; Van Melle, M. J.; Wang, H. H.; and Wheeler, A. E.: Development of a Satellite Microwave Radiometer to Sense the Surface Temperature of the World Oceans. NASA CR-1960, 1972.

Hollinger, James P.: Passive Microwave Measurements of the Sea Surface. Journal of Geophysical Research, Vol. 75, No. 27, September 20, 1970, pp. 5209-5213.

Hollinger, James P.: Passive Microwave Measurements of Sea Surface Roughness. IEEE Transactions on Geoscience Electronics, Vol. GE-9, No. 3, July 1971, pp. 165-169.

Johannessen, Ola M.; and Foster, L. A.: A Note on the Topographically Controlled Oceanic Polar Front in the Barents Sea. Journal of Geophysical Research, Vol. 83, No. C9, Sept. 20, 1978, pp. 4567-4571.

Johnson, J. B.: Thermal Agitation of Electricity in Conductors. Physical Review, Vol. 32, July 1928, pp. 97-109.

Kerr, Donald E., ed: Propagation of Short Radio Waves. McGraw-Hill Book Co., Inc., 1951.

Klein, Lawrence A.; and Swift, Calvin T.: An Improved Model for the Dielectric Constant of Sea Water at Microwave Frequencies. IEEE Transactions on Antennas and Propagation, Vol. AP-25, No. 1, January 1977, pp. 104-111.

Knight, John: A General Expression for the Output of a Dicke Type Radiometer. Proceeding of the IRE, Vol. 50, No. 12, December 1962, pp. 2497-2498.

Lawrence, Roland W.; Stanley, William D.; and Harrington, Richard F.: Digital Signal Processing in Microwave Radiometers. Paper presented at the 1980 IEEE Southeascon, Nashville, Tenn., April 1980.

Lipes, R. G.; Bernstein, R. L.; Cardone, V. J.; Katsaros, K. B.; Njoku, E. G.; Riley, A. L.; Ross, D. B.; Swift, C. T.; and Wentz, F. J.: Seasat Scanning Multichannel Microwave Radiometer: Results of the Gulf of Alaska Workshop. Science, Vol. 204, June 29, 1979, pp. 1415-1417.

Love, A. W.; Ho, W. W.; and Van Melle, M. J.: Engineering Design of a Laboratory Prototype Stepped Frequency Radiometer. SD 75-SA-0006, Rockwell International, 1975.

Mentzer, C. A.; Peters, L.; and Beck, F. B.: A Corrugated Horn Antenna Using V-Shape Corrugations. IEEE Transactions on Antennas and Propagation, Vol. AP-23, No. 1, January 1975, pp. 93-97.

Nordberg, W.; Conaway, J.; Ross, Duncan B.; and Wilheit, T.: Measurements of Microwave Emission From a Foam-Covered, Wind-Driven Sea. Journal of the Atmospheric Sciences, Vol. 38, April 1971, pp. 429-435.

Peake, William H.: Interaction of Electromagnetic Waves With Some Natural Surfaces. IRE Transactions on Antennas and Propagation, Vol. AP-7, No. 5, December 1959, pp. 324-329.

Planck, Max (Morton Masius, transl.): The Theory of Heat Radiation. Dover Publications, Inc., 1913.

Reeves, Robert G.: Manual of Remote Sensing. American Society of Photogrammetry, 1975.

Ross, Duncan B.; and Cardone, Vincent: Observations of Oceanic Whitecaps and Their Relation to Remote Measurements of Surface Wind Speed. Journal of Geophysical Research, Vol. 79, No. 3, January 20, 1974, pp. 444-452.

Ryle, M.; and Vonberg, D. D.: An Investigation of Radio-Frequency Radiation From the Sun. Proc. Roy. Soc. (London), Vol. 193, April 1948, pp. 98-120.

Schmugge, T.; Wilheit, T. T.; and Gloersen, P.: Microwave Signatures of Snow and Fresh Water Ice. Conference on Advanced Concepts and Techniques in the Study of Snow and Ice Resources, National Academy of Sciences, Monterey, Calif., Dec. 1973, pp. 551-562.

Seling, Theodore V.: An Investigation of a Feedback Control System for Stabilization of Microwave Radiometers. IRE Transactions on Microwave Theory and Techniques, Vol. 10, No. 3, May 1962, pp. 209-213.

Silver, Samuel, ed: Microwave Antenna Theory and Design. McGraw-Hill Book Co., Inc., 1949.

Smith, John I.: Modern Operational Circuit Design. Wiley-Interscience, a division of John Wiley and Sons, Inc., 1971.

Stanley, William D.: Digital Simulation of Dynamic Processes in Radiometer Systems. Old Dominion University Research Foundation Report on NAS1-14193 Task 46, May 1979(a).

Stanley, William D.: Preliminary Development of Digital Signal Processing in Microwave Radiometers. Old Dominion University Research Foundation Report on NAS1-15676, 1979(b).

Stanley, William D.; Harrington, Richard F.; and Lawrence, Roland W.: Dynamic Simulation of Random Processes in Radiometers Using CSMP and ACSL. Paper presented at the 1979 IEEE Southeascon, Roanoke, Virginia, April 1979.

Stanley, William D.; and Peterson, Steven J.: Equivalent Statistical Bandwidths of Conventional Low-Pass Filters. IEEE Transactions on Communications, Vol. COM-27, No. 10, October 1979, pp. 1633-1634.

Stogryn, A.: The Apparent Temperature of the Sea at Microwave Frequencies. IEEE Transactions on Antennas and Propagation, Vol. AP-15, No. 2, March 1967, pp. 278-286.

Stratton, Julius A.: Electromagnetic Theory. McGraw-Hill Book Co., Inc., 1941.

Strom, Leland D.: The Theoretical Sensitivity of the Dicke Radiometer. Proceedings of the IRE, Vol. 45, No. 9, September 1957, pp. 1291-1292.

Swift, C. T.: Microwave Radiometer Measurements of the Cape Cod Canal. Radio Science, Vol. 9, No. 7, July 1974, pp. 641-653.

Swift, C. T.: Passive Microwave Remote Sensing of the Ocean - A Review. Boundary-Layer Meteorology, Vol. 18, 1980, pp. 25-54.

Thomann, Gary C.: Experimental Results of the Remote Sensing of Sea-Surface Salinity at 21-cm Wavelength. IEEE Transactions on Geoscience Electronics, Vol. GE-14, No. 3, July 1976, pp. 198-214.

Tiuri, M. E.: Radio Astronomy Receivers. IEEE Transactions on Antennas and Propagation, Vol. AP-12, No. 4, December 1964, pp. 930-938.

Tiuri, Martti; Hallikainen, Martti; and Laaperi, Antti: Radiometer Studies of Low-Salinity Sea Ice. Boundary-Layer Meteorology, Vol. 13, Nos. 1, 2, 3, and 4, January 1978, pp. 361-371.

U. S. Standard Atmosphere, 1976. U. S. Government Printing Office.

Vant, M. R.; Gray, R. B.; Ramseier, R. O.; and Makios, V.: Dielectric Properties of Fresh and Sea Ice at 10 and 35 GHz. Journal of Applied Physics, Vol. 45, No. 11, November 1974, pp. 4712-4717.

Vant, Malcolm R.: A Combined Empirical and Theoretical Study of the Dielectric Properties of Sea Ice Over the Frequency Range 100 MHz to 40 GHz. Ph.D. Thesis, Carleton University, Ottawa, Canada, June 1976.

Wait, David F.: The Sensitivity of the Dicke Radiometer. Journal of Research of the National Bureau of Standards, Vol. 71C, No. 2, April-June 1967, pp. 127-152.

Watson, H. A., ed: Microwave Semiconductor Devices and Their Circuit Applications. McGraw-Hill Book Co., Inc., 1969.

Webster, William J.; Wilheit, Thomas T.; Ross, Duncan B.; and Gloersen, Per: Spectral Characteristics of the Microwave Emission From a Wind-Driven Foam-Covered Sea. Journal of Geophysical Research, Vol. 81, No. 18, June 20, 1976, pp. 3095-3099.

Wilheit, T.: The Electrically Scanning Microwave Radiometer (ESMR) Experiment. The Nimbus 5 User's Guide, U.S. Government Printing Office, 1972.

Wilheit, T.: The Electrically Scanning Microwave Radiometer (ESMR) Experiment. The Nimbus 6 User's Guide, U.S. Government Printing Office, 1975.

Wilheit, Thomas T., Jr.; and Fowler, Mary Grace: Microwave Radiometric Determination of Wind Speed at the Surface of the Ocean During BESEX. IEEE Transactions on Antennas and Propagation, Vol. AP-25, No. 1, January 1977, pp. 111-120.

Young, Leo; Robinson, Lloyd A.; and Hacking, Colin A.: Meander-Line Polarizer. IEEE Transactions on Antennas and Propagation, Vol. AP-21, No. 3, May 1973, pp. 376-378.

Zwally, H. Jay; and Gloersen, Per: Passive Microwave Images of the Polar Regions and Research Applications. Polar Record, Vol. 18, No. 116, 1977, pp. 431-450.

APPENDIX A

ERROR DUE TO RAYLEIGH-JEANS APPROXIMATION

The brightness of a blackbody due to a finite thermodynamic temperature can be determined from Planck's Radiation Law as (Reeves, 1975)

$$B(f,T) = \frac{2hf^3}{c^2}\left[\frac{1}{\exp\left(\frac{hf}{kT}\right) - 1}\right]. \tag{A-1}$$

The Rayleigh-Jeans approximation to Planck's Radiation Law is (Reeves, 1975)

$$B(f,T) = \frac{2kTf^2}{c^2}. \tag{A-2}$$

The brightness obtained from (A-2) would be an approximate value of the true brightness. Let $\hat{B}$ be the approximate value obtained using the Rayleigh-Jeans approximation. The error is equal to the true value minus the approximate value and is obtained from (A-1) and (A-2).

$$B = \frac{hf}{k}\left[\frac{1}{\exp\left(\frac{hf}{kT}\right) - 1}\right]. \tag{A-3}$$

Expanding the exponential and factoring yields

$$B = T\left[\frac{1}{1 + \frac{1}{2!}\left(\frac{hf}{kT}\right) + \frac{1}{3!}\left(\frac{hf}{kT}\right) + \ldots}\right]. \tag{A-4}$$

Substituting the following series expansion in (A-4):

$$\left(1 + a_1x + a_2x^2 + \ldots\right)^{-1} = \left[1 - a_1x + \left(a_1{}^2 - a_2\right)x^2 + \ldots\right]. \tag{A-5}$$

yields an expression for the error $B - \hat{B}$. Since brightness and brightness temperature are related (Reeves, 1975), the error can be expressed in terms of brightness temperature temperature. The error is

$$T - \hat{T} = \frac{1}{2}\frac{hf}{k} - \frac{1}{12}\frac{h^2f^2}{k^2T} + \ldots . \tag{A-6}$$

Neglecting higher order terms, the error ε_T is

$$\varepsilon_T = \frac{1}{2}\frac{hf}{k} - \frac{1}{12}\frac{h^2f^2}{k^2T}. \tag{A-7}$$

Substitution of known constants in (A-7):

$$\varepsilon_T = 2.4 \times 10^{-2}\ f - 1.9 \times 10^{-4}\ f^2T^{-1} \tag{A-8}$$

where frequency f is in GHz and temperature T is in K. The error is primarily a function of frequency and exceeds 0.1 K at 4.17 GHz and 1 K at 41.7 GHz. The second term contributes less than 0.1 K error below 72 GHz. The error is a fixed bias error such that the true temperature is higher than that obtained from the Rayleigh-Jeans approximation.

APPENDIX B

RADIATIVE TRANSFER EQUATION PROGRAM

This appendix contains a flow chart of the computer program to calculate the radiometric brightness temperature at the input to the radiometer antenna as a function of the geophysical parameters. The program was written in the Fortran Extended Version 4.7 and is used on the CDC CYBER 170, CYBER 70 and 6000 series computer systems at the Langley Research Center.

The flow chart of the main program TANT is shown in Fig. B-1. Subroutine EM computes the emissivity of the surface using the dielectric constant model developed by Klein and Swift (1977) for both fresh and sea water, data from Vant (1976) for lake ice and sea ice, (2-77) for the layered dielectric media, and the Fresnal reflection coefficients. The flow chart for subroutine ATMOD is shown in Fig. B-2. Subroutine ATCO computes the atmospheric pressure and temperature based on the 1976 U.S. Standard Atmosphere. Subroutine AABC computes the absorption coefficients for oxygen, water vapor, and liquid water content of clouds as a function of altitude from the surface to 50 km. Subroutine ATINT integrates the absorption coefficients to obtain opacities as a function of altitude using a five point extended Simpson's Rule.

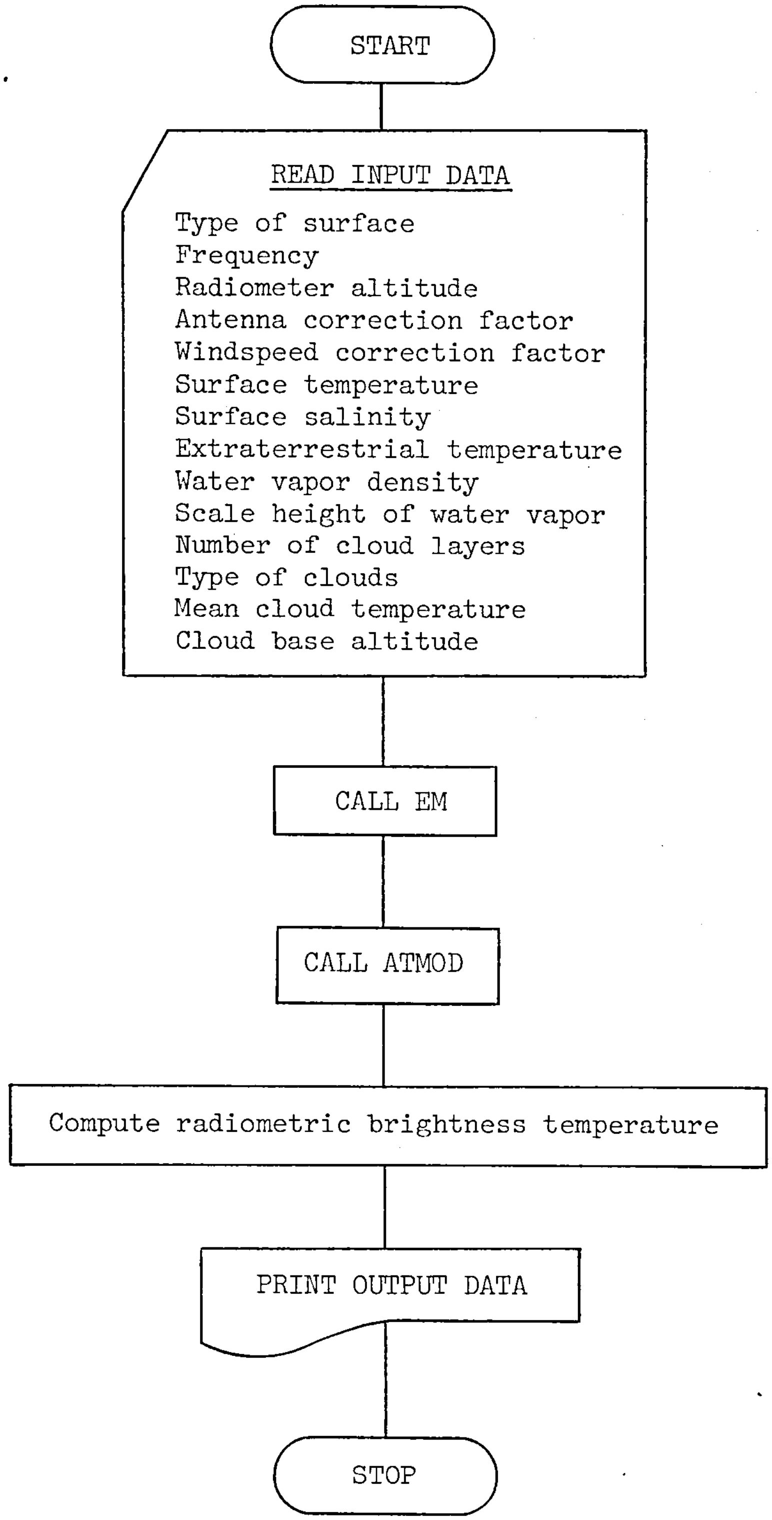

Figure B-1. Flow chart of TANT.

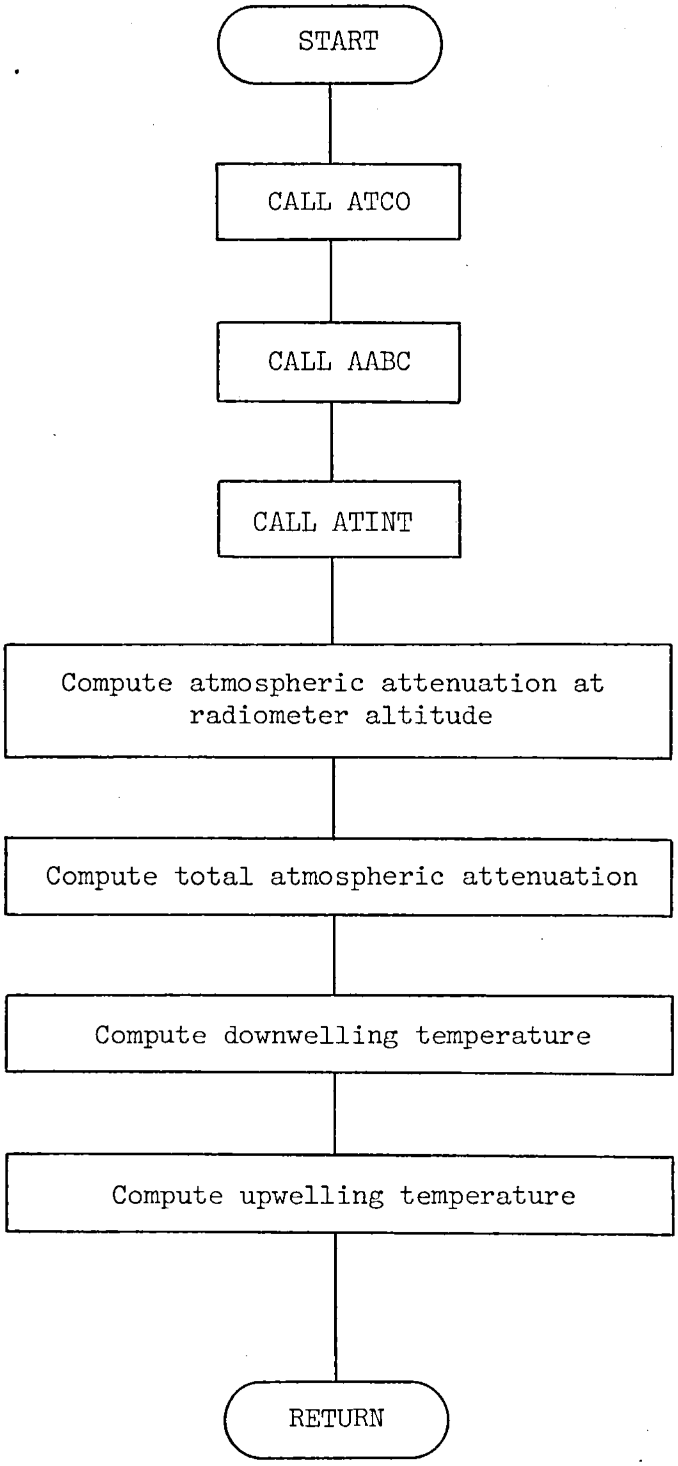

Figure B-2. Flow chart of ATMOD.

1. Report No. NASA TM-81847	2. Government Accession No.	3. Recipient's Catalog No.

4. Title and Subtitle THE DEVELOPMENT OF A STEPPED FREQUENCY MICROWAVE RADIOMETER AND ITS APPLICATION TO REMOTE SENSING OF THE EARTH

5. Report Date
June 1980

6. Performing Organization Code

7. Author(s)
Richard F. Harrington

8. Performing Organization Report No.

9. Performing Organization Name and Address
NASA Langley Research Center
Hampton, Virginia 23665

10. Work Unit No.
506-61-63-01

11. Contract or Grant No.

12. Sponsoring Agency Name and Address
National Aeronautics and Space Administration
Washington, DC 20546

13. Type of Report and Period Covered
Technical Memorandum

14. Sponsoring Agency Code

15. Supplementary Notes

16. Abstract

The design, development, application, and capabilities of a variable frequency microwave radiometer are described. This radiometer has demonstrated the versatility, accuracy, and stability required to provide contributions to the geophysical understanding of ocean and ice processes. The design technique utilized a closed-loop feedback method, whereby noise pulses were added to the received electromagnetic radiation to achieve a null balance in a Dicke switched radiometer. Stability was achieved through the use of a constant temperature enclosure around the low loss microwave front end. The Dicke reference temperature was maintained to an absolute accuracy of 0.1 K using a closed-loop proportional temperature controller. Versatility was achieved by developing a microprocessor based digital controller which operates the radiometer and records the data on computer compatible tapes. Accuracy analysis has shown that this radiometer exhibits an absolute accuracy of better than 0.5 K when the sensitivity is 0.1 K. The sensitivity varies between 0.0125 K and 1.25 K depending upon the bandwidth and integration time selected by the digital controller.

Remote sensing experiments were conducted from an aircraft platform using this radiometer. The purpose of these experiments was to demonstrate that the accuracy and versatility of this instrument had been achieved in actual field experiments. Four significant scientific observations were accomplished during these experiments. These observations consisted of the first radiometeric mapping of an ocean polar front, exploratory experiments to measure the thickness of lake ice, first discrimination between first year and multiyear ice below 10 GHz, and the first known measurements of frequency sensitive characteristics of sea ice.

17. Key Words (Suggested by Author(s))
Electronic and Electrical Engineering
Physical Oceanography
Snow, Ice and Permafrost
Electricity and Magnetism

18. Distribution Statement
Unclassified - Unlimited
Subject Category 33

19. Security Classif. (of this report) Unclassified	20. Security Classif. (of this page) Unclassified	21. No. of Pages 179	22. Price* A09

* For sale by the National Technical Information Service, Springfield, Virginia 22161